

Detached eddy simulations of single and coaxial supersonic jets

Alessandro Mancini

Department of Engineering

University of Leicester

A thesis submitted for the degree of

Doctor of Philosophy

January 2018

Detached eddy simulations of single and coaxial supersonic jets

Alessandro Mancini

Aircraft today are 20-30 dB quieter than the first passenger jets, emitting less than 1% of the noise. Further reductions in noise emission are a real challenge. The jet noise component is relatively well understood for simple geometries but it is still elusive to accurate and efficient models able to predict it for real turbofan engine nozzle configurations. Enhanced modelling of the complex three-dimensional flow from dual-flux jets of turbofan engines, in which shock waves interact with turbulent structures to generate shock-associated jet noise, is therefore required. This work explores whether lower-order hybrid Detached Eddy Simulation (DES) schemes can be used for aeroacoustic investigations of supersonic under-expanded jets. The objective of this thesis is to produce and analyse aeroacoustic results from under-expanded supersonic single and dual jets with an affordable DES numerical scheme. The main goal is to use a relatively computationally cheap numerical solver able to produce engineering accurate acoustic results for under-expanded jets. Compared to high-order full Large Eddy Simulation (LES) predictions, the second-order time accurate and up to third-order space accurate DES approach here proposed would give a strong advantage in terms of time and computational cost using a fraction of the resources of a full LES. The outcome of the work proves that the adopted approach is suitable for the analysis of BroadBand Shock Associated Noise (BBSAN) in under-expanded supersonic single jets. With respect to dual-flux coaxial jets, further tests are necessary to assess the behaviour of the DES approach in the region of interaction of strong waves with the RANS boundary layer close to the walls in order for the DES approach to be safely and confidently used as a design tool for the engine-airframe integration of wide-body civil aircraft.

Acknowledgements

The author wishes to thank Dr. Aldo Rona, his supervisor, for the opportunity given to him to work in the AeroTraNet2 project, for his inestimable guidance, and for his constant support throughout these four years. A special thank goes to Dr. Edward Hall for his continuous help and support on many occasions, and for his friendship. A thank to all the fellows of the AeroTraNet2 project for making this an unforgettable experience.

The dissemination of these results has received funding from the European Union Seventh Framework Programme FP7/2007-2013 under grant agreement no. 317142. The author wishes to express his gratitude to Dr. Guillaume Puigt for the invaluable help, advice, and encouragement he provided.

Words cannot express the author's gratitude to Carlos Pérez Arroyo.

Contents

Contents	iii
Nomenclature	vi
1 Introduction	1
2 Aeroacoustics of free jets	7
2.1 Introduction	7
2.2 Jets	7
2.3 Jet aeroacoustics	11
2.3.1 Jet mixing noise	12
2.3.2 Shock-associated noise	14
2.3.2.1 Broadband Shock-Associated Noise	14
2.3.2.2 Screech Tonal Noise	17
2.3.3 Coaxial Jets	25
2.4 Computational Aeroacoustics (CAA)	30
3 Methodology	34
3.1 Introduction	34

3.2	Governing equations	34
3.3	Detached Eddy Simulation	37
3.3.1	Governing equations	37
3.3.2	Finite-volume spatial discretisation	46
3.3.3	Time integration	51
3.3.4	Boundary conditions	52
3.3.4.1	Non-reflecting far-field	53
3.3.4.2	Subsonic inflow	55
3.3.4.3	Subsonic outflow	57
3.3.4.4	No-slip wall	58
3.3.5	Sponge region treatment	59
3.4	MPI approach	60
3.5	Validation	61
4	Supersonic under-expanded single jet	63
4.1	Experimental set-up	64
4.2	Mesh and numerical set-up	64
4.3	Results	67
5	Supersonic under-expanded dual-stream jet	83
5.1	Test case conditions	83
5.2	Mesh and numerical set-up	84
5.3	Experimental set-up	85
5.4	Results	88
5.4.1	Time-averaged flow	89
5.4.2	Effects of secondary nozzle shift in VKI experiments	106

5.4.3 Unsteady flow and noise production	110
6 Conclusions	121
6.1 Single jet test case	122
6.2 Dual-stream jet test case	123
6.3 Further work	126
Bibliography	127

Nomenclature

Roman symbols

a	Speed of sound
A	Area
c	Local speed of sound
C_p	Specific heat at constant pressure
C_v	Specific heat at constant volume
D	Diameter
e	Specific energy
f	Frequency
\mathbf{F}	Vector of convective inviscid fluxes
\mathbf{F}_v	Vector of convective viscous fluxes
\mathbf{I}	Identity matrix
\bar{k}	Averaged turbulent kinetic energy
k_T	Thermal conductivity
M	Mach number
\mathbf{n}	Outwards normal unit vector to a surface
p	Pressure
Pr	Prandtl number
\mathbf{q}	Conductive heat flux vector
r	Radial distance
R	Polar distance
Re	Reynolds number
R_g	Specific gas constant
\mathbf{S}_t	Vector of turbulent source terms
St	Strouhal number
t	Time

$\bar{\mathbf{t}}$	Reynolds stress tensor
T	Temperature
\mathbf{u}	Velocity vector
\mathbf{U}	Vector of conservative variables
V	Volume
\mathbf{x}	Position vector

Greek symbols

Δ_i	Characteristic length of cell i
$\bar{\epsilon}$	Average dissipation rate per unit mass
Γ	Blending function for the DES model
γ	Specific heat ratio
θ	Azimuthal angle
λ	Wavelength
μ	Dynamic viscosity
ϕ	Numerical flux limiter
ρ	Density
σ_f	Filtering parameter
σ_r	Recall parameter
τ	Viscous stress tensor
$\bar{\omega}$	Average specific turbulence dissipation rate
ω	Angular frequency

Subscripts and superscripts symbols

0	Stagnation condition
c	Critical value
e	Value at the nozzle exit plane
j	Fully expanded jet conditions
k	Relative to the $k - \epsilon$ model
l	Laminar quantity
p	Referenced to the primary nozzle
s	Referenced to the secondary nozzle

t	Turbulent quantity
x'	Fluctuation of x with respect to the mean value
ω	Relative to the $k - \omega$ model
∞	Value defined at quiescent air conditions

Acronyms

BBSAN	BroadBand Shock-Associated Noise
CAA	Computational AeroAcoustics
CFD	Computational Fluid Dynamics
CFL	Courant-Friedrichs-Lewy
CNPR	Core Nozzle Pressure Ratio
DCS	Direct Computation of Sound
DES	Detached Eddy Simulation
DNS	Direct Numerical Simulation
DRP	Dispersion Relation Preserving
FNPR	Fan Nozzle Pressure Ratio
LES	Large Eddy Simulation
MUSCL	Monotone Upwind Scheme for Conservation Laws
NPR	Nozzle Pressure Ratio
NRBC	Non-Reflective Boundary Condition
OSPL	Overall Sound Pressure Level
PSD	Power Spectral Density
RANS	Reynolds Averaged Navier-Stokes
SCN	Shock-Cell Noise
TV	Total Variation
TVD	Total Variation Diminishing
URANS	Unsteady Reynolds Averaged Navier-Stokes

Chapter 1

Introduction

In modern aviation, noise emissions generated by jet engines are a subject of key importance, both in civil and military aircraft, for several reasons. In the military context, high-speed fighter aircraft feature low-bypass engines where the dominant noise source is the aerodynamic jet noise. This can feature an intense tonal noise, commonly referred to as screech. The intensity and nature of the screech noise have been identified as possible causes for material failure due to fatigue. In civil air transport, it is possible to identify two main driving objectives strictly related to jet noise: enhancing cabin comfort and reducing the impact on the environment. The demand of airlines for a quieter passenger environment together with stricter flight-crew noise-exposure regulations are the main factors to be considered for the first objective. Moreover, the trend towards replacing the aluminium fuselage skin with a carbon fibre reinforced composite, while delivering structural and manufacturing benefits, is likely to have an impact on cabin noise, due to the difference in the sound transmission loss characteristics of the lighter and directionally stiffer carbon fibre matrix composite compared to the structurally equivalent aluminium panel.

1. INTRODUCTION

Great interest in the enhancement of cabin comfort is shown by aircraft manufacturers, as this is perceived as marketable added value to their product. On the other hand, great care has to be paid to the environmental impact of aircraft noise on the airport neighbourhoods since this is a matter regulated by the International Civil Aviation Organisation and enforced by the national aviation authorities. In 2001, the Advisory Council for Aeronautics Research in Europe (ACARE) produced, with the support of several aeronautic stakeholders and governments, a document [1] containing several objectives and technological advancements to be fulfilled by aircraft manufacturers by 2020. In terms of environmental impact, main goals of this agreement were the reduction of perceived noise on ground by half, and an abatement in carbon dioxide and nitrogen oxide emissions per passenger per kilometre of 50% and 80%, respectively. These objectives were revisited in 2012 with the publication of FlightPath 2050 [2]. New limits were established for 2050 with an envisioned reduction of perceived noise by 65% with respect to average noise levels registered in 2000. These objectives motivated a sustained research and investigations on jet noise generation.

Aircraft today are 20-30 dB quieter than the first passenger jets, emitting less than 1% of the noise. Further reductions in noise emission are a real challenge. With noise shielding and acoustic absorption techniques being substantially mature, the quest is on finding methods to create aircraft engine jets that are intrinsically quieter at source. This requires enhanced modelling of the complex three-dimensional flow from dual-flux jets of turbofan engines, in which shock waves interact with turbulent structures to generate shock-associated jet noise. The work presented herein is part of the AeroTraNet2 project, a European project which gathers together universities, research centres, and industry.

1. INTRODUCTION

Framework

The present work is part of the AeroTraNet2 project, a Marie Curie Action of the European Commission's 7th Framework Programme (FP7). This 2012-2016 project aimed to build up key knowledge for developing a new physics-based shock-cell noise design tool for the aircraft industry. Shock-cell noise is a distinctive noise component that appears in turbo-fans engines at cruise conditions. Six academic partners collaborated to address the common objective of modelling shock-cell noise in a wide-body aircraft engine configuration from private sector partner Airbus France, by shock-tolerant numerical modelling for under-expanded jets (University of Leicester), large eddy simulations for turbulent jets with weak shocks (Centre Européen de Recherche et de Formation Avancée en Calcul Scientifique, CERFACS), advanced flow-noise correlations (Università degli Studi Roma Tre), jet and near-field noise experiments (von Karman Institute for Fluid Dynamics), reduced-order modelling and flow control (Institut de Mécanique des Fluides de Toulouse, IMFT-INP), and advanced laser-based measurement techniques (the Italian Ship Model Basin, CNR-INSEAN). Knowledge output was synthesized through a dedicated knowledge capturing program by the University of Greenwich, which was supported by private sector partner General Electric. In AeroTraNet2, the research output became itself object of knowledge management research, which was a novel supra-disciplinary element of this European project. AeroTraNet2 investigated three complementary approaches in a collaborative environment. The first approach was experimental. Jet and noise measurements were acquired in a newly built jet noise facility at the Von Karman Institute (VKI). They were costly and, even though the acquisition time was large, the measured locations were restricted by the limited size of the

1. INTRODUCTION

facility. The second approach was numerical. It involved the modelling of the jet by time-resolved computational fluid dynamics. These numerical simulations were able to capture the flow at any point in space within the limits of the available data storage. However, these time-marching simulations delivered a shorter flow time history than the experiment, due to the time-step restrictions of the compressible flow. The third approach, which was more analytical, aimed at obtaining reduced order models of the jet shear layer flow as perturbations of a simplified steady mean flow. By bringing these three approaches together, AeroTraNet2 aimed to deliver a contribution to the quest for quieter aircraft engines.

Objectives

The objective of this thesis is to produce and analyse aeroacoustic results from under-expanded supersonic single and dual jets with an affordable Detached Eddy Simulation (DES) numerical scheme. The main goal is to use a relatively computationally cheap numerical solver able to produce engineering accurate acoustic results related to under-expanded jets. Compared to high-order full Large Eddy Simulation (LES) predictions, the second-order time accurate and up to third-order space accurate DES approach here proposed would give a strong advantage in terms of time and computational power, using a fraction of the resources of a full LES. Whilst DES does not resolve the same wavenumber and frequency bandwidth of a wall-resolved LES, it is of interest to investigate whether sufficient shock-turbulence interaction dynamics is resolved to enable engineering accurate predictions of shock-associated jet noise. A single jet test case will firstly be discussed to evaluate the general behaviour and performance of the solver when dealing with the near-field

1. INTRODUCTION

acoustics of free jets. A dual-stream jet, more representative of the outflow from high bypass ratio turbofan engines, will then be presented to test the capabilities of the solver and to verify the feasibility of performing aeroacoustic investigations of under-expanded jets via lower-order DES numerical schemes.

Outline

The thesis is structured as follows:

- **Chapter 1:** Introduction.
- **Chapter 2:** The second chapter is meant to provide the reader with a comprehensive overview on free jets and free jet aeroacoustics from the related literature. After a description of the jet aerodynamics, the jet noise production mechanisms are introduced and described. The chapter is concluded with a discussion on computational aeroacoustics (CAA).
- **Chapter 3:** Chapter 3 describes in detail the numerical scheme used in the present work. The governing equations and their averaging in the DES approach are described, followed by a detailed summary of the time and space discretisations, boundary layer treatments, and the Message Passing Interface (MPI) code parallelisation approach.
- **Chapter 4:** The single jet test case is here presented. A description of the experimental test case and of the corresponding numerical model is given. Time-averaged and time-dependent results are then shown and discussed.
- **Chapter 5:** In this chapter, the dual jet test case is presented. At first, the experimental facility is described along with the issues that were encountered

1. INTRODUCTION

in its construction and use. A description of the numerical model follows. A detailed description and analysis of time-averaged and time-dependent results closes this chapter.

- **Chapter 6:** Conclusions.

Chapter 2

Aeroacoustics of free jets

2.1 Introduction

This chapter provides a review on jet noise generation and on its numerical modelling. First, a description of the jet aerodynamics and of the different jet topologies is given to introduce the key phenomena that take place in subsonic and supersonic jets. Then, an in-depth analysis of jet aeroacoustics is presented, with a description of the driving mechanisms of noise production as they are currently understood. The chapter concludes with a description of the major challenges for Computational Aeroacoustics (CAA) and with an overview of the currently available numerical approaches suited for this study.

2.2 Jets

A jet is a stream of fluid that is ejected from a nozzle (or an orifice) into a surrounding medium which has lower momentum. In the case of jet engines, the topology of the

2. AEROACOUSTICS OF FREE JETS

jet depends on the pressure ratio between the flow inside the engine and the ambient pressure and on the shape of the nozzle through which the flow is accelerated.

In civil aircraft applications, convergent-divergent de Laval nozzles are seldom used due to weight and space constraints. Simpler and lighter convergent nozzles are typically used for civil aircraft propulsion and their main operating conditions are briefly described here. Three different flow topologies can be observed at the exit plane of a single-stream jet:

- A perfectly expanded subsonic jet with $p_e = p_{amb}$,
- A perfectly expanded sonic jet with $p_e = p_{amb}$,
- An under-expanded sonic exit with $p_e > p_{amb}$,

where p_e is the exit pressure at the nozzle exit plane and p_{amb} is the ambient pressure. The three conditions refer to different values of the Nozzle Pressure Ratio (NPR), which is the ratio between the total pressure of the flow and the ambient pressure,

$$\text{NPR} = p_0/p_{amb} > 1. \quad (2.1)$$

An increase of the NPR determines a change in the flow conditions from subsonic to under-expanded supersonic conditions passing through the sonic state. At low values of the NPR, a subsonic flow is established inside the convergent nozzle and the conditions remain subsonic up to the exit, where the Mach number is then lower than 1. In a subsonic flow, the exit pressure always matches the ambient pressure. If the NPR is increased, the exit Mach number M_e of the bulk flow increases according

2. AEROACOUSTICS OF FREE JETS

to the isentropic relation

$$\text{NPR} = \left(1 + \frac{(\gamma - 1)}{2} M_e^2\right)^{\gamma/(\gamma-1)}, \quad (2.2)$$

where γ is the specific heat ratio. The exit Mach number increases until the sonic condition, $M_e = 1$, is attained. The second flow topology is then established, with a perfectly expanded sonic jet issuing from the nozzle. The NPR relative to this condition is defined as critical and expressed as

$$\text{NPR}_c = \left(\frac{\gamma + 1}{2}\right)^{\gamma/(\gamma-1)}. \quad (2.3)$$

From this condition, a further increase of the NPR does not affect the exit Mach number and the nozzle is defined as choked. Since the flow is not allowed to completely expand before the exit plane, the flow pressure at the exit does not match the ambient pressure and the flow is referred to as under-expanded. A further supersonic expansion takes place outside the nozzle, to the ambient pressure condition. It is possible to define the fully expanded Mach number (M_j) that a perfectly expanded jet would reach in a de Laval nozzle operating at the same NPR and express this relative to the NPR as

$$\text{NPR} = \frac{p_0}{p_{amb}} = \left(1 + \frac{\gamma - 1}{2} M_j^2\right)^{\gamma/(\gamma-1)}. \quad (2.4)$$

The typical flow topology of an under-expanded jet exiting from a convergent nozzle is shown in Figure 2.1. The velocity difference between the airflow at the nozzle exit plane and the surrounding quiescent air creates a streamwise growing shear layer forming at the nozzle lip. The under-expanded airflow from the nozzle exit

2. AEROACOUSTICS OF FREE JETS

plane expands through a fan of expansion waves generated by the surrounding lower ambient pressure. Upon reaching the shear layer, the expansion waves from the nozzle lip reflect as compression waves that focus towards the nozzle axis, creating a shock cone, as identified by the arrow in Figure 2.1. The jet core, re-compressed by the shock cone, starts a new expansion and this process repeats as a sequence of compressions and expansions. The inflected velocity profile of the shear layer is receptive to disturbances that convectively amplify, developing into large-scale instabilities, as indicated by arrows in Figure 2.1. The resulting shear-layer motion makes the shock-cell structure inside it unsteady. The sketched shock-shear-layer interaction results in noise being emitted in the surroundings. Figure 2.2 shows the

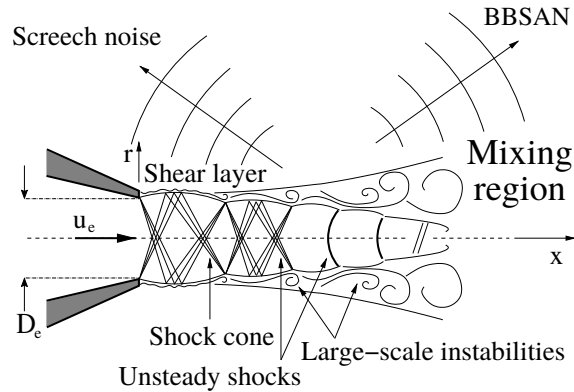


Figure 2.1: Flow features of an under-expanded jet [3].

flow topology of a $M_j = 1.15$ under-expanded jet from André [4]. The image has been obtained by means of the schlieren technique and clearly shows the features described and sketched in Figure 2.1 for an averaged flow. A first expansion, light grey area, is followed by a shock, dark grey area, and this pattern repeats in the downstream direction.

2. AEROACOUSTICS OF FREE JETS

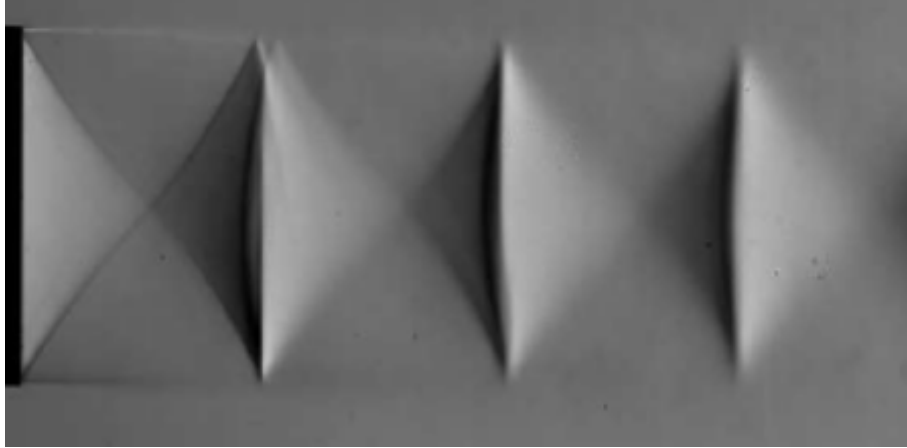


Figure 2.2: Shock-cell pattern generated by a $M_j = 1.15$ under-expanded jet from André [4].

2.3 Jet aeroacoustics

The production of noise in jets is linked to the jet flow dynamics. Two main sources of noise are identified in jets: mixing noise and shock-cell associated noise. The first component is found at $\text{NPR} > 1$ since it is related to the turbulent mixing taking place in the flow. On the other hand, shock-cell associated noise can only be observed when a shock-cell pattern appears in the jet, *i.e.* in jets where $M_j \neq M_e$. The typical spectrum of a supersonic under-expanded jet, taken in the upstream direction, is shown in Fig. 2.3. Mixing noise and shock-cell associated noise can be easily distinguished, with the latter being typically of greater intensity and covering a higher frequency range. A third feature is indicated in the picture, which is the screech noise peak. Screech is a phenomenon linked to the presence of shock cells in the flow and only appears in certain conditions. It will be further described in Section 2.3.2.2.

2. AEROACOUSTICS OF FREE JETS

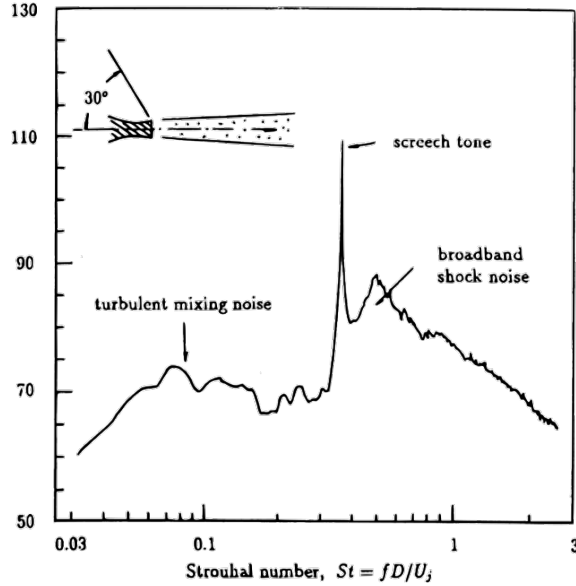


Figure 2.3: Typical far-field supersonic jet noise spectrum acquired at 150° from the downstream direction, from Tam [5].

2.3.1 Jet mixing noise

Jet mixing noise is produced by turbulent mixing taking place in the flow [6]. Turbulence developing in free jets can be divided into two categories [7]: fine and large scale turbulence. A shear layer forms from the nozzle inner lip at the nozzle exit and large-scale instabilities are convected within it. These large-scale instabilities, or eddies, maintain a coherent structure up to where they reach a size of the order of the nozzle exit diameter. Concurrently, fine-scale turbulent structures in the shear layer tend to break into smaller structures until their length scale is such that dissipation phenomena suppress them. The fine-scale turbulence is to be considered as a compact source of noise since its length scale is typically smaller than the emitted sound wavelength. Fine-scale turbulence produces a broadband noise component due to the chaotic motion of the flow. Its contribution is omnidirectional, with a downstream preponderance. However, due to the non-uniformity of the jet,

2. AEROACOUSTICS OF FREE JETS

the waves undergo refraction effects that impact on the directivity of the produced sound, generating a relatively quiet zone in the downstream direction known as the ‘cone of silence’. On the other hand, the large-scale turbulence has typical length scales that are of the same order of magnitude as the emitted sound wavelength and is thus considered as a non-compact source of noise. Its component appears as a broad peak in the spectrum and, due to the downstream convection of the eddies, this noise contribution exhibits a directional preference, mainly radiating in the downstream direction.

Tam and Golebiowski [8] supported this separation of scales defining similarity spectra for both components. The combined similarity spectrum is given by

$$S = \left[A \cdot F \left(\frac{f}{f_L} \right) + B \cdot G \left(\frac{f}{f_F} \right) \right] \left(\frac{D_j}{r} \right)^2, \quad (2.5)$$

where $F(f/f_L)$ and $G(f/f_F)$ are the similarity spectra corresponding to the large and fine turbulence scales respectively, f_L and f_F are the peak frequencies of said spectra, which are functions of the jet operating parameters, and A and B are the amplitudes of the independent spectra with same dimensions as S , as reported in [8]. In the downstream direction, where the large-scale emission is dominant, parameter B can be set to zero, thus simplifying the expression. Conversely, in the upstream direction, where the fine-scales are dominant, parameter A can be set to zero. Tam and Golebiowski [8] proposed two similarity spectrum functions $F(f/f_L)$ and $G(f/f_F)$ applicable to noise from an axisymmetric jet radiated at any inlet angle regardless of the jet Mach number M_j and of the jet to ambient temperature ratio. The two similarity spectrum functions, determined at first empirically, were cross-checked against the entire range of Mach number and temperature ratio available

2. AEROACOUSTICS OF FREE JETS

at the time at NASA Langley, which gave a good match [8].

2.3.2 Shock-associated noise

Shock-associated noise, as stated in Section 2.3, only appears with imperfectly expanded supersonic jets where a shock-cell pattern is observed. Emission levels of shock-cell noise are typically around 10dB higher than their mixing noise counterpart. Two components are identified in shock-associated noise: a broadband component, which is known as Broadband Shock Associated Noise (BBSAN) and it is present in all imperfectly expanded jets, and a tonal component, called screech noise, that only appears under certain conditions.

2.3.2.1 Broadband Shock-Associated Noise

Broadband Shock Associated Noise was identified for the first time by Harper-Bourne and Fisher [9] in 1973, prompting to a number of experimental investigations. The generation of BBSAN was attributed by Tam and Tanna [10] to the weak interaction between the downstream propagating large turbulence structures of the shear layer and the quasi-periodic shock-cell structures, causing the coherent scattering of these vortical structures. On the basis of this idea, Tam described such interaction by developing a stochastic model in a first paper in 1987 [11]. In its first formulation, the model was capable of predicting the near and far field spectra of slightly imperfectly expanded jets. In 1990, Tam [12] extended the formulae to the moderately imperfectly expanded jets. The original model [11] was based on the assumption that the large turbulence structures/instability waves and the shock cells are independent entities and they can be modelled separately. The approach was focused on the analysis of the interaction of these instabilities as they propa-

2. AEROACOUSTICS OF FREE JETS

gate through the shock-cell structure. In his 1987 approach, Tam used a stochastic model developed in a previous work by Tam and Chen [13] to provide a description of the spatial and temporal evolution of the vortical structures in the mixing layer of the jet. In this model, the structures were represented by a superposition of the intrinsic (instability) wave modes of the flow. The amplitudes of the wave modes were treated as stochastic functions possessing similarity properties. By implementing these concepts, the model was able to calculate the spatial distributions of the turbulent Reynolds stresses, the intensities of the turbulent velocity components, and the spectral contents.

To model the quasi-periodic shock-cell structure, Tam relied on the approach developed in the work by Tam, Jackson and Seiner [14]. Such approach was based on the observation that, in a sense, the shocks and expansion fans are trapped inside the jet, by interior wave reflection at the shear layer, and form more or less a steady wave pattern. This can be regarded as the jet plume acting as a waveguide for these disturbances and, on the basis of this idea, Tam *et al.* [14] decomposed the structure into the stationary waveguide of Fourier modes of the jet mean flow using multiple-scales expansion. By decomposing the flow variables associated with the shock cells into waveguide modes, the wavelengths of the modes are not exact integer multiples of each other and the passage of the large turbulence structures through the shock cells produces interactions between the broad spectrum of wave-like disturbances and each of the individual waveguide modes of the shock cells. Since the wavelength of each waveguide mode is different, its scattering properties are not the same. As a result, the principal direction of noise radiation and the spectral content of the radiated noise associated with different modes are different. In the far field, the noise intensity is the sum of the noise generated by each of the modes. Hence,

2. AEROACOUSTICS OF FREE JETS

the noise spectrum at a point is made up of a superposition of many sub-spectra, each generated by a waveguide mode of the quasi-periodic shock cell structure. In other words, in the framework of this model of BBSAN, the noise spectrum could exhibit more than one spectral peak, a characteristic which differs markedly from turbulent mixing noise. This characteristic finds confirmation in the observations of Tam, Seiner and Yu [15] who found that BBSAN is made up of a superposition of many spectral peaks.

As previously stated, the original method by Tam [11] was only valid for mildly imperfectly expanded jets. The extension of the method by Tam [12] was possible upon observing that, over the wider Mach number range of moderately imperfectly expanded jets, the quasi-periodic shock-cell structure has a strong resemblance to that of mildly imperfectly expanded jets. Furthermore, the shock noise intensity depends only on the amplitude of the quasi-periodic shock-cell structure but it is relatively insensitive to the amplitude of the strong first shock. Being the BBSAN generation relatively independent from the first shock and due to the aforementioned similarity in the quasi-periodic structures, the prediction formulae are easily extended, provided that the appropriate shock cell waveguide mode amplitudes are used. In his work, Tam provided equations capable of accurately predicting noise in the near and far field for both under- and over-expanded jets, cold and hot. The approach was validated against a vast set of experimental data, providing good match over the entire moderately imperfectly expanded Mach number range. These results accredited the hypotheses made on the BBSAN production mechanisms.

2. AEROACOUSTICS OF FREE JETS

2.3.2.2 Screech Tonal Noise

While the presence of the shock-cell pattern is inherently linked to the production of broadband shock-cell noise, the conditions necessary for the onset of the tonal noise, screech, are not easily and commonly observed. Depending on the flow conditions, such as the Mach number and the temperature, and on the environment in which the jet is discharged, with particular reference to the presence of surfaces around the nozzle exit plane and the nozzle lip geometry, screech may or may not appear and may or may not present some of its harmonics. Moreover, if the BBSAN is a well understood phenomenon that can be successfully predicted both in frequency and amplitude in single-stream jets, models able to predict the intensity of screech noise are still elusive.

The generation of screech is, in principle, similar to that of the BBSAN as it stems from the interaction between the convected instabilities and the shock cells. However, in the case of screech, the selection of convectively amplifying shear-layer instabilities by upstream feedback locks the noise generation process in a feedback loop, which determines the tonal characteristic of screech. The first studies on screech noise appeared in the early fifties with Powell [16] who made the discovery of screech based solely on the observation of schlieren flow visualizations.

Powell was the first to detect the upstream directivity of the shock noise which appeared to contradict the conception that the interaction between the jet instabilities and the shock cells produced monopoles at the jet edges. Powell [16] was able to resolve this incongruence by modelling the sources as a phased array of regularly spaced monopoles with the directionality being dependent on the phase difference between the sources. He defined empirical formulae for the directivity pattern of

2. AEROACOUSTICS OF FREE JETS

the screech main lobes as

$$D_f = \frac{1}{3} + \frac{2}{3} \cos \{2\pi(L/\lambda)[1 - M_c \cos(\alpha)]\} \quad (2.6)$$

and

$$D_h = \frac{1}{3} + \frac{2}{3} \cos \{4\pi(L/\lambda)(1 - M_c \cos(\alpha))\} \quad (2.7)$$

for the fundamental and harmonic tones respectively. In Equation (2.6) and Equation (2.7), L is the shock-cell spacing, α the angle measured with respect to the downstream direction, and M_c and λ are the convective Mach number and the wavelength of the disturbance respectively. The peak directivity of the fundamental tone is in the upstream direction ($\alpha = 180^\circ$) whereas, for the harmonics, it is at 90° . The frequency of the fundamental tone can be approximated with a simple formula, and is given by

$$f = \frac{U_c}{s(1 + M_c)}, \quad (2.8)$$

where U_c is the convection velocity of the shear-layer structures and s is the shock spacing. Even if Equation (2.8) looks extremely simple, it relies on the accurate determination of U_c and s . As first approximation, U_c can be taken as $0.7 U_j$ [9], being U_j the fully expanded jet velocity, while the shock spacing of the i^{th} shock cell can be expressed by means of Prandtl [17] and Pack [18] formulation as

$$s_i \approx \frac{2\pi}{k_i} = \pi(M_j^2 - 1)^{1/2} \frac{D_j}{\sigma_i}, \quad (2.9)$$

where D_j and M_j are the fully-expanded jet diameter and Mach number respectively, and σ_i are the zeros of the Bessel function of order 0 of the first kind.

Two fundamental concepts are expressed in Powell's approach: first, the phase cri-

2. AEROACOUSTICS OF FREE JETS

terion requires that the sum of the time needed for the convection of downstream travelling hydrodynamic instabilities and the time for upstream travelling disturbances to reach the nozzle lip has to be an integer multiple of the screech cycle period, and second, the amplitude criterion requires the sound directivity to show a maximum in the upstream direction [19].

Interestingly, Panda [20] obtained Prandtl's equation (2.8) while observing standing wave patterns outside the jet shear layer. Panda suggested that a standing wave pattern is to be expected in supersonic screeching jets with a resultant wavenumber $k_{sw} = k_s + k_h$. Such pattern is generated by the interference between downstream propagating hydrodynamic fluctuations k_h and upstream propagating acoustic waves k_s . The wavelength of the standing wave is defined as

$$\frac{1}{L_{sw}} = \frac{1}{\lambda_s} + \frac{1}{\lambda_h}, \quad (2.10)$$

where λ_s and λ_h are the wavelength of the acoustic wave and that of the hydrodynamic fluctuations respectively. Since $\lambda_s = a_\infty/f_s$ and $\lambda_h = u_c/f_s$, where a_∞ is the ambient speed of sound, and u_c is the convective speed of the hydrodynamic disturbances, it is possible to rewrite this equation as

$$f = \frac{u_c}{L_{sw}(1 + u_c/a_\infty)}, \quad (2.11)$$

which is equivalent to Equation (2.8) with the wavelength of the standing wave replacing the shock spacing. Panda *et al.* [21] showed that this relationship is valid for circular, rectangular, and elliptic jets. It has to be noted that the occurrence of a standing wave formation is not specific to the case of a shock-containing screeching

2. AEROACOUSTICS OF FREE JETS

jet. Lepicovsky and Ahuja [22] have shown that a standing wave also exists, for example, in the near field for a subsonic edgetone situation.

Tam, Seiner and Yu [15] improved Equation (2.8) in order to take into account temperature effects. The frequency can then be expressed as

$$f = \frac{U_c}{L_s} \left[1 + M_c \left(1 + \frac{\gamma - 1}{2} M_j^2 \right)^{-1/2} \left(\frac{T_r}{T_\infty} \right)^{1/2} \right]^{-1}, \quad (2.12)$$

where T_r is the total temperature of the jet and T_∞ is the ambient temperature.

Following the description of Raman [19] and Tam [23], screech can be described as the concurrent action of four key mechanisms, reported in Fig. 2.4: (1) instability wave growth, (2) instability-shock interaction, (3) acoustic feedback, and (4) receptivity process (*i.e.* coupling of hydrodynamic and acoustic disturbances).

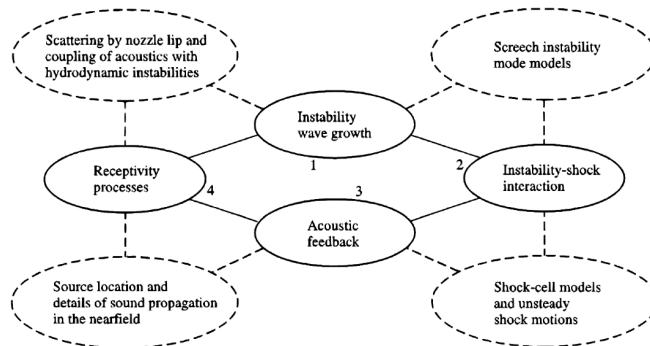


Figure 2.4: Schematic diagram of resonant screech loop (solid lines) and associated phenomena (dashed lines), from Raman [19].

The first step in the screech loop is the instability wave growth. The exponential growth of instability modes usually encountered in shear layers of free jets is significantly altered in shock containing jets and it is made more complex. Several factors could be responsible for the acceleration, the deceleration, and the modulation of the instability waves. A first factor to take into account is that the shock train produces

2. AEROACOUSTICS OF FREE JETS

an alternating divergent and convergent flow boundary. As the flow accelerates and decelerates passing through the shock cells, it is reasonable to assume that the disturbance velocity would exhibit a similar behaviour. This modulation effect is clearly visible, for example, in the data of Raman and Rice [24] shown in Figure 2.5. It is evident that the shocks significantly modulate the amplitude of the velocity fluctuations, as indicated by the dips before the shocks followed by a downstream recovery. The evolution is highly non-linear and it is difficult to identify, in the pattern, a streamwise region where an exponential growth of the velocity disturbances takes place according to the linear theory. Such observations lead to questions about the applicability of linear stability analysis for jets exhibiting screech and highlight the complex nature of screech. Even though the growth rate is modified by the

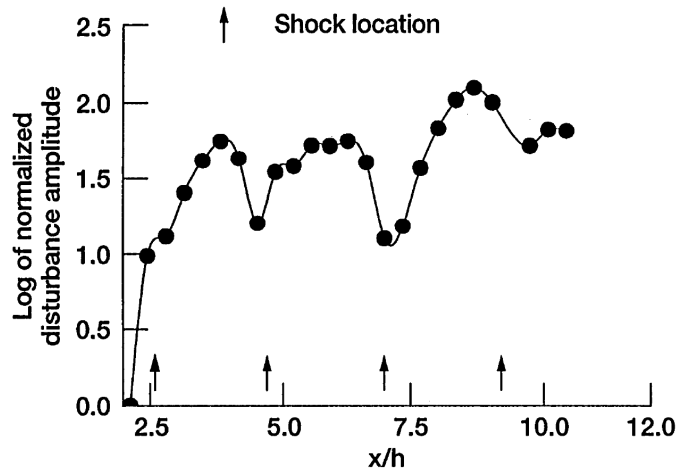


Figure 2.5: Evidence of instability wave modulation by shocks in a rectangular jet, $M_j = 1.44$, from Raman and Rice [24].

shock cells, instabilities need to grow up to a certain amplitude in order to effectively interact with the shocks, usually reaching sufficient dimensions between the 3rd and the 5th shock cell.

2. AEROACOUSTICS OF FREE JETS

The second step in the screech instability loop is the interaction of the shear-layer instabilities with the shock cells. One of the key aspects for the accurate predictions of screech is the correct prediction of the shock-cell spacings. The frequency of screech emission, as shown in Equation (2.8), is proportional to the inverse of the shock-cell length. For this reason, models able to accurately predict the shock-cell spacing are required. Some examples are the Prandtl model, previously introduced with Equation (2.9), or the model developed by Tam, Jackson and Seiner [14] which solves an eigenfunction expansion of a modelled shock-cell system inside a jet surrounded by a vortex sheet. By means of this model, Tam [25] was able to give approximate predictions of the shock spacing for rectangular and non-axisymmetric supersonic jets. Morris *et al.* [26] solved the same eigenfunction problem but using a boundary element method capable of dealing with nozzles of arbitrary cross-section. They also studied the impact of the finite thickness of the mixing layer, finding that its effect is the reduction of the shock spacing by 20% over the length of the potential core. However, better modelling to characterize the shock-cell spacing is required in order to take into account non-uniformities in the shock cells in the unsteady flow. Starting from the third shock cell, shocks are subject to noticeable motion inside the potential core, due to the turbulent structures that are convected downstream from the nozzle lip. These structures shape the potential cone of the jet, influencing the shock structures contained within it.

The final steps in the screech loop require the sound generated downstream to propagate to the nozzle lip (feedback) and couple with the hydrodynamic disturbances in the shear layer (the process of receptivity). Through receptivity, large amplitude acoustic perturbations are able to act on the flow instabilities. This process is analogous to the transition of a laminar boundary layer in which free-stream

2. AEROACOUSTICS OF FREE JETS

perturbations entering in it are amplified, initiating transition to turbulence. The large-amplitude acoustic disturbances act like a forcing term at the origin of the shear layer, the nozzle lip, generating hydrodynamic structures that are convected downstream. The nozzle lip thickness is a crucial parameter and Norum [27] showed that the thickening of the nozzle lip can increase screech noise intensity of up to $10dB$. The newly generated structures eventually interact with the shock cells closing the feedback loop. An accurate description of the acoustic near field is of key importance for the understanding of feedback and receptivity phenomena and numerous detailed experimental measurements are available in literature [28, 29, 30, 31]. In these studies, the receptivity is in places referred to as the interaction of large-amplitude acoustic waves with the shear-layer at the nozzle lip. Canonic acoustic waves are small-amplitude perturbations that satisfy the linear acoustic momentum equation. In the context of the nozzle lip receptivity, the term acoustic refers to the upstream radiating character of such waves, which are of finite-amplitude and therefore exhibit non-linear propagating characteristics at a group velocity that is approximated to the ambient speed of sound.

As observed by Krothapalli *et al.* [32], the dominant acoustic centre is located at the third shock cell, with a shift towards the fourth cell when the Mach number increases. Suda *et al.* [33] experimentally observed travelling waves inside the third shock cell of over-expanded jets. They attributed the production of screech noise to the evolution of such waves. Panda [34] confirmed the downstream motion of the shock centre by means of laser shock detection techniques. With the passage of each vortex, the shock centre moves downstream. During its drifting, the shock weakens and eventually disappear while another shock appears upstream replacing it. This new shock is originated from the opposite side of the shear layer. This

2. AEROACOUSTICS OF FREE JETS

process is shown in the sketch in Fig. 2.6 by Suda, Manning and Kaji [33]. The anchor point A , moves forward to the point A' and then point B moves backward until the starting position is reached.

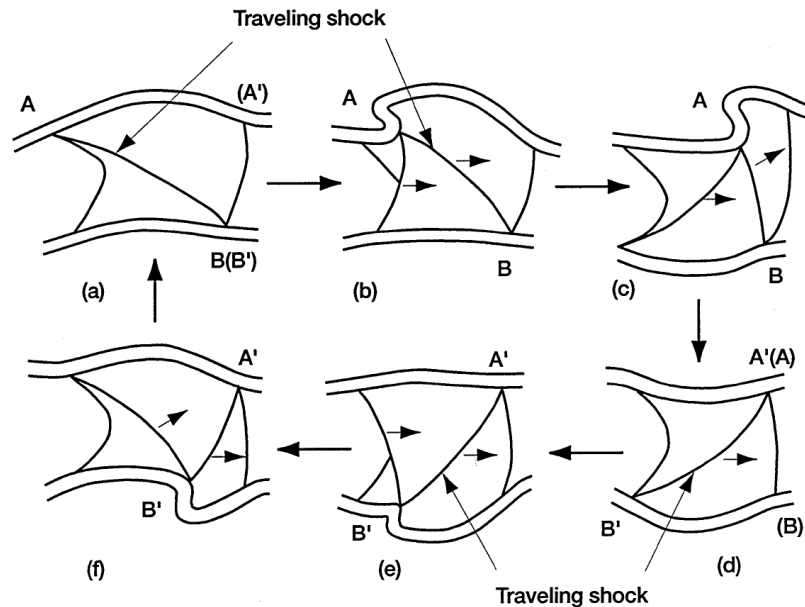


Figure 2.6: Dynamic motion of the travelling shock in the third shock cells from Suda *et al.* [33].

Interesting progresses towards the understanding of screech have been made in the past years thanks to numerical investigations. In 2003, Suzuki and Lele [35] introduced the concept of shock leakage. Shock leakage occurs near the saddle point of vortices convected downstream in the mixing layer (see Figure 2.7). They showed that, if instabilities are large enough and present a clear saddle point, shock waves are able to leak through the mixing layer. Lui and Lele [36] studied, via a Direct Numerical Simulation (DNS), the test case of a shock impinging into a shear layer and bouncing back as an expansion wave. They confirmed the presence of shock leakage and the omni-directionality of shock-associated noise emitting from

2. AEROACOUSTICS OF FREE JETS

the shock tip.

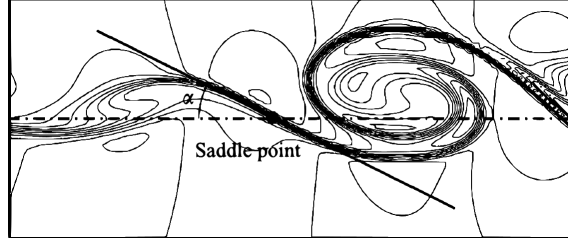


Figure 2.7: Slope of the temperature contour with saddle point from Suzuki and Lele [35].

As final remarks, it has to be noted that the screech amplitude and oscillations increase with flight velocity [37] (*i.e.* the velocity of the flow outside the jet) and that the amplitude of the screech decreases with temperature [15]. However, for a given flow temperature, screech intensity is independent of the shock strength, *i.e.* is independent of the jet M_j . A minimum shock strength is needed to originate screech, but the amplitude does not vary once screech appears. On the other hand, for high Mach numbers, screech is not developed. For further reading on screech noise, the reader is referred to Raman's extensive review [38] on this subject.

2.3.3 Coaxial Jets

The generation of noise in coaxial jets is driven by the same mechanisms described in the previous sections for single-stream jets. The flow topologies, although different, present strong similarities. Conceptually, it is possible to isolate three distinct noise sources: the inner shear layer between the primary and secondary streams, the outer shear layer between the secondary jet and the ambient, and the fully merged jet farther downstream. Each of these sources has characteristic length and velocity scales that differ from one another. Different configurations can be studied for coaxial jets,

2. AEROACOUSTICS OF FREE JETS

depending on the flow conditions of the primary and secondary jet. Conventionally, the primary jet is the inner one, while the secondary is the one surrounding the primary flow. Several works can be found in literature on the different configurations. Dahl, Papamoschou and Hixon [39] performed numerical and experimental studies on supersonic perfectly expanded coaxial jets at different operating conditions, maintaining constant thrust and mass flow. As described in Section 2.3.1, in a fully expanded jet, noise is generated by turbulent mixing. Dahl *et al.* [39] showed that the measured mixing noise spectra can be characterized by the same similarity spectra that Tam *et al.* [8] used to characterize single-stream supersonic jets. It appears that, with both subsonic and supersonic secondary flows, large-scale structures are responsible for the dominant noise component in the downstream direction of the jet. Moreover, using instability wave analysis, they determined that such noise component is generated by instability waves developed in the inner shear layer and achieving their maximum amplitude downstream of the outer potential core, where the shear layers of the two streams merge.

Murakami and Papamoschou [40, 41] studied the case where the primary jet is supersonic and the secondary is subsonic. They focused on the analysis of potential core stretching, shear-layer growth rate, and entrainment. They showed that the secondary flow reduces the growth rate of the primary shear layer and elongates the primary jet potential core. They also provided a semi-empirical model to evaluate the lengths of both primary and secondary potential cores. Viswanathan [42] performed a parametric study for a number of conditions. For configurations with a supersonic primary jet and subsonic or low supersonic secondary jet, he observed that the noise from the primary jet drives the total noise production. The noise from the secondary shear layer is negligible when strong shocks are established in

2. AEROACOUSTICS OF FREE JETS

the primary jet and an increase in the primary jet velocity is responsible for a noticeable increase in noise production at high frequencies especially in the range between 120° and 135° , as shown in Figure 2.8. The shock-associated noise is dominant for all angles and has characteristics similar to those of single jet BBSAN.

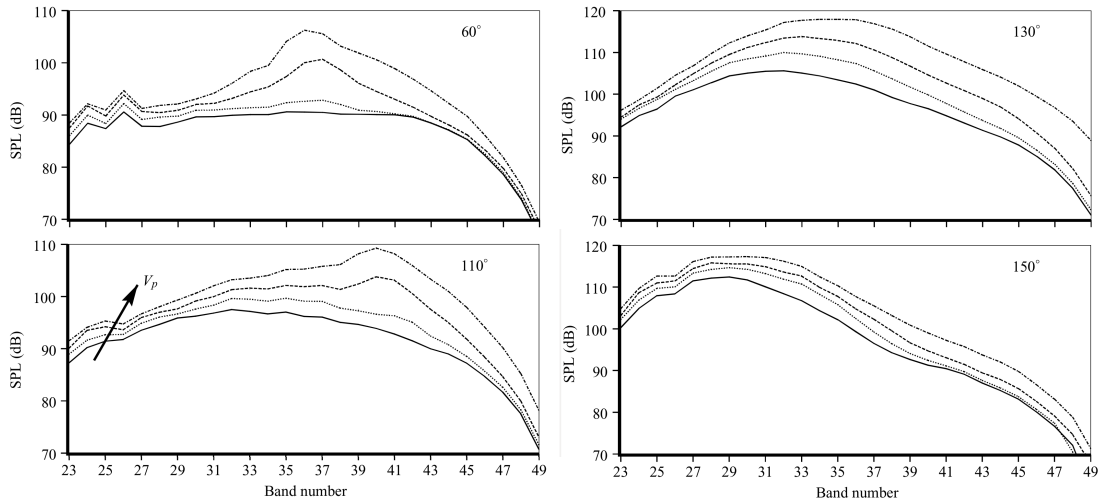


Figure 2.8: Spectral variation due to change in supersonic primary stream with fixed subsonic secondary jet conditions [42].

When a supersonic secondary flow is present, the directivity and the noise spectra are significantly different as shown in Figure 2.9. Viswanathan [42] reported for the first time that a strong radiation of shock-associated noise to large aft angles (downstream direction) is observed, with its intensity increasing with increasing Mach number of the secondary stream, regardless of the primary flow Mach number. At the same time, a contribution from shock associated noise to the forward quadrant becomes evident. Supersonic secondary jets strongly deviate in behaviour from single jets and coaxial jets with supersonic primary streams. In his work, Viswanathan [42], also studied the effects of temperature and of forward flight on the noise emission.

2. AEROACOUSTICS OF FREE JETS

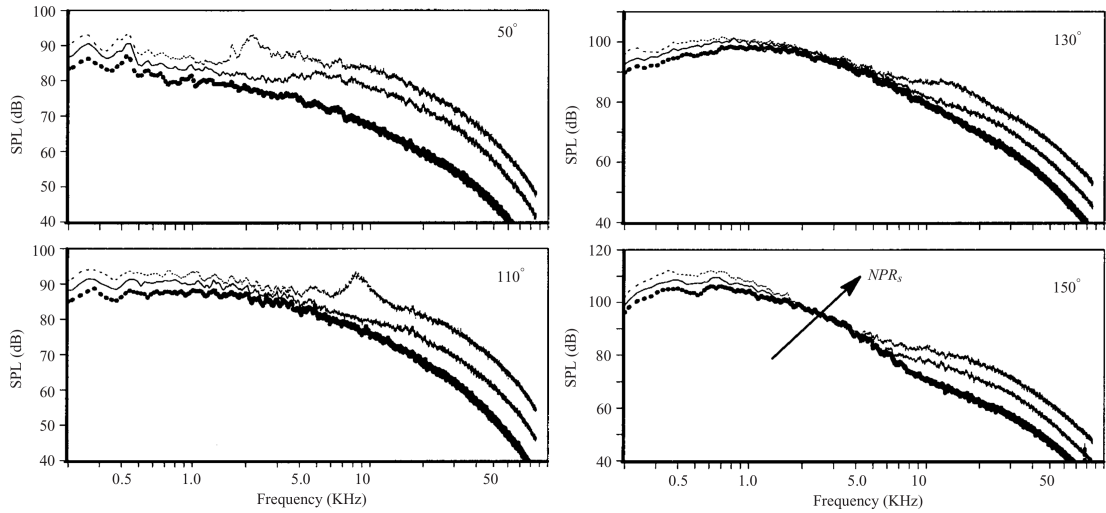


Figure 2.9: Spectral variation due to change in supersonic primary stream with fixed subsonic secondary jet conditions [42].

In this work, the flow topology of interest consists of a subsonic primary jet surrounded by a supersonic under-expanded flow. A simplified sketch of the flow topology is shown in Figure 2.3.3. The imposed flow conditions determine the appearance of a shock-cell system in the secondary flow. Two shear layers are formed, the first due to the interaction between the primary jet and the secondary jet, and the second generated by the secondary stream interacting with the ambient air. In this config-

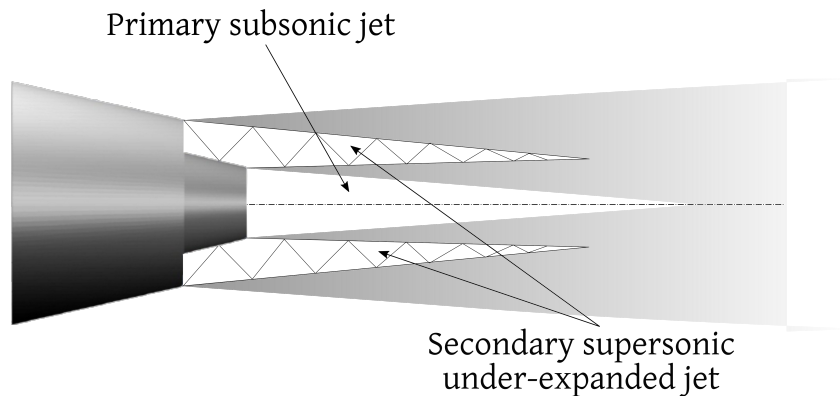


Figure 2.10: Sketch of the shock-cell pattern generated by a dual jet with an under-expanded secondary stream and a subsonic primary stream.

2. AEROACOUSTICS OF FREE JETS

uration, the BBSAN noise, produced by the interaction of large turbulent structures and shock cells, presents a more complicated noise generation mechanism. Being the supersonic under-expanded flow surrounded by two shear layers, it is expected that BBSAN sources would double. Abdelhamid and Ganz [43] corroborated this idea observing that high frequency components developed in the primary shear layer, *i.e.* at the boundary of the inner one, while low frequency components originated in the secondary shear layer. Tam, Pastouchenko and Viswanathan [44] confirmed these

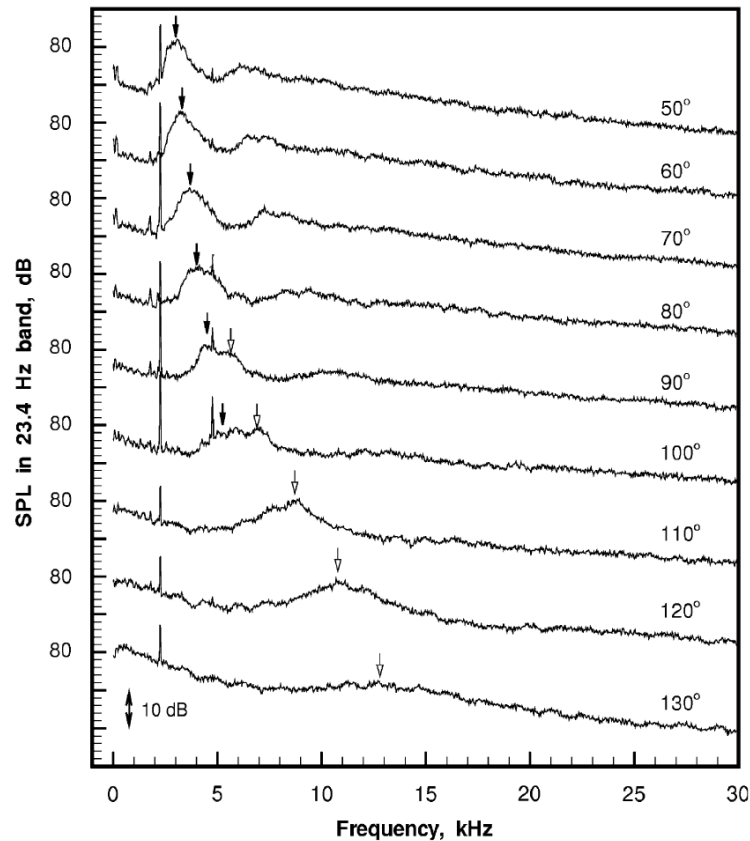


Figure 2.11: Noise spectra of a dual stream jet at 10° interval. Subsonic primary jet $M_p = 0.72$ and supersonic under-expanded secondary jet $M_s = 1.36$ from Tam *et al.* in [44]. Black arrows indicate the first component of broadband shock-cell noise and open arrows indicate the second component.

2. AEROACOUSTICS OF FREE JETS

findings as shown in Figure 2.3.3. The first component has characteristics that are very similar to those of single-stream supersonic jets, with the noise that is radiated primarily in the upstream direction and that decreases in intensity as the inlet angle increases. With the development of a vortex sheet model for the dual-stream jet, Tam *et al.* [44] were able to give a physical explanation for this roll-off phenomenon. The source responsible for sound radiation in the primary shear layer moves at a subsonic speed relative to the supersonic secondary jet. This causes the disturbances to decay exponentially when transmitting through the secondary jet, thus experiencing a significant reduction in the noise radiation amplitude. The modelled roll-off phenomenon proved to be in agreement with the experimental observations. The second component is instead very different to what observed in single jets. It mainly radiates in the downstream direction and the noise intensity is low at 90° , increasing as the inlet angle increases.

The interest in coaxial jets is understandably high, since modern commercial aircraft engines are almost exclusively bypass turbofan jet engines. Alongside experimental campaigns [42, 45, 46, 47], in the last few years a number of numerical investigations have arisen which tackled the study of coaxial jets using the LES approach [48, 49, 50, 51, 52, 53].

2.4 Computational Aeroacoustics (CAA)

Sound, being a vibration that propagates through a medium, is, by definition, an unsteady process; thus no sound can be produced by a steady flow. The amplitude of the acoustic waves generated by the fluid motion are usually several orders of magnitude smaller than the strongest pressure waves in the flow. For example, for

2. AEROACOUSTICS OF FREE JETS

a Mach=1.5 jet, the velocity fluctuations of the radiated sound are four orders of magnitude smaller than the mean flow pressure [5]. Therefore, in order to be able to compute acoustic waves and sound phenomena, not only an unsteady calculation is needed, but it is also necessary that the numerical model and machine related errors be lower than the acoustic perturbations. Numerical errors can lead to the overestimation of the noise generated aerodynamically, since the acoustic efficiency is very low even in loud flows [54]. Moreover, propagation of acoustic waves over long distances may occur with a very low attenuation for coherently propagating waves [55]. Artificial dissipation and dispersion effects inherent to numerical schemes have to be kept as low as possible, in order to limit the decay in amplitude and the phase shift of sound waves.

Resolving all the scales of turbulence and frequencies of the problem is, in principle, required in order to capture all the frequency components of the sound generated by a flow field. In practice, such approach is prohibitively expensive as the computational cost would be enormous, thus only a certain range of scales can be directly resolved. Numerical methodologies can be grouped according to the range of spatial and temporal scales that are explicitly represented in the simulation. The influence of the phenomena that are not directly captured requires modelling. Colonius [55] classifies the currently available approaches in CAA into two categories: direct computation of sound and hybrid methods.

The methods that fall under the direct computation of sound (DCS) category aim to compute both the unsteady flow of the problem and the sound it generates. In this approach, the computational domain must contain the noise-producing region of the flow and at least part of the near field where the noise is radiated and can then be measured. The computational mesh has to be designed in order to correctly

2. AEROACOUSTICS OF FREE JETS

capture both the flow features and the sound waves. Due to computational and time constraints linked to the dimensions of the required meshes, a DCS approach implementing full DNS simulations is not suitable for actual industrial problems, but it is usually adopted to obtain insights on the underlying sound generation processes. It has to be noted that, thanks to great improvements in available computational power, DCS studies with DNS progressed from very simple idealised cases, as co-rotating vortices [56], to nearly complete flow regions, ranging from a supersonic jet [57] to a supersonic shear layer with a lip [58]. The above mentioned studies on shock leakage phenomena by Suzuki and Lele [35] and the work of Lui and Lele [36] are two other examples of DCS-DNS analyses.

Less expensive than DNS analyses, are Large Eddy Simulations (LES). In an LES approach, only a given range of energy-containing eddies is captured. The motion of smaller scales and their effect on the resolved ones are modelled by means of subgrid scale (SGS) models. The cost of LES computations is much lower with respect to DNS and they guarantee a good trade-off in terms of result quality. Several full subsonic jet LES studies can be found in literature ([59, 60, 61, 62, 63, 64, 65] among others) that provided insight in the noise generation mechanisms. Bogey, Bailly and Juvé [59] found that, for a subsonic LES jet simulation at $M_e = 0.9$ and $Re = 65000$, the generation of sound is related to the breakdown of the shear layer in the central zone of the jet. Bodony and Lele [60] studied the temperature effects on the noise production obtaining good agreement with experimental data. Bogey and Bailly [61] studied the impact of different inflow forcing conditions on the flow development and on the sound field concluding that if a forced ring vortex is used, involving several azimuthal modes, the first four modes have the strongest impact; by removing them, turbulence intensity is reduced, thus obtaining a quieter

2. AEROACOUSTICS OF FREE JETS

flow. Regarding supersonic jets, Schulze and Sesterhenn [66] and Berland *et al.* [67] simulated a three-dimensional (3D) supersonic under-expanded planar jet. Berland *et al.* [67] were able to observe the shock-leakage phenomenon reported by Suzuki and Lele [35] for a real jet, showing the shock-vortex interactions taking place in the third shock cell.

The second class of methods identified by Colonius [55], the hybrid methods, relies on a second calculation to predict the noise on the basis of results obtained via a main simulation which provides the flow dynamics of the problem. This second computation can be performed a posteriori or in parallel with the main computation. DNS and LES simulations, as well as Unsteady RANS simulations, can be used to compute the sound sources that will be used for the implementation of an acoustic analogy. Bailly [68] computed the noise of subsonic and supersonic jets from statistical source models combining a $k - \epsilon$ RANS model with an acoustic analogy. Colonius [69] compared DNS and Lilley's analogy based on the DNS sources on the sound generated by a vortex pairing in a two-dimensional compressible mixing layer. Vortex methods can also be used in conjunction with the acoustic analogies in order to reduce the computational time [70, 71]. Vortex methods provide a quick assessment of the impact of the main variables on the radiated noise. Their principal attraction for CAA is that they provide a dynamic model of the unsteady, essentially inviscid, flow at a reduced cost. Another hybrid approach requires the numerical solution of the linearised Euler equations (LEE) with specific source-terms [72] or projected source-terms [73] in order to extend the near-field compressible flow data to the radiated acoustic field.

For further information, the reader is referred to the comprehensive review of Colonius [55] on CAA methods.

Chapter 3

Methodology

3.1 Introduction

This chapter presents the numerical scheme, the boundary conditions, and the numerical techniques used to simulate the jets described in the previous chapter. The first part describes the governing equations for Newtonian fluids and their spatial and temporal discretisation. A description of the boundary conditions implemented inside the in-house finite-volume scheme Cosmic follows along with a description of the sponge layer treatment. To conclude, a synthetic description of the domain decomposition, the parallelisation of the code by MPI, and its validation are given.

3.2 Governing equations

The fluids being studied in the present work are Newtonian and non-reactive. Under these conditions, the governing equations for fluid flows are the time-dependent

3. METHODOLOGY

Navier-Stokes (N-S) equations that can be expressed in the following form:

$$\frac{\partial \mathbf{U}}{\partial t} + \nabla \cdot \mathbf{F} = \nabla \cdot \mathbf{F}_v, \quad (3.1)$$

where \mathbf{U} is the vector of conservative variables, \mathbf{F} the inviscid flux vector, and \mathbf{F}_v the viscous flux vector, which are defined, respectively, as:

$$\mathbf{U} = \begin{pmatrix} \rho \\ \rho \mathbf{u} \\ \rho e_0 \end{pmatrix}, \quad \mathbf{F} = \begin{pmatrix} \rho \mathbf{u} \\ \rho \mathbf{u} \otimes \mathbf{u} + p \mathbf{I} \\ \rho \mathbf{u} (e_0 + p/\rho) \end{pmatrix}, \quad \mathbf{F}_v = \begin{pmatrix} 0 \\ \boldsymbol{\tau} \\ \mathbf{u} \cdot \boldsymbol{\tau} - \mathbf{q} \end{pmatrix}, \quad (3.2)$$

where ρ is the density, \mathbf{u} is the velocity vector, e_0 is the specific total energy, p is the static pressure, $\boldsymbol{\tau}$ is the viscous stress tensor, \mathbf{q} is the convective heat flux vector, \otimes is the dyadic product and \mathbf{I} is the identity matrix. The three rows in Equation (3.2) refer to mass, momentum, and energy conservation respectively. The ideal gas hypothesis holds for the flows of interest by which the equation of state is

$$p = \rho R_g T, \quad (3.3)$$

where R_g is the specific gas constant which, for dry air, assumes the value $R_g = 287.058 \text{ J kg}^{-1} \text{ K}^{-1}$. The total energy e_0 is

$$e_0 = \frac{1}{\gamma - 1} R_g T + \frac{1}{2} \mathbf{u} \cdot \mathbf{u}, \quad (3.4)$$

3. METHODOLOGY

where γ is the ratio of specific heats and T is the absolute temperature. The viscous stress tensor is defined as

$$\boldsymbol{\tau} = \mu_l (\nabla \mathbf{u} + \mathbf{u} \otimes \nabla - 2/3 \mathbf{I} \nabla \cdot \mathbf{u}), \quad (3.5)$$

where μ_l is the molecular viscosity. The conductive heat flux vector is defined as

$$\mathbf{q} = -k_T \nabla T, \quad (3.6)$$

where k_T is the thermal conductivity. Two additional algebraic relations have to be introduced for the molecular viscosity and the thermal conductivity in order to solve the second-order partial differential equation system (3.1):

$$\mu_l = 1.458 \times 10^{-6} \frac{T^{3/2}}{(T + 110.4)} \quad [\text{kg m}^{-1} \text{s}^{-1}], \quad (3.7)$$

$$k_T = \frac{\gamma R_g \mu_l}{(\gamma - 1) Pr_l} \quad [\text{W m}^{-1} \text{K}^{-1}], \quad (3.8)$$

where Pr_l is the Prandtl number, considered constant in the present work and equal to $Pr_l = 0.726$, and $\gamma = C_p/C_v$. Equations (3.1) become the time-dependent inviscid Euler equations when $\mathbf{F}_v = 0$.

3.3 Detached Eddy Simulation

3.3.1 Governing equations

A Direct Numerical Simulation (DNS) is a computation where the whole range of spatial and temporal scales of turbulence is resolved, meaning that no turbulence model is required to close the Navier-Stokes equations. This translates into extremely refined meshes that can capture turbulent structures from the integral scale down to the Kolmogorov length scale where turbulent dissipation takes place. For external flows with high Reynolds numbers, such as the ones modelled in this work, the number of cells necessary for such computations would make their cost prohibitively high, despite the ever increasing power of High Performance Computing (HPC) facilities. The introduction of turbulence models can significantly reduce the time and resources needed to perform analyses on real life and complex flows and it is the way that most of the industrial flows are modelled at the present time. To introduce a turbulence model, each variable in Equation (3.1) is split into an averaged and a fluctuating component, namely $\bar{\mathbf{u}}$ and \mathbf{u}' , so that

$$\mathbf{u} = \bar{\mathbf{u}} + \mathbf{u}'. \quad (3.9)$$

Depending on the averaging process, two different approaches are obtained: Reynolds-Averaged Navier-Stokes (RANS) simulations and Large Eddy Simulation (LES). In RANS, the averaging process is performed in time, so that

$$\bar{\mathbf{u}}(\mathbf{x}) = \frac{1}{\Delta t} \int_t^{t+\Delta t} \mathbf{u}(\mathbf{x}, t) dt. \quad (3.10)$$

3. METHODOLOGY

RANS averaging of the N-S equations causes the generation of additional terms, called Reynolds stresses, which are new unknowns that are added to the equations. These unknowns pose a closure problem, *i.e.* the necessity to derive additional relations to close the problem and solve the equations. The RANS model adopted for this work defines two transport equations to formally close the flow governing equations.

In LES, the average is done in space, operating the convolution of the continuous variable $\mathbf{u}(\mathbf{y}, t)$ with a time-invariant filter kernel $\mathbf{G}(\mathbf{x}_i - \mathbf{y})$,

$$\bar{\mathbf{u}}(\mathbf{x}_i, t) = \int_{Vol} \mathbf{G}(\mathbf{x}_i - \mathbf{y}) \mathbf{u}(\mathbf{y}, t) d\mathbf{y}. \quad (3.11)$$

The filter kernel \mathbf{G} has an associated cut-off length scale Δ and turbulence scales smaller than the cut-off are eliminated from \mathbf{u} . It is quite common, in industrial applications, to match the filter kernel to the computational grid. As with the RANS approach, the LES filtering generates additional terms, called sub-grid scale stresses. These terms are analogous, *i.e.* they are derived in the same way, as the Reynolds stresses in RANS. A sub-grid scale (SGS) model is then introduced to represent the effects of the variable fluctuations \mathbf{u}' on the averaged field and close the problem. Several SGS models are available, among which the Yoshizawa [74] one-equation LES model that is used in this work which is built on the assumption of a match between the filter and the mesh. In this case, the filter \mathbf{G} is defined as a top-hat filter [75] given by

$$\mathbf{G}(\mathbf{x}_i - \mathbf{y}) = \frac{1}{\Delta_i} H\left(\frac{\Delta_i}{2} - |\mathbf{x}_i - \mathbf{y}|\right), \quad (3.12)$$

where Δ_i is the characteristic length of cell i , \mathbf{x}_i is the cell centre position, \mathbf{y} is the position vector and H is the heavy-side function. Yoshizawa's model assumes Δ_i to

3. METHODOLOGY

be the cubic root of the i^{th} cell volume V_i , $\Delta_i = \sqrt[3]{V_i}$.

The averaged Navier-Stokes equations obtained applying Equation (3.9) to Equation (3.1) are:

$$\frac{\partial \bar{\rho}}{\partial t} + \nabla \cdot (\bar{\rho} \bar{\mathbf{u}}) = 0, \quad (3.13)$$

$$\frac{\partial (\bar{\rho} \bar{\mathbf{u}})}{\partial t} + \nabla \cdot (\bar{\rho} \bar{\mathbf{u}} \otimes \bar{\mathbf{u}} + \bar{\rho} \mathbf{I} + \overline{\rho \mathbf{u}' \otimes \mathbf{u}'} - \bar{\boldsymbol{\tau}}) = 0, \quad (3.14)$$

$$\begin{aligned} \frac{\partial (\bar{\rho} \bar{e} + \frac{1}{2} \overline{\rho \mathbf{u}' \cdot \mathbf{u}'})}{\partial t} + \nabla \cdot \left(\bar{\rho} \bar{\mathbf{u}} \bar{h} + \frac{1}{2} \overline{\rho \bar{\mathbf{u}} \mathbf{u}' \cdot \mathbf{u}'} \right) = \\ \nabla \cdot [\bar{\mathbf{u}} \cdot (\bar{\boldsymbol{\tau}} - \overline{\rho \mathbf{u}' \otimes \mathbf{u}'}) - k_T \nabla \bar{T} - \overline{\rho \mathbf{u}' h'}], \end{aligned} \quad (3.15)$$

where the term $\frac{1}{2} \overline{\mathbf{u}' \cdot \mathbf{u}'}$ in Equation (3.15) represents the averaged turbulent kinetic energy \bar{k} , while the term $\overline{\rho \mathbf{u}' \otimes \mathbf{u}'}$ in Equations (3.14) and (3.15) is the Reynolds stress tensor, modelled by means of the Boussinesq approximation [76], in analogy to the viscous stress tensor, as

$$\bar{\mathbf{t}} = -\overline{\rho \mathbf{u}' \otimes \mathbf{u}'} = \mu_t \left(\nabla \bar{\mathbf{u}} + \bar{\mathbf{u}} \otimes \nabla - \frac{2}{3} \mathbf{I} \nabla \cdot \bar{\mathbf{u}} \right) - \frac{2}{3} \mathbf{I} \bar{\rho} \bar{k}. \quad (3.16)$$

In Equation (3.15), the term $\overline{\rho \mathbf{u}' h'}$ is the vector of turbulent transport of heat flux and it is modelled as proportional to the average temperature gradient [77] as

$$\bar{\mathbf{q}}_t = \overline{\rho \mathbf{u}' h'} = -\frac{\mu_t C_p}{Pr_t} \nabla \bar{T}, \quad (3.17)$$

where Pr_t is the turbulent Prandtl number, considered constant in this work and equal to $Pr_t = 0.91$. Equations (3.13) - (3.17) are invariant to whether time or space averaging is used. The equation system (3.13) - (3.15) has to be closed by

3. METHODOLOGY

means of an additional equation in order to couple the extra variable \bar{k} with the other averaged variables. The closure for \bar{k} is obtained by performing the scalar product of the vector of velocity fluctuations \mathbf{u}' with the Navier-Stokes equation of momentum conservation. The product is then averaged with Equation (3.11), giving the following transport equation for \bar{k} ,

$$\begin{aligned} \frac{\partial (\bar{\rho}\bar{k})}{\partial t} + \nabla \cdot \left(\bar{\rho}\bar{\mathbf{u}}\bar{k} - \overline{\mathbf{t} \cdot \mathbf{u}'} + \frac{1}{2} \overline{\rho \mathbf{u}' \mathbf{u}' \cdot \mathbf{u}'} + \overline{p' \mathbf{u}'} \right) = \\ - \overline{\rho \mathbf{u}' \cdot \mathbf{u}'} \nabla \cdot \bar{\mathbf{u}} - \overline{\mathbf{t} : \mathbf{u}' \otimes \nabla} - \overline{\mathbf{u}' \cdot \nabla p'} + \overline{p' \nabla \cdot \mathbf{u}'}, \end{aligned} \quad (3.18)$$

where $:$ is the double scalar product. Unfortunately, Equation (3.18) introduces new unknowns in the problem that would require new equations to be defined. To solve this issue, some modelling is necessary and Equation (3.18) has to be expressed in a different way. For the RANS approach, two mainstream closure models are based on a two-equation closure system that defines a new transport equation for \bar{k} and an additional transport equation. The additional equation is commonly based either on the average dissipation rate per unit mass $\bar{\epsilon}$ or on the average specific turbulence dissipation rate $\bar{\omega}$, giving the $k - \epsilon$ or $k - \omega$ model respectively. For the $k - \epsilon$ model, the viscous dissipation of turbulent shear stress is proportional to $\bar{\epsilon}$ as

$$\overline{\mathbf{t} : \mathbf{u}' \otimes \nabla} = \bar{\rho}\bar{\epsilon} = \mu_t \overline{\nabla \mathbf{u}' : \nabla \mathbf{u}'}. \quad (3.19)$$

For the $k - \omega$ model, the same term can be expressed as function of $\bar{\omega}$,

$$\overline{\mathbf{t} : \mathbf{u}' \otimes \nabla} = \beta^* \bar{\rho} \bar{k} \bar{\omega}. \quad (3.20)$$

3. METHODOLOGY

The two approaches have different properties and limitations. The shear stress transport (SST) model adopted in this work has been developed by Menter [78] by combining the strengths of both $k - \epsilon$ and $k - \omega$ models while limiting their drawbacks. The SST model behaves like the $k - \omega$ model in the inner parts of the boundary layer. This makes the model well-posed all the way down to the wall without the introduction of extra damping functions. The model then mimics a $k - \epsilon$ treatment in free-stream flows where it performs better than its counterpart, especially in the presence of adverse pressure gradients and in separating flows. The two-equation closure of the $k - \omega$ -SST model is then given by

$$\frac{D(\bar{\rho}\bar{k}_{RANS})}{Dt} = \bar{\mathbf{t}} : \bar{\mathbf{u}} \otimes \nabla - \beta^* \bar{\rho}\bar{k}_{RANS}\bar{\omega} + \nabla \cdot [(\mu_l + \sigma_k \mu_{t,RANS}) \nabla \bar{k}_{RANS}], \quad (3.21)$$

and

$$\begin{aligned} \frac{D(\bar{\rho}\bar{\omega})}{Dt} = \gamma \bar{\rho}\bar{\mathbf{t}} : \bar{\mathbf{u}} \otimes \nabla - \beta^* \bar{\rho}\bar{\omega}^2 + \nabla \cdot [(\mu_l + \sigma_\omega \mu_{t,RANS}) \nabla \bar{\omega}] + \\ (1 - F_1) 2\bar{\rho}\sigma_\omega \frac{1}{\bar{\omega}} \nabla \bar{k}_{RANS} \cdot \nabla \bar{\omega}, \end{aligned} \quad (3.22)$$

where D/Dt represents the material operator $D/Dt = \partial/\partial t + \bar{\mathbf{u}} \cdot \nabla$ and $\bar{\mathbf{t}}$ is the turbulent stress tensor, given by

$$\bar{\mathbf{t}} = \mu_{t,RANS} \left(\nabla \bar{\mathbf{u}} + \bar{\mathbf{u}} \otimes \nabla - \frac{2}{3} \mathbf{I} \nabla \cdot \bar{\mathbf{u}} \right) - \frac{2}{3} \bar{\rho}\bar{k}_{RANS} \mathbf{I}. \quad (3.23)$$

Equation (3.22) works both as ϵ equation and ω equation depending on the value of

3. METHODOLOGY

	σ_k	σ_ω	β	β^*	γ
$k - \omega$	0.85	0.5	0.075	0.09	$\frac{\beta_1}{\beta^*} - \frac{\sigma_{\omega 1} \kappa^2}{\sqrt{\beta^*}}$
$k - \epsilon$	1.0	0.856	0.0828	0.09	$\frac{\beta_2}{\beta^*} - \frac{\sigma_{\omega 2} \kappa^2}{\sqrt{\beta^*}}$

Table 3.1: Turbulence closure model coefficients.

the blending function F_1 that is used to couple the constants of the two models:

$$\begin{pmatrix} \sigma_k \\ \sigma_\omega \\ \beta \\ \gamma \end{pmatrix} = F_1 \begin{pmatrix} \sigma_{k1} \\ \sigma_{\omega 1} \\ \beta_1 \\ \gamma_1 \end{pmatrix} + (1 - F_1) \begin{pmatrix} \sigma_{k2} \\ \sigma_{\omega 2} \\ \beta_2 \\ \gamma_2 \end{pmatrix}. \quad (3.24)$$

The constants are reported in Table 3.1, where $\kappa = 0.41$ is the Von Kármán constant and the compound subscript 1 refers to the $k - \omega$ model while the subscript 2 refers to the $k - \epsilon$ model. The blending function F_1 is

$$F_1 = \tanh \left\{ \min \left[\max \left(2 \frac{\sqrt{\bar{k}_{RANS}}}{0.09 \bar{\omega} y}, \frac{500 \mu_l}{\bar{\rho} \bar{\omega} y^2} \right), \frac{4 \bar{\rho} \sigma_{\omega 2} \bar{k}_{RANS}}{CD_{k\omega} y^2} \right] \right\}^4, \quad (3.25)$$

where $CD_{k\omega}$ is

$$CD_{k\omega} = \max \left(2 \bar{\rho} \sigma_{\omega 2} \frac{1}{\bar{\omega}} \nabla \bar{k}_{RANS} \cdot \nabla \bar{\omega}, 10^{-20} \right) \quad (3.26)$$

and y is the distance from the closest wall to the centre of the cell.

The eddy viscosity $\mu_{t,RANS}$ is given by

$$\mu_{t,RANS} = \frac{\bar{\rho} \alpha_1 \bar{k}_{RANS}}{\max(\alpha_1 \bar{\omega}, |\mathbf{S}_{ij}| F_2)}, \quad (3.27)$$

where $\alpha_1 = 0.31$, $|\mathbf{S}_{ij}|$ is the magnitude of the strain rate tensor $\mathbf{S}_{ij} = 1/2 (\nabla \bar{\mathbf{u}} + \bar{\mathbf{u}} \otimes \nabla)$

3. METHODOLOGY

and the function F_2 is defined as

$$F_2 = \tanh \left[\max \left(2 \frac{\sqrt{\bar{k}_{RANS}}}{0.09\bar{\omega}y}, \frac{400\mu_l}{\bar{\rho}\bar{\omega}y^2} \right) \right]. \quad (3.28)$$

The closure problem in LES can be tackled in a similar way as in RANS by defining an alternative to Equation (3.18) for \bar{k} . Such approach is followed by Yoshizawa's [74] one-equation model, that defines the transport equation as

$$\frac{D(\bar{\rho}\bar{k}_{LES})}{Dt} = \bar{\mathbf{t}} : \bar{\mathbf{u}} \otimes \nabla - C_d \frac{\bar{\rho}\bar{k}_{LES}^{3/2}}{\Delta} + \nabla \cdot [(\mu_l + \sigma_k \mu_{t,LES}) \nabla \bar{k}_{LES}], \quad (3.29)$$

where $\bar{\mathbf{t}}$ is given by Equation (3.23) substituting \bar{k}_{RANS} with \bar{k}_{LES} and the eddy viscosity $\mu_{t,LES}$ is given by

$$\mu_{t,LES} = \bar{\rho} C_s \Delta \sqrt{\bar{k}_{SGS}}. \quad (3.30)$$

In Equations (3.29) and (3.30), the parameters C_s and C_d are the Yoshizawa constants and are related to the Smagorinsky constant by

$$C_{smag} = \left(\frac{C_s^3}{C_d} \right)^{0.25}. \quad (3.31)$$

The Smagorinsky constant typically ranges from 0.065 to 0.2 and for the purpose of this work $C_{smag} = 0.1$ will be assumed. The resulting Yoshizawa constants for the model are $C_s = 0.046$, $C_d = 1.0$, and $\sigma_k = 1.0$. The low value assumed for the Smagorinsky constant C_{smag} in this work was chosen to prevent over-damping and to reduce the re-laminarisation of the flow leaving the nozzle boundary layer.

The Detached-Eddy Simulation (DES) approach was developed as an hybrid

3. METHODOLOGY

approach to merge LES and RANS. DES is a three-dimensional unsteady numerical solution obtained using a single turbulence model, which functions as an SGS model in regions where the grid density is fine enough for LES, and as a RANS model in regions where it is not. The reason behind the development of the DES approach is the attempt to reduce the mesh points required for accurately solve the flow close to the wall in three-dimensional simulations. A wall-resolved LES can be prohibitively expensive to perform due to the mesh clustering in the boundary layer region, since, as stated by Piomelli [79], ‘over 90% of the grid points are needed to resolve less than 10% of the computational domain’. To overcome this difficulty, the RANS approach is used close to the wall where it is known to provide accurate mean boundary layer predictions.

By inspection of Equations (3.21) and (3.29) it is shown that the LES and RANS models can be easily blended together resulting in the following \bar{k} transport equation,

$$\frac{D(\bar{\rho}\bar{k})}{Dt} = \bar{\mathbf{t}} : \bar{\mathbf{u}} \otimes \nabla - \left[\Gamma \beta^* \bar{\rho} \bar{k} \bar{\omega} + (1 - \Gamma) C_d \frac{\bar{\rho} \bar{k}^{3/2}}{\Delta} \right] + \nabla \cdot [(\mu_l + \sigma_k \mu_t) \nabla \bar{k}], \quad (3.32)$$

where the eddy viscosity μ_t is obtained by blending Equations (3.27) and (3.30) as follows,

$$\mu_t = \Gamma \mu_{t,RANS} + (1 - \Gamma) \mu_{t,LES}. \quad (3.33)$$

The blending function Γ is defined as

$$\Gamma = \tanh \left[\max \left(\frac{\sqrt{\bar{k}_{RANS}}}{0.09 \bar{\omega} y}, \frac{500 \mu_l}{\bar{\rho} \bar{\omega} y^2} \right) \right]^4. \quad (3.34)$$

Depending on the value of Γ , there are three possible regions in the flow: the RANS region, where $\Gamma \rightarrow 1$ and the closure is given by Equations (3.21) and (3.22) and

3. METHODOLOGY

$\bar{k} \equiv \bar{k}_{RANS}$, the LES region where $\Gamma \rightarrow 0$ and Equation (3.29) is recovered leading to $\bar{k} \equiv \bar{k}_{LES}$, and an intermediate region where the two models work together to solve Equation (3.32). The $\bar{\omega}$ transport equation (3.22) is solved everywhere in the domain to guarantee continuity in the transport of $\bar{\omega}$, however, its result is not used in the LES region.

Equations (3.13), (3.14), (3.15) and (3.32) can be rearranged in a compact form:

$$\frac{\partial}{\partial t} \mathbf{U} + \nabla \cdot (\mathbf{F}_c + \mathbf{F}_v) + \mathbf{S} = 0, \quad (3.35)$$

where the conservative variable vector \mathbf{U} , the convective flux vector \mathbf{F}_c , the turbulent flux vector \mathbf{F}_v and the turbulent source term vector \mathbf{S}_t are given by:

$$\mathbf{U} = \begin{pmatrix} \bar{\rho} \\ \bar{\rho} \bar{\mathbf{u}} \\ \bar{\rho} (\bar{e} + \bar{k}) \\ \bar{\rho} \bar{k} \\ \bar{\rho} \bar{\omega} \end{pmatrix}, \quad (3.36)$$

$$\mathbf{F}_c = \begin{pmatrix} \bar{\rho} \bar{\mathbf{u}} \\ \bar{\rho} \bar{\mathbf{u}} \otimes \bar{\mathbf{u}} + \bar{p} \mathbf{I} \\ \bar{\rho} \bar{\mathbf{u}} (\bar{\rho} \bar{e} + \bar{p} / \bar{\rho} + \bar{k}) \\ \bar{\rho} \bar{\mathbf{u}} \bar{k} \\ \bar{\rho} \bar{\mathbf{u}} \bar{\omega} \end{pmatrix}, \quad (3.37)$$

3. METHODOLOGY

$$\mathbf{F}_v = \begin{pmatrix} 0 \\ -(\bar{\mathbf{t}} + \bar{\boldsymbol{\tau}}) \\ -\bar{\mathbf{q}} - \bar{\mathbf{q}}_t - (\bar{\mathbf{t}} + \bar{\boldsymbol{\tau}}) \cdot \bar{\mathbf{u}} - (\mu_l + \sigma_k \mu_t) \nabla \bar{k} \\ -(\mu_l + \sigma_k \mu_t) \nabla \bar{k} \\ -(\mu_l + \sigma_\omega \mu_t) \nabla \bar{\omega} \end{pmatrix}, \quad (3.38)$$

$$\mathbf{S}_t = \begin{pmatrix} 0 \\ 0 \\ 0 \\ \Gamma \beta^* \bar{\rho} \bar{k} \bar{\omega} + (1 - \Gamma) C_d \bar{\rho} \bar{k}^{3/2} / \Delta - \bar{\mathbf{t}} : \nabla \bar{\mathbf{u}} \\ \beta \bar{\rho} \bar{\omega}^2 + 2(1 - F_1) (\bar{\rho} \sigma_{\omega 2} \nabla \bar{k}_{RANS} \cdot \nabla \bar{\omega}) / \bar{\omega} - \gamma \bar{\rho} \bar{\mathbf{t}} : \bar{\mathbf{u}} \otimes \nabla \end{pmatrix}. \quad (3.39)$$

3.3.2 Finite-volume spatial discretisation

The finite-volume discretisation is a method that allows to represent partial differential equations in the form of algebraic equations [80]. In the structured finite volume discretisation, the physical domain is mapped by a cluster of topologically hexahedral control volumes V_i , where the subscript i refers to the i^{th} control volume of the mesh. Equation (3.35) is integrated over each control volume, giving

$$\int_{V_i} \frac{\partial \mathbf{U}}{\partial t} dV + \int_{V_i} \nabla \cdot (\mathbf{F}_c + \mathbf{F}_v) dV + \int_{V_i} \mathbf{S}_t dV = 0. \quad (3.40)$$

3. METHODOLOGY

If a stationary computational domain is considered, by applying the Gauss divergence theorem to Equation (3.40), this can be written as

$$\frac{\partial}{\partial t} \int_{V_i} \mathbf{U} dV + \oint_{S_i} \mathbf{F}_c \cdot \mathbf{n} dS + \oint_{S_i} \mathbf{F}_v \cdot \mathbf{n} dS + \int_{V_i} \mathbf{S}_t dV = 0, \quad (3.41)$$

where S_i is the closed boundary of V_i and \mathbf{n} its outwards normal unit vector. The integration of the convective and turbulent flux vectors can be expressed as the summation of the contributions from all discrete faces delimiting the control volume V_i . It is then possible to write:

$$\mathbf{U}_i = \frac{1}{V_i} \int_{V_i} \mathbf{U} dV, \quad (3.42)$$

$$\oint_{S_i} \mathbf{F}_c \cdot \mathbf{n} dS = \sum_{k=1}^{N_{faces}} \mathbf{F}_{c_k} \cdot \mathbf{n}_{i,k} S_{i,k}, \quad (3.43)$$

$$\oint_{S_i} \mathbf{F}_v \cdot \mathbf{n} dS = \sum_{k=1}^{N_{faces}} \mathbf{F}_{v_k} \cdot \mathbf{n}_{i,k} S_{i,k}, \quad (3.44)$$

$$\mathbf{S}_{t_i} = \frac{1}{V_i} \int_{V_i} \mathbf{S}_t dV, \quad (3.45)$$

where N_{faces} is the number of faces of the control volume V_i , $S_{i,k}$ is the k^{th} face of V_i , and $\mathbf{n}_{i,k}$ its outwards normal unit vector. Equation (3.41) can then be rewritten in compact form as

$$V_i \frac{\partial \mathbf{U}_i}{\partial t} + \mathcal{R}_i = 0, \quad (3.46)$$

where \mathbf{U}_i is the space-averaged value of the vector of conservative variables over the cell volume V_i and \mathcal{R}_i is the residual generated from the discretised terms and it is equal to

$$\mathcal{R}_i = \sum_{k=1}^{N_{faces}} \mathbf{F}_{c_k} \cdot \mathbf{n}_{i,k} S_{i,k} + \sum_{k=1}^{N_{faces}} \mathbf{F}_{v_k} \cdot \mathbf{n}_{i,k} S_{i,k} + V_i \mathbf{S}_{t_i}. \quad (3.47)$$

3. METHODOLOGY

To solve the non-linear equation system (3.46), the residual operator \mathcal{R}_i needs to be computed in all its parts.

The convective flux vector \mathbf{F}_c is linearised by means of the Godunov method, or Flux Difference Splitting. Interface fluxes normal to the finite-volume cell boundaries are evaluated with an approximate Riemann solver developed by Roe [81]. Roe's approximate Riemann solver is based on a piecewise constant reconstruction of the state in each cell and it is then first-order accurate in space [82]. To mitigate the excessive artificial dissipation introduced by the first order method, Van Leer *et al.* [83] replaced the piecewise constant approach with a quadratic reconstruction, obtaining a higher order spatial reconstruction, the so-called Monotone Upwind Scheme for Conservation Laws (MUSCL) interpolation. In the present work, the coefficients of the reconstruction are imposed as described by Manna [84] to give a third-order accurate reconstruction of the spatial gradients in regions of the flow that do not present strong variations. To define the values on the two sides of a given interface, the reconstruction procedure uses four contiguous cells. In order to obtain a stable numerical scheme, a limiter is introduced for this process. Sweby [85] demonstrated that a numerically stable scheme is achieved if the total variation (TV) of the conservative variables does not increase at each iteration. The total variation of conservative variables for the discrete case is expressed as

$$TV(\mathbf{U}^n) = \sum_i |\mathbf{U}_{i+1}^n - \mathbf{U}_i^n|. \quad (3.48)$$

The condition to achieve a stable scheme then translates into

$$TV(\mathbf{U}^{n+1}) \leq TV(\mathbf{U}^n). \quad (3.49)$$

3. METHODOLOGY

A scheme respecting the condition of Equation (3.49) is defined as Total Variation Diminishing (TVD) and it is monotonic and stable. A limiting function is then defined that satisfies the following conditions [85]:

$$\phi(r) = 0 \quad \forall \quad r \leq 0, \quad (3.50)$$

$$r \leq \phi(r) \leq \min[1, 2r] \quad \forall \quad 0 < r \leq 1, \quad (3.51)$$

$$1 \leq \phi(r) \leq \min[2, r] \quad \forall \quad r > 1, \quad (3.52)$$

where r is the ratio of consecutive gradients, a measure of the smoothness of the solution, and for a given cell is defined as

$$r_i = \frac{u_i - u_{i-1}}{u_{i+1} - u_i}. \quad (3.53)$$

The limiting function $\phi(r)$ must be designed in such a way to satisfy Equations (3.50) – (3.52), describing a certain region in the $\phi(r) - r$ plane known as the TVD region for second-order TVD schemes, which is represented by the shaded regions in Fig. 3.1. A number of limiters are available, each with different behaviour and properties, so that it is not possible to define a universal best limiter, but a most suitable approach for a given problem. For the present study, the van Leer [86] limiter is used,

$$\phi_{vl}(r) = \frac{r + |r|}{1 + |r|}. \quad (3.54)$$

This limiter possesses the symmetry property

$$\frac{\phi_{vl}(r)}{r} = \phi_{vl}\left(\frac{1}{r}\right), \quad (3.55)$$

3. METHODOLOGY

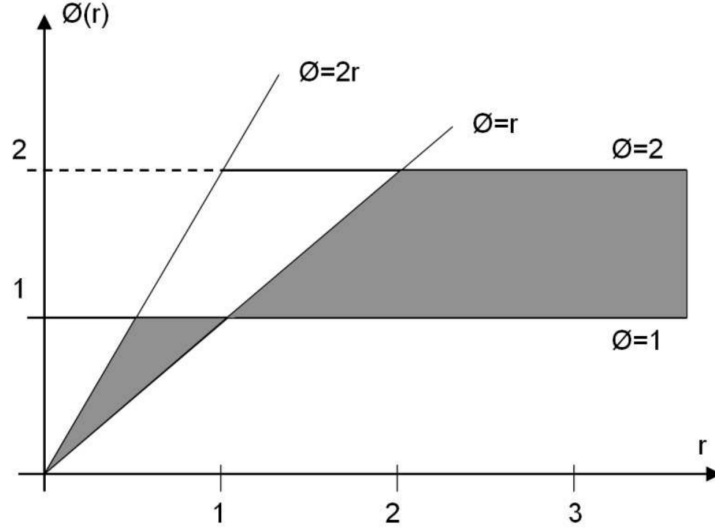


Figure 3.1: Region of stable operation of a second-order TVD scheme, from Sweby [85].

which ensures that the limiting action on forward and backward gradients is the same.

The viscous fluxes \mathbf{F}_v from Equation (3.47) are estimated by means of the velocity vector gradients. For their computation, a staggered grid is built across the cell interfaces where the gradients are evaluated. The flow state at the surface boundary of the newly created control volume and the surface normal unit vector are computed from the mesh geometry and the velocity gradient is then obtained using the Gauss divergence theorem. This approach produces an accurate reconstruction of the velocity gradients up to the second-order [84].

Lastly, the source term vector \mathbf{S}_{t_i} includes the production and destruction terms of the $k-\omega$ -SST equations. The production term is evaluated using Equation (3.23) to calculate the Reynolds stress tensor $\boldsymbol{\tau}$ and by applying the Gauss divergence theorem to calculate the velocity gradients. The evaluation of the source term S_{t_i}

3. METHODOLOGY

completes the estimation of the linear terms in Equation (3.47) and the final step to evaluate the solution of the volume-averaged vector of conservative variables \mathbf{U} is then the time integration of the differential $\partial\mathbf{U}_i/\partial t$.

3.3.3 Time integration

To integrate the discrete ordinary differential vector Equation (3.46), an explicit multi-stage Runge-Kutta time step integration algorithm is used. The scheme is computationally cheap, both in terms of computational power and memory allocation, and it is designed to preserve the TVD properties of the spatial differentiation scheme. The algorithm is implemented as follows:

$$\begin{aligned} \mathbf{U}_i^0 &= \mathbf{U}_i^n \\ \text{do } k &= 1, m \\ \mathbf{U}_i^k &= \mathbf{U}_i^0 - \alpha_k \frac{\Delta t}{V_i} \mathcal{R}^{k-1} \\ \text{end do} \\ \mathbf{U}_i^{n+1} &= \mathbf{U}_i^m \end{aligned} \tag{3.56}$$

where m denotes the number of stages of the Runge-Kutta scheme and n the time level. The stability of the scheme is restricted by the Courant-Friedrichs-Lewy condition [87]:

$$\Delta t \leq CFL \frac{V_i}{l_x + l_y + l_z}, \tag{3.57}$$

3. METHODOLOGY

$$\begin{aligned}\ell_x &= (|u_i| + c_i) S_i^x, \\ \ell_y &= (|v_i| + c_i) S_i^y, \\ \ell_z &= (|w_i| + c_i) S_i^z,\end{aligned}\tag{3.58}$$

where CFL is the Courant number, V_i is the cell volume, c_i is the local speed of sound, and S_i^x , S_i^y , and S_i^z are the projected areas of cell i in the x , y , and z directions. As the target simulation is a high Reynolds number jet, which is dominated by convection, the inviscid form of the CFL condition of Equations (3.57) - (3.58) was found to provide numerically stable computations.

3.3.4 Boundary conditions

Boundary conditions have a crucial role in any CFD simulation and in particular for CAA simulations. It is of fundamental importance that no spurious perturbations are created at the boundaries and that outward travelling waves and disturbances from the domain are not reflected back into the flow-field. The imposed boundary conditions are defined using a one-cell deep exterior frame surrounding the physical domain. The boundary condition values depend on the first interior cell variables and on the imposed conditions on the exterior ghost cells. This function is defined according to the physical boundary condition that is necessary to impose on a given boundary. A number of different conditions is needed for the simulation of a free jet. The boundary conditions adopted in the present work are: non-reflecting far-field, subsonic inflow, subsonic outflow, and no-slip wall.

3. METHODOLOGY

3.3.4.1 Non-reflecting far-field

The far-field condition switches between a subsonic inflow and a subsonic outflow condition depending on the value of the inner flow velocity component normal to the surface boundary. The definition of accurate Non-Reflective Boundary Conditions (NRBC) is crucial in CAA applications [88]. To define the conditions for the 3D case, an extension of the characteristic based boundary conditions from Giles [89] as found in Givoli [90] is used. Depending on whether the flow is entering or exiting the computational domain, the following procedure is adopted to limit the non-physical reflections caused by the numerical scheme. The flow parameters at the far-field have to satisfy a reference free stream condition:

$$\begin{pmatrix} p \\ T \\ \mathbf{u} \end{pmatrix} = \begin{pmatrix} p_\infty \\ T_\infty \\ \mathbf{u}_\infty \end{pmatrix}. \quad (3.59)$$

Consider the one-dimensional flow in the direction of the boundary outward unit normal \mathbf{n} . The incoming Riemann invariant R^- is defined from the free-stream conditions as

$$R^- = \mathbf{u}_\infty \cdot \mathbf{n} - \frac{2c_\infty}{\gamma - 1}, \quad (3.60)$$

where c_∞ is the free stream speed of sound. On the other hand, the outgoing Riemann invariant R^+ is defined from the first interior cell towards the surface of the computational domain boundary as

$$R^+ = \mathbf{u}_{phy} \cdot \mathbf{n} - \frac{2c_{phy}}{\gamma - 1}, \quad (3.61)$$

3. METHODOLOGY

where c_{phy} is the speed of sound at the computational domain interior. The speed of sound (c_S) and the normal velocity component ($\mathbf{u}_S \cdot \mathbf{n}$) of the incoming wave at the boundary interface are defined as

$$c_S = \frac{\gamma - 1}{4} (R^+ - R^-) \quad (3.62)$$

and

$$\mathbf{u}_S \cdot \mathbf{n} = \frac{R^+ - R^-}{2} . \quad (3.63)$$

The sign of the surface normal velocity component $\mathbf{u}_S \cdot \mathbf{n}$ can be either positive or negative. This determines whether the condition to be applied locally is an inflow or outflow boundary condition. The outflow condition, used where $\mathbf{u}_S \cdot \mathbf{n} > 0$, is:

$$\mathbf{u}_b = [\mathbf{u}_{phy} - (\mathbf{u}_{phy} \cdot \mathbf{n}) \mathbf{n}] + (\mathbf{u}_s \cdot \mathbf{n}) \mathbf{n} , \quad (3.64)$$

$$\rho_b = \left(\frac{\rho_{phy}^\gamma c_S^2}{\gamma p_{phy}} \right)^{\frac{1}{\gamma-1}} , \quad (3.65)$$

$$p_b = \frac{\rho_b c_S^2}{\gamma} . \quad (3.66)$$

The inflow condition, used where $\mathbf{u}_S \cdot \mathbf{n} \leq 0$, is instead:

$$\mathbf{u}_b = [\mathbf{u}_\infty - (\mathbf{u}_\infty \cdot \mathbf{n}) \mathbf{n}] + (\mathbf{u}_s \cdot \mathbf{n}) \mathbf{n} , \quad (3.67)$$

$$\rho_b = \left(\frac{\rho_\infty^\gamma c_S^2}{\gamma p_\infty} \right)^{\frac{1}{\gamma-1}} , \quad (3.68)$$

$$p_b = \frac{\rho_b c_S^2}{\gamma} . \quad (3.69)$$

3. METHODOLOGY

The vector of conservative variables imposed at the ghost cell is then:

$$\mathbf{U}_b = \begin{pmatrix} \rho_b \\ \rho_b \mathbf{u}_b \\ \frac{1}{\gamma-1} \rho_b + \frac{1}{2} \rho_b \mathbf{u}_b \cdot \mathbf{u}_b \end{pmatrix}. \quad (3.70)$$

3.3.4.2 Subsonic inflow

An inflow boundary condition can either be subsonic or supersonic depending on the inlet Mach number normal to the boundary surface. In the present work, only subsonic inlet conditions are imposed for the simulation. The inflow condition is formulated following the same characteristic based approach as for the far-field boundary condition for a three-dimensional flow. For a subsonic flow, four characteristic waves (λ_2 to λ_5) move towards the domain interior. It is therefore necessary and sufficient to impose four quantities for the subsonic inflow condition. It is common practice to impose the stagnation temperature T_0 , the stagnation pressure p_0 , and two inlet flow angles α , the polar angle, and β , the azimuthal angle. The imposed conditions are used in conjunction with the interior flow variables as presented hereafter. The negative Riemann invariant is evaluated as in Equation 3.60 but with the interior quantities

$$R^- = \mathbf{u} \cdot \mathbf{n} - \frac{2c}{\gamma - 1}. \quad (3.71)$$

The interior tangential velocity component is then evaluated as

$$u_t = |\mathbf{u} - \mathbf{u} \cdot \mathbf{n}|. \quad (3.72)$$

3. METHODOLOGY

The entropy and total enthalpy values at the inlet, based on the imposed conditions, are:

$$s = \frac{p_0}{(\rho)^\gamma}, \quad h_0 = \frac{\gamma R_g T_0}{\gamma - 1}. \quad (3.73)$$

The positive Riemann invariant is defined as

$$R^+ = \frac{1}{\gamma} \left[(\gamma - 3) R^- + 4 \sqrt{h_0 - \frac{u_t^2}{2} - \frac{\gamma - 1}{2} (R^-)^2} \right]. \quad (3.74)$$

At this point, the normal velocity and the speed of sound at the boundary can be calculated using the Riemann invariants as:

$$u_{nb} = \frac{R^+ + R^-}{2}, \quad c_b = \frac{\gamma - 1}{4} (R^+ - R^-). \quad (3.75)$$

The boundary velocity is then given by

$$u_b = \sqrt{u_{nb}^2 + u_t^2}. \quad (3.76)$$

The velocity components at the boundary can be now obtained by decomposing the velocity u_b according to the two prescribed velocity angles α and β :

$$\begin{aligned} u_b &= u_b \cos(\alpha), \\ v_b &= u_b \sin(\alpha) \cos(\beta), \\ w_b &= u_b \sin(\alpha) \sin(\beta). \end{aligned} \quad (3.77)$$

3. METHODOLOGY

Finally, density, static pressure, and temperature at the boundary are imposed as follows:

$$\rho_b = \left(\frac{c^2}{\gamma s} \right)^{\frac{1}{\gamma-1}}, \quad (3.78)$$

$$p_b = \frac{\rho_b c^2}{\gamma}, \quad (3.79)$$

$$T_b = T_0 \left(\frac{p_b}{p_0} \right)^{\frac{\gamma-1}{\gamma}}. \quad (3.80)$$

3.3.4.3 Subsonic outflow

In the subsonic outflow condition, only one characteristic wave is moving towards the domain interior (λ_1), therefore only one quantity needs to be assigned. The static pressure p_b is imposed at the exit and the other primitive variables are extrapolated from the interior domain. The back pressure equation, as function of the normal Mach number component, is obtained from Manna [84],

$$c_1 M_{nb}^3 + c_2 M_{nb}^2 + c_3 M_{nb} + c_4 = 0, \quad (3.81)$$

where M_{nb} is the normal component of the boundary condition Mach number that is obtained by solving Equation 3.81 using a Newton-Raphson method, and the

3. METHODOLOGY

coefficients c_1 , c_2 , c_3 , and c_4 are:

$$c_1 = \gamma - 1 , \quad (3.82)$$

$$c_2 = 2\gamma , \quad (3.83)$$

$$c_3 = \gamma - 3 , \quad (3.84)$$

$$c_4 = 2 - \left[\left(\rho c (1 + M_n)^2 \left(\frac{\gamma - 1}{\gamma} V_n + \frac{2c}{\gamma} \right) \right) \right] / p_b \gamma - 1 , \quad (3.85)$$

where V_n is the velocity component normal to the boundary. The speed of sound at the boundary is evaluated as

$$c_b = \frac{\gamma p_b (M_{nb} + 1)^2}{\rho c (M_n + 1)^2} . \quad (3.86)$$

Then, the boundary primitive variables are determined as follows:

$$\rho_b = \frac{\gamma p_b}{c_b^2} , \quad (3.87)$$

$$u_{nb} = M_{nb} c_b , \quad (3.88)$$

$$\mathbf{u}_b = (\mathbf{u} - (\mathbf{u} \cdot \mathbf{n}) \mathbf{n}) + u_{nb} \mathbf{n} . \quad (3.89)$$

3.3.4.4 No-slip wall

For viscous flows, the fluid in contact with a solid wall interface has a zero relative velocity. For a stationary surface, the boundary velocity vector is defined as $\mathbf{u}_b = -\mathbf{u}$ to impose a zero velocity value at the solid interface. By imposing a zero pressure gradient normal to the wall and no heat flux through the wall (adiabatic solid wall), the pressure and temperature can be set equal to the interior variables, $p_b = p$ and $T_b = T$.

3. METHODOLOGY

3.3.5 Sponge region treatment

In simulations of supersonic jets, the pressure waves travelling in the computational domain have a large amplitude and the implementation of the above mentioned boundary conditions might not be sufficient if the dimensions of the domain are too small. In order to limit the computational cost of the simulations, the numerical domain is not large enough to guarantee that the incident waves will not reflect back into the domain. For this reason, a sponge region is introduced that surrounds the whole physical domain. The sponge region uses a high stretching factor of the mesh, resulting in a rapid growth of cell size away from the physical boundaries of the computation. The goal of this design is to damp travelling waves in order to reduce their intensity to levels that can be safely handled by the boundary conditions. To improve the sponge region performance, two non-exclusive approaches are implemented in the solver to increase the damping capability of this region. The two approaches, described by Fosso [91], are:

- use of a second order filter

$$\hat{u}_{i,j,k} = u_{i,j,k} - \sigma_f \left(\frac{x_e - x}{x_e - x_s} \right)^p \left(\frac{1}{4}u_{i-1,j,k} - \frac{1}{2}u_{i,j,k} + \frac{1}{4}u_{i+1,j,k} \right), \quad (3.90)$$

where u is the field to be filtered, σ_f is the filtering parameter, and x_s and x_e are the starting and ending coordinates of the sponge region respectively. The function $(x_e - x)^p / (x_e - x_s)^p$ allows to apply the filter in a progressive way. The exponent p is taken equal to 2.

- addition of a source term to drive the vector of conservative variables towards

3. METHODOLOGY

a target ambient flow state

$$\frac{\partial U}{\partial t} + \dots = \sigma_r \frac{c}{\Delta x} \left(\frac{x_e - x}{x_e - x_s} \right)^p (u - U_{tar}) , \quad (3.91)$$

where U_{tar} is the target state, σ_r is the recall parameter, c is the speed of sound, and Δx is the dimension of the cell in the buffer zone to which Equation (3.91) is applied. As for the filter equation, the exponent is $p = 2$.

The use of these treatments, applied together in the present work, was found to be sufficient to reduce the amplitude of the reflected waves for the purpose of the simulation.

Details on the implementation of all boundary conditions can be found in El-Dosoky [92].

3.4 MPI approach

The flow solver uses Message Passing Interface (MPI) to split its execution on multiple threads on High Performance Computing clusters. The numerical model is parallelised by domain decomposition. The numerical mesh is split into blocks that are then assigned to individual cores of multi-core processors. The GreedyXtra load-balancing algorithm described by Ytterström [93] is adopted for this scope in this work. The GreedyXtra is an iterative algorithm that considers the extra work performed due to the ghost cell treatment and for the handling of blocks. The number of float operations performed for the ghost cells is taken proportional to the number of float operations for the interior cells and it is possible to assign different param-

3. METHODOLOGY

eters for different directions (i, j, k) . The performance model for the algorithm is defined as

$$t_j = \frac{1}{P_j} \sum_{k \in G_j} [(N_k + Ng_k) \times W] , \quad (3.92)$$

where t_j is the processing time for the current core j , P_j is the number of float operations per second for core j , G_j is the set of blocks allocated to core j , N_k is the number of internal grid-cells for block k , Ng_k is the number of ghost cells for block k evaluated from the parameters defined by the user, and W is the work performed for each cell, *i.e.* the number of floats operations. The optimum uni-core time can be defined as

$$T_{uni} = \frac{\sum_k [(N_k + Ng_k) \times W]}{\sum_j P_j} . \quad (3.93)$$

The optimum time is updated after each split because the number of ghost cells increases every time a block is split.

This algorithm allows for an efficient splitting of the mesh on a given number of processors that translates into a well-balanced repartition of workload. The flow solver is then able to efficiently perform simulations with more than 1,800 processors, allowing the use of large meshes with more than 200 million cells.

3.5 Validation

The implementation and validation of the described schemes for the flow solver has been performed by El-Dosoki [92] as part of his PhD work. The flow solver has been successfully used for several PhD theses [92, 94, 95], journal articles [96, 97], and conference articles [98, 99] and shows a solid track record of successful studies. However, the in-house code had never been used to perform CAA analysis

3. METHODOLOGY

of supersonic free jets. The single jet test case presented in the following chapter has been used as a benchmark test to validate the solver capabilities to reliably perform this kind of simulations.

Chapter 4

Supersonic under-expanded single jet

The single jet test case presented in this chapter models a single jet experiment by André [4]. Experimental data from André [4] are available for comparison as well as numerical data provided by the Centre Européen de Recherche et de Formation Avancée en Calcul Scientifique (CERFACS) [100]. CERFACS modelled the same jet using the *elsA* solver, developed by ONERA, which is a finite-volume multi-block structured solver with the 6-th order implicit compact finite difference scheme by Lele [101] that was extended to finite-volumes by Fosso *et al.* [102]. The scheme is stabilized by the compact filter of Visbal & Gaitonde [103] that is also used as an implicit subgrid-scale model for obtaining LES. Time integration is performed by a six-step third-order Runge-Kutta Dispersion Relation Preserving (DRP) scheme by Bogey and Bailly [104]. Far-field experimental data are available from the Von Karman Institute (VKI) where single and dual-stream jets at similar test conditions were tested [105]. The comparison of results obtained from Cosmic with both ex-

4. SUPERSONIC UNDER-EXPANDED SINGLE JET

perimental and numerical data from third parties is extremely important to build confidence in the solver capabilities and in its ability to effectively capture aeroacoustic phenomena linked to supersonic free jets.

4.1 Experimental set-up

The set-up of the single jet experimental apparatus consists of a contoured convergent nozzle with an exit diameter $D_e = 38.0$ mm and a nozzle exit Mach number $M_e = 1.0$. The nozzle is operated under-expanded at the stagnation to ambient pressure ratio $p_s/p_\infty = 2.27$. The nozzle lip thickness t_e is $0.0131D_e$. The flow at the nozzle exit is axial. This cold air jet has an exit stagnation temperature of 303.15 K. The modelled exit and ambient conditions match those in the experimental set-up of André [4]. The nozzle exit static density, axial velocity, pressure, and temperature are 1.6206 kg/m³, 318.6 m/s, 117.52 kPa, and 252.62 K, respectively. The jet discharges in initially quiescent air at temperature $T_\infty = 288.15$ K and pressure $p_\infty = 98.0$ kPa. The Reynolds number, Re , based on the jet exit diameter is 1.2×10^6 and the fully expanded jet Mach number $M_j = 1.15$. The air flow is modelled under constant specific heat ideal gas assumptions, with specific gas constant $R_g = 287.058$ J/(kg K) and specific heat ratio $\gamma = 1.4$.

4.2 Mesh and numerical set-up

The overall computational domain for the simulation, shown in Fig. 4.1, extends for $50D_e$ downstream of the nozzle exit plane and $15D_e$ upstream of it. The domain is composed of the physical domain and of a sponge layer. For the physical do-

4. SUPERSONIC UNDER-EXPANDED SINGLE JET

main, a contoured boundary is used in the radial direction with a minimum extent of $5D_e$ at the nozzle exit plane and a maximum extent of $6.0D_e$ at the physical domain outflow placed at $20D_e$ from the nozzle exit plane. In the upstream axial direction, the physical domain extends to $-4D_e$. The compliant layer, or sponge layer, extends over the range $20D_e \leq x \leq 50D_e$ in the downstream axial direction, over the range $-15D_e \leq x \leq -4D_e$ in the upstream axial direction, and up to $20D_e$ in the radial direction. The computational domain is discretised in finite volumes using a structured multi-block body-fitted Cartesian mesh. A butterfly mesh topology is built around a prismatic mesh block running through the nozzle axis. The nozzle is discretised with 860,160 cells ($240 \times 56 \times 64$), the surrounding of the nozzle with 7,604,160 cells ($267 \times 445 \times 64$) and the jet area with 57,337,536 cells ($1713 \times 523 \times 64$) for a total of around 65.8×10^6 cells. Mesh clustering close to the nozzle walls is implemented to achieve a near-wall resolution of $y^+ = 1$ at the nozzle exit along the nozzle walls with 25 points in the boundary layer and a mesh expansion ratio of 30%. The mesh cut-off frequency at the point $(0D_e, 3D_e)$ is $St = 2.5$ with approximately 30 points per wavelength. Inside the physical domain, topological surfaces are defined for the collection of data used to perform the Ffowcs Williams and Hawkings acoustic analogy and arrays of probes are defined to extract quantities at locations of interest. Three surfaces are defined starting from a radial distance of $2D_e$, $3D_e$, and $4D_e$ over the nozzle exit plane and are parallel to the contoured radial boundary. The arrays of probes are placed on the axis, on the lip line, and at radial distances of $1D_e$, $2D_e$, and $3D_e$. The probes are placed every $\Delta x = 0.1D_e$ and there are 18 arrays in the azimuthal direction for each radial position. The axial and lip line arrays are parallel to the jet axis, while the others present a positive expansion angle $\vartheta = 5^\circ$. Both topological surfaces and probes

4. SUPERSONIC UNDER-EXPANDED SINGLE JET

are extracted at a frequency of 200 kHz. Axial planes spaced by $\Delta x = 1D_e$ are extracted at a frequency of 100 kHz, together with the $y = 0$ and the $z = 0$ planes.

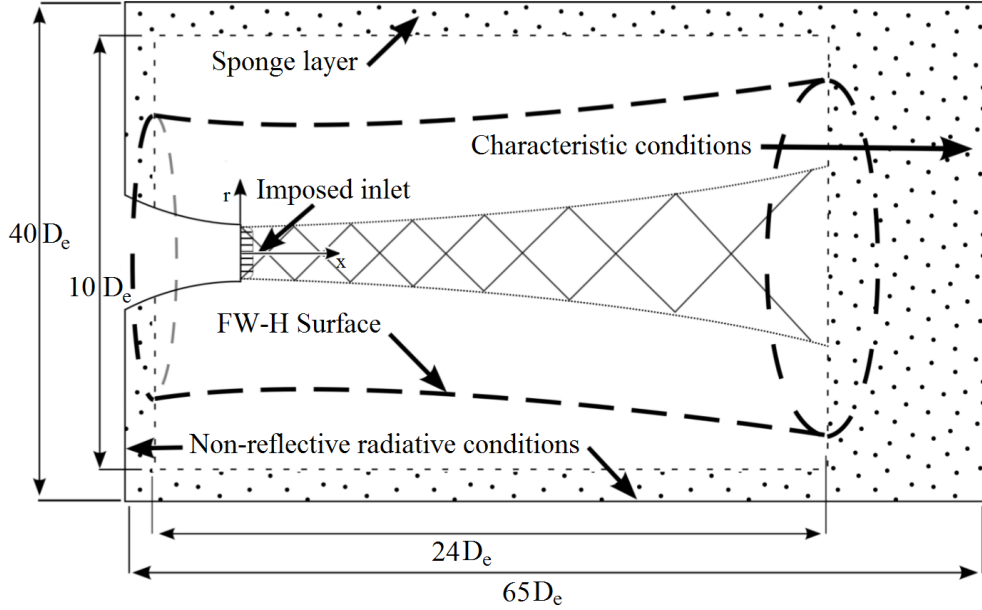


Figure 4.1: Sketch of the computational domain adopted for the DES simulation.

Inside the nozzle, at the computational domain inflow, a uniform axial inflow is imposed from the values of the stagnation pressure and temperature reported in Section 4.1, assuming an isentropic expansion to the nozzle exit of the bulk flow. The flow inside the nozzle is tripped at the axial position $x = -1D_e$ following the approach proposed by Bogey [106]. This tripping is necessary to obtain turbulent flow type profiles of turbulence intensity in the shear layer developing from the nozzle lip. Above the contoured nozzle, at the computational domain inflow boundary, a subsonic inflow boundary condition is imposed with a uniform axial inflow Mach number of 0.1 and ambient laboratory pressure, as detailed in Section 4.1. The radial boundary and the outflow boundary are modelled by extrapolating the flow from the interior of the computational domain. The computation is started

4. SUPERSONIC UNDER-EXPANDED SINGLE JET

from a quiescent zero flow condition imposed over the full computational domain. This starts the jet impulsively and the computation is time-marched through 120 non-dimensional time units ($\hat{t} = t c_{ref}/D_e$) to allow the jet to develop statistically stationary characteristics. Thereafter, the computation is further time-advanced by 120 non-dimensional time units during which time-mean and root-mean-square estimates of the flow state are obtained.

4.3 Results

Results are presented in this section and compared with published experimental and numerical data. This comparison has, as its main goal, the assessment of the numerical predictions from Cosmic and the feasibility of using Cosmic for an aeroacoustic investigation of the aerodynamic sources of broadband shock associated noise.

Figure 4.2 shows a snapshot taken from the DES simulation. It is possible to clearly identify the key features of a supersonic under-expanded flow, with diamond-shaped shock cells strongly interacting with turbulent structures being convected downstream inside the mixing layer. The instantaneous Mach number isosurfaces are denoted with colours and the pressure field fluctuations are shown by levels of grey. Strong pressure waves can be identified in the whole domain travelling in the upstream and in the downstream directions.

The shock-cell noise frequency is inversely related to the size of the shock cells and, more specifically, to the axial distance between the locations where the shocks interact with the most energetic turbulence scales from the first Kelvin-Helmholtz shear-layer instability. The time-averaged Mach number axial profile obtained from

4. SUPERSONIC UNDER-EXPANDED SINGLE JET

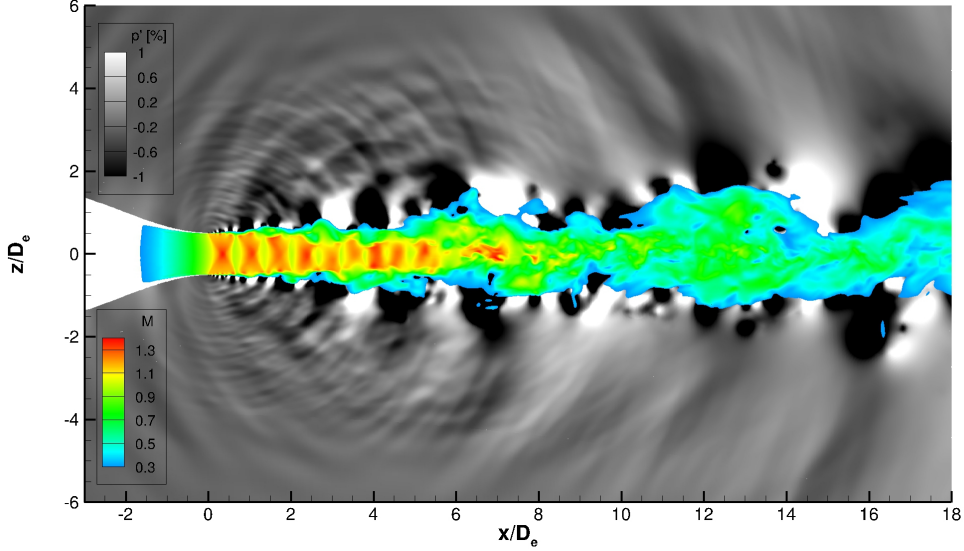


Figure 4.2: Instantaneous iso-colour levels of streamwise Mach number and grayscale levels of pressure fluctuation of a $M_j = 1.15$ under-expanded jet.

1.2M iterations is shown in Fig. 4.3 and compared with numerical results from *elsA* [100] and experimental results from André [4]. A very good agreement is obtained in the shock-cell spacing for the first four shock cells between the Cosmic prediction and the experiment. As shown in Table 4.1, the axial length of the first two shock cells are accurately predicted to three significant digits and the error for the first 4 shock cells is limited to around 3%. The error is larger for the fifth shock cell, at 10%. On the other hand, the prediction from *elsA* shows a shift in the shock cell location starting from the second shock cell. The shift becomes more evident for the following shock cells, showing a smaller shock-cell length compared to the experiment. As far as the shock-cell amplitudes are concerned, the prediction from Cosmic does not appear as accurate as for the shock-cell length for the first two shock cells. The first shock-cell amplitude appears to be overestimated, however the

4. SUPERSONIC UNDER-EXPANDED SINGLE JET

experimental data do not follow the expected trend of a strong first shock followed by shocks of lower intensity. On the other hand, the shock intensity predicted for the following shock cells has a lower amplitude than what was measured in experiments. As reported in Table 4.2, the errors for the first five shock cells are limited to a maximum of 3.2%. A different trend is observed for *elsA*, with the predictions showing a higher shock-cell amplitude for all shock cells with respect to the experiment. While the Cosmic prediction shows a decay in the Mach number at the end of the potential core at around $5D_e$, *elsA* better follows the average Mach number observed in the experiment, even if the predicted potential core extends more than $2D_e$ downstream of the end of the experimental potential core. The differences in shock-cell length and amplitude between the experiment and the Cosmic computation can be attributed to the low order of the scheme that is used by Cosmic in the presence of a shock introducing high numerical viscosity. To obtain better results, an increased spatial resolution is likely to be required.

	Cosmic	Exp. [4]	% error
L_1/D_e	0.725	0.725	0.0%
L_2/D_e	0.679	0.679	0.0%
L_3/D_e	0.666	0.686	-3.0%
L_4/D_e	0.626	0.646	-3.2%
L_5/D_e	0.587	0.646	-10.0%
\bar{L}_{avg}/D_e	0.657	0.676	-2.9%

Table 4.1: Shock-cell axial length comparison between Cosmic and experimental data from André [4].

	Cosmic	Exp. [4]	% error
M_1	1.376	1.343	2.4%
M_2	1.319	1.353	-2.6%
M_3	1.282	1.336	-3.0%
M_4	1.259	1.284	-3.2%
M_5	1.236	1.273	-2.9%
\bar{M}_{avg}	1.294	1.318	-1.8%

Table 4.2: Shock-cell amplitude comparison between Cosmic and experimental data from André [4].

Figure 4.5 shows that there is very good agreement in the axial velocity profiles among the numerical predictions and the experiment for all three extraction lines at $x = 0.16D_e$, $x = 0.34D_e$, and $x = 0.52D_e$ shown in Fig. 4.4. The three lines are

4. SUPERSONIC UNDER-EXPANDED SINGLE JET

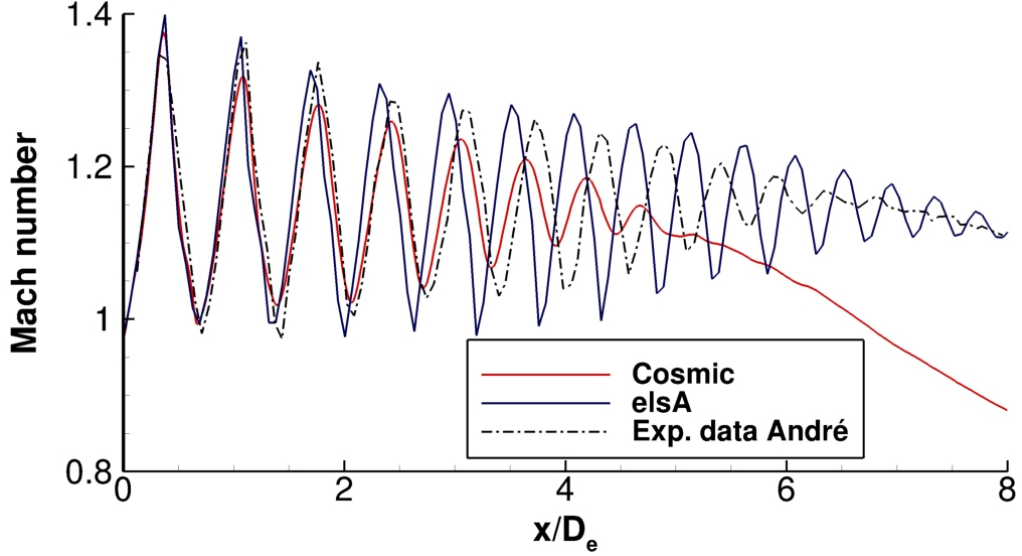


Figure 4.3: Mach number distribution along the axis of a $M_j = 1.15$ under-expanded jet. Numerical data from Cosmic and *elsA* [100]. Experimental results from André [4].

extracted at the middle point of the first shock cell expansion region, at the end of the first shock cell expansion region, *i.e.* point of maximum Mach number, and at the middle point of the first shock cell compression region, respectively. At all three positions, Cosmic shows a thinner shear layer than both *elsA* and the experiment indicated by a sharper change in velocity around $y = 0.5D_e$. In Fig. 4.5(c), the difference in axial velocity close to the axis between the numerical predictions and the experiment confirms the difference that can be observed in Fig 4.3 in the compression region of the first shock cell with the numerical predictions experiencing a slight inflection that is not observed in the experiment.

Well-predicted axial velocity profiles are not sufficient to correctly capture the development of shear-layer instabilities, therefore a tripping function was added to initiate the growth of such instabilities. Such function allows the supersonic jet to transition to a fully turbulent flow within $D_e/2$ from the nozzle exit plane. To sup-

4. SUPERSONIC UNDER-EXPANDED SINGLE JET

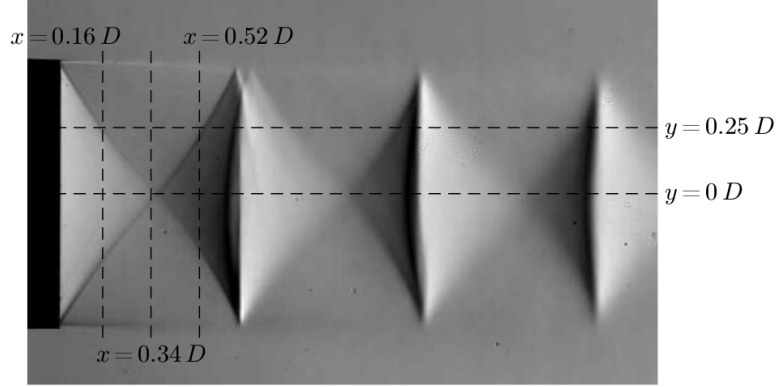


Figure 4.4: Lines of extraction for the radial distributions of axial velocity for a $M_j = 1.15$ under-expanded jet. Image taken from André [4].

port this statement, the *rms* values of the axial and tangential velocity components are shown in Fig. 4.6. The modelled flow starts as laminar both on the axis and in the shear layer. By $x = 0.5D_e$, the flow reaches *rms* velocity levels of the same magnitude as in the experiment. The predicted axial and tangential *rms* velocity components in the shear layer from Cosmic are higher than in the experiment. This is probably due to a slight over-estimation of the tripping function parameters in the current simulation. A reduction in the tripping function parameters would most probably lower the *rms* values for both velocity components. In the Cosmic prediction the *rms* levels are sustained in the downstream direction while a *rms* steady axial decay is observed for *elsA*.

The analysis of the jet plume statistical quantities gave satisfactory agreement with experiment. This gives some confidence that time-dependent predictions at discrete locations inside the domain should also give an adequate representation of the flow field. In Fig. 4.7, the Power Spectral Density (PSD) of the predicted pressure fluctuation in the near field of the jet is shown. Figures 4.7(a,d), 4.7(b,e), and 4.7(c,f) show respectively the PSD from the predicted pressure fluctuations at

4. SUPERSONIC UNDER-EXPANDED SINGLE JET

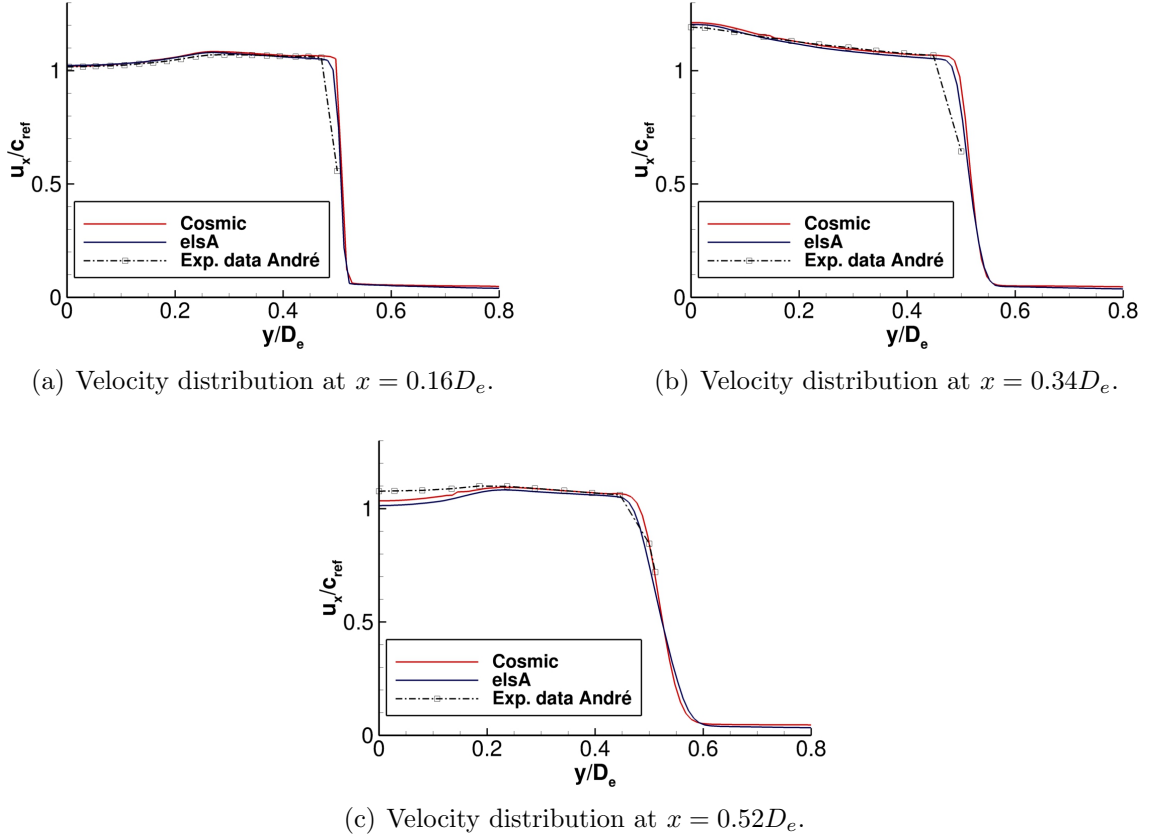


Figure 4.5: Axial velocity distribution in the radial direction for a $M_j = 1.15$ under-expanded jet. $\theta = 0$ meridional plane. Numerical data from Cosmic and *elsA* [100]. Experimental results from André [4].

radial locations $r = 1D_e$, $2D_e$, and $3D_e$ on the meridional plane ($\theta = 0$) from Cosmic and *elsA*. The PSD is expressed as dB/St and it is plotted as function of the normalised axial location x/D_e and of the Strouhal number $St = f D_e/c_{ref}$. The first row of results has been obtained with the numerical scheme Cosmic, while the second one is the output from *elsA*. The spatial resolution of the abscissa in Fig. 4.7 is $\Delta x = 0.1D_e$. The overall agreement in the predictions from the two schemes is good and the main characteristics of shock-cell associated noise are present in both sets of results. Analysing Fig. 4.7 with respect to measurements by Savarese [107]

4. SUPERSONIC UNDER-EXPANDED SINGLE JET

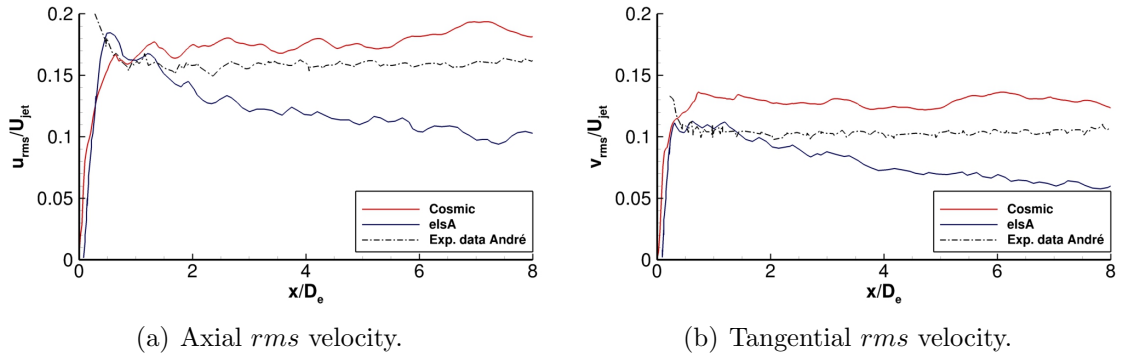


Figure 4.6: *Rms* velocity profiles on the nozzle lip line for a $M_j = 1.15$ under-expanded jet. Numerical data from Cosmic and *elsA* [100]. Experimental results along the lip line from André [4].

for a similar test case, it is possible to observe the ‘banana’ shaped component of noise at high frequency typical of broad-band shock associated noise. This is shown as a region of high PSD starting from around $St = 0.7$ at $x/D_e = 0$ and extending to $St = 1.6$ at $x/D_e = 6$. The axial extent of the ‘banana’ is smaller for the Cosmic prediction, $x/D_e \approx 6$, due to a shorter shock train structure with respect to *elsA* which predicts the axial extent of the shock train as $x/D_e \approx 8$. This shows a clear dependence of these frequency components of the pressure fluctuation upon the shock cells. The lower Strouhal number components in Fig. 4.7 are instead related to large turbulence structures and they have a predominant hydrodynamic nature. The rapid decay in the radial direction of these lower Strouhal number components predicted by *elsA* is not matched in Cosmic. This is probably due to larger turbulence structures present in the simulation performed with Cosmic that are caused by the coarser azimuthal discretisation used in the Cosmic simulation. The coarser azimuthal discretisation of the domain does not allow to resolve well the breakdown of shear-layer toroidal instabilities into fine-scale turbulence. This produces larger structures convected in the downstream direction compared to *elsA*.

4. SUPERSONIC UNDER-EXPANDED SINGLE JET

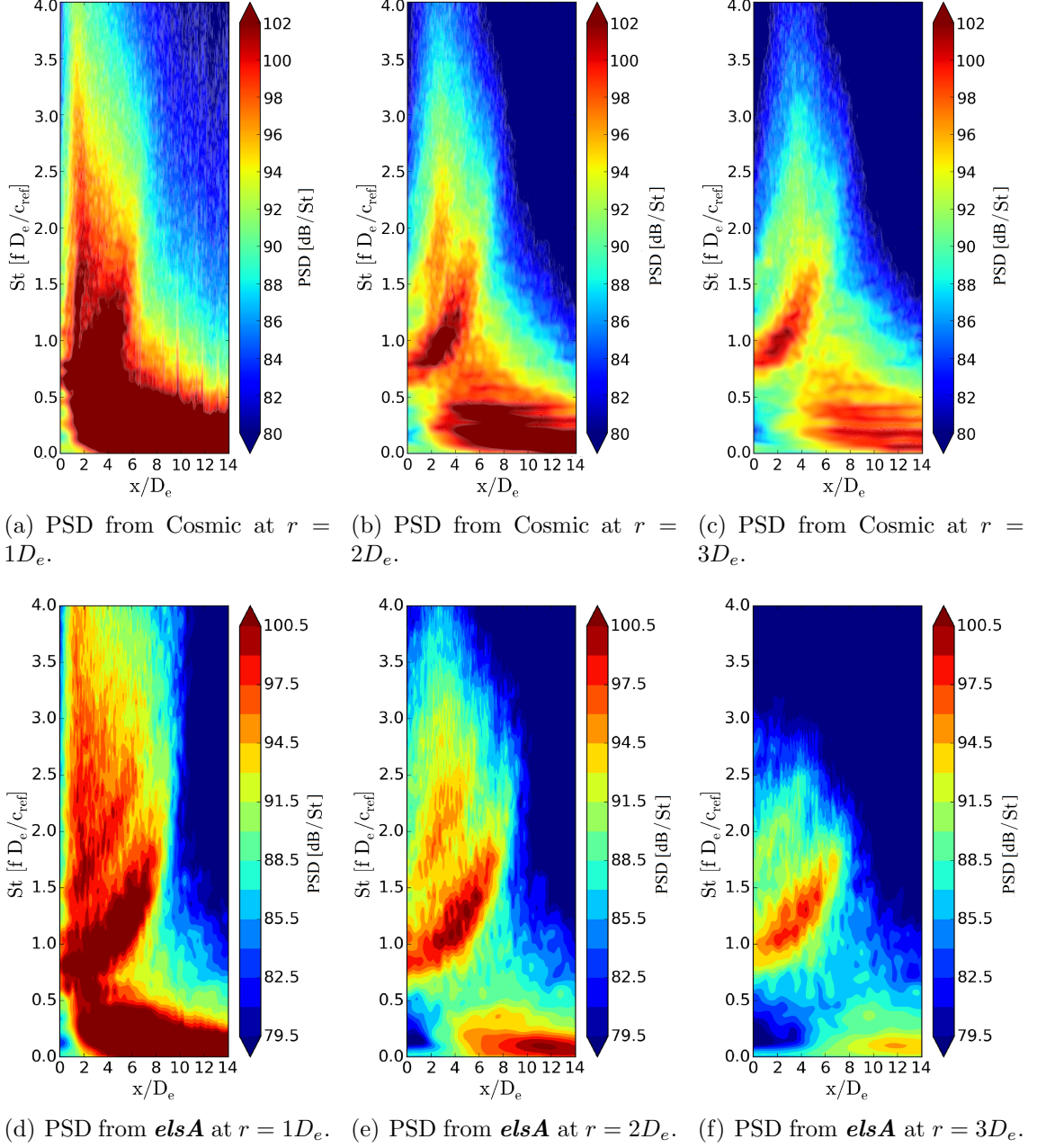


Figure 4.7: Power Spectral Density at different radial locations for a $M_j = 1.15$ under-expanded jet obtained with the numerical schemes Cosmic and *elsA* [100].

These structures are responsible for strong hydrodynamic perturbations travelling in the near-field of the jet. This hypothesis appears to be corroborated by Fig. 4.8(a)

4. SUPERSONIC UNDER-EXPANDED SINGLE JET

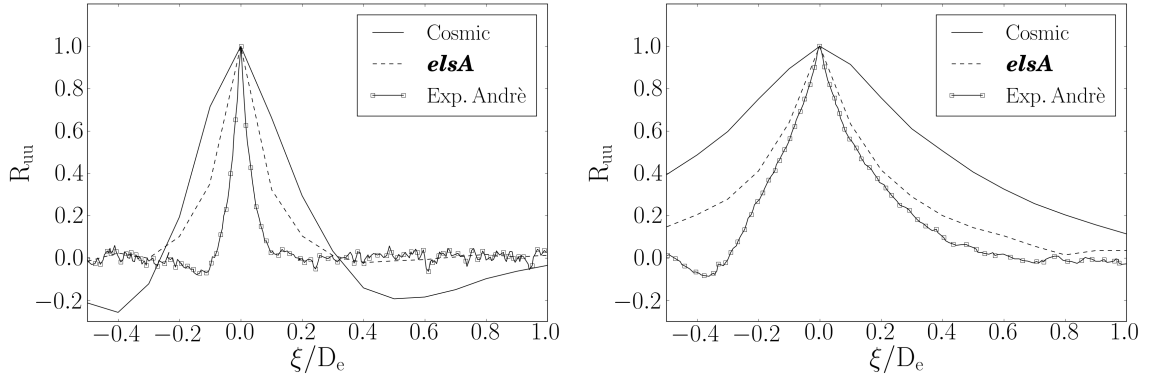
and 4.8(b) where the spatial velocity autocorrelation in the axial direction is shown along the nozzle lip line for the axial positions $x = 1.5D_e$ and $x = 9.0D_e$ respectively. The autocorrelation gives an estimate of the size of the turbulence structures developing in the shear layer and it is evaluated with the same formulation as in André [4],

$$R_{uu}(\bar{x}, \bar{\xi}) = \frac{\langle u'(\bar{x}, t) u'(\bar{x} + \bar{\xi}, t) \rangle}{u^{rms}(\bar{x}) u^{rms}(\bar{x} + \bar{\xi})}, \quad (4.1)$$

where the angle brackets $\langle \bullet \rangle$ indicates averaging with respect to t , u' is the axial velocity perturbation, u^{rms} is the axial velocity root mean square, x is the current position, and ξ is the autocorrelation axial distance from x that is discretised in steps of $0.1D_e$ in this study. For the Cosmic simulation, the number of available samples for the time average is 2,400. Comparing Fig. 4.8(a) and Fig. 4.8(b), it is possible to appreciate the growth of the turbulence shear-layer structures in the downstream direction. Both numerical predictions overestimate the size of the turbulence structures, however Cosmic presents a larger overestimation with respect to **elsA**, confirming the presence of large organised structures developing and travelling in the downstream direction.

By integrating the axial velocity autocorrelation between $R_{uu} = 0.1$ and $R_{uu} = 1$ at different axial locations, the turbulence length-scale is evaluated and presented in Fig. 4.9. While **elsA** shows a similar growth rate to the experimental observations, even though it is translated by around 1.5 diameters in the axial direction, Cosmic exhibits a different behaviour with a much faster growth rate experienced in the first 3 diameters from the nozzle exit plane. This observation confirms the hypothesis on the limitations in capturing the breakdown of shear-layer toroidal instabilities into fine-scale turbulence of the Cosmic simulation. These limitations, as previously

4. SUPERSONIC UNDER-EXPANDED SINGLE JET



(a) Axial velocity autocorrelation at $x/D_e = 1.5$. (b) Axial velocity autocorrelation at $x/D_e = 9.0$.

Figure 4.8: Lip line axial velocity autocorrelation at $x/D_e = 1.5$ and $x/D_e = 9.0$ for a $M_j = 1.15$ under-expanded jet. Comparison with numerical data from Pérez [100] and experimental results from André [4].

stated, can be ascribed to an insufficient azimuthal discretisation coupled with the higher numerical viscosity of the lower-order scheme of Cosmic triggered by the scheme upwinding across the shocks.

Far-field noise predictions were obtained from Cosmic by the application of the Ffowcs Williams and Hawkings acoustic analogy, as implemented by Di Stefano [108]. The analysis uses the aerodynamic flow data extracted on a surface placed at $r = 3D_e$, as sketched in Fig. 4.1. Figure 4.10 shows the PSD at $50D_e$ from the jet exit measured by André [4] and by Guariglia [105], and numerical results obtained with Cosmic and *elsA* [100]. The plots are shown for polar angles of 50, 80, 110 and 140 degrees with respect to the nozzle outflow direction. The polar distance R is referenced to the nozzle exit plane centre. The measurements from André [4] and from Guariglia [105] show a good agreement at all four polar angles, confirming the repeatability of the experiment. The discrete peaks in PSD are from screech, a complex phenomenon that depends on several factors [19]. The shape and thickness of the nozzle lip affect the screech noise characteristics [38] and can

4. SUPERSONIC UNDER-EXPANDED SINGLE JET

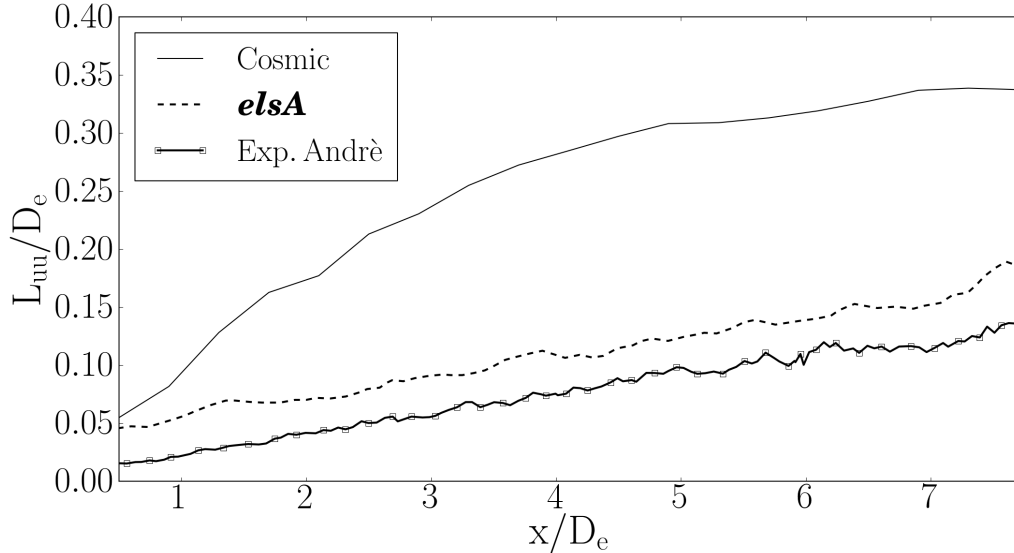


Figure 4.9: Lip line turbulence length scale for a $M_j = 1.15$ under-expanded jet. Comparison with numerical data from Pérez [100] and experimental results from André [4].

account for the different Strouhal number spectral peaks observed in the two experiments. The jet noise radiated is shown to have significant directivity as shown by the PSD dependence on the polar angle of Figs. 4.10(a)-(d). While results from the jet modelled by *elsA* show a general underestimation of the PSD at low Strouhal numbers, the opposite is true for the jet modelled by Cosmic. A large contribution to the unsteady pressure fluctuations from low Strouhal number components was also observed in Fig. 4.7 in the near-field. The presence of this component in the far-field is not compatible with the discussion of Fig. 4.7 where this contribution was interpreted as coming from the non-radiating hydrodynamic field. The large far-field low Strouhal number contribution could be a numerical artefact from the spurious disturbances of long wavelength travelling through the finite-length computational domain. Such disturbances may be caused by a complex interaction between the

4. SUPERSONIC UNDER-EXPANDED SINGLE JET

flow exiting the domain, the sponge region, and the boundary conditions. To prevent this from happening in the dual jet simulation of Chapter 5, a second-order filter for the sponge region [91] is implemented to make sure that waves travelling in the sponge region are effectively damped. As far as the high frequency components are concerned, it is observed that the mesh cut-off wavenumber in *elsA* does not allow to resolve frequencies higher than $St \approx 1.2$. For Cosmic, on the other hand, the mesh discretisation has been defined to resolve higher wavenumbers than with the mesh used in *elsA* and a good agreement at high frequencies is observed for $\theta = 50^\circ$ and $\theta = 80^\circ$ in Fig. 4.10. In the upstream direction, at the polar angles $\theta = 110^\circ$ and $\theta = 140^\circ$, the high frequency component of the radiating pressure is underestimated by both numerical methods *elsA* and Cosmic. Scattering and interference phenomena occurring in the experiment could be the reason of this mismatch at high polar angles in the far-field.

Screech noise component is not predicted by either numerical simulation. Pérez [100] identifies the causes for the absence of screech in the *elsA* simulation in the definition of the initial conditions for the LES, in a poor discretisation of the nozzle lip region, and in the absence of the nozzle interior region, three aspects of key importance [50, 109, 67, 110]. The inflow conditions in *elsA* LES are extracted from a RANS simulation and imposed directly at the nozzle exit plane, posing problems to the development of the right turbulence structures for the development of screech. Even if the Cosmic domain comprises the interior nozzle region, the presence of a RANS boundary layer imposed by the DES approach raises doubts about the possibility of developing appropriate shear-layer receptivity conditions for the screech to develop. The discretisation of the nozzle lip region is also a critical aspect due to the necessity of correctly capturing the interaction of upstream travelling distur-

4. SUPERSONIC UNDER-EXPANDED SINGLE JET

bances with the nozzle lip which provides the closing step for the screech feedback loop [16]. Both Cosmic and *elsA* meshes may have insufficient spatial refinement in this region. Finally, the higher numerical dissipation of the lower-order scheme implemented in Cosmic might play a role in damping the disturbances interacting with the nozzle lip in a region of strong gradients.

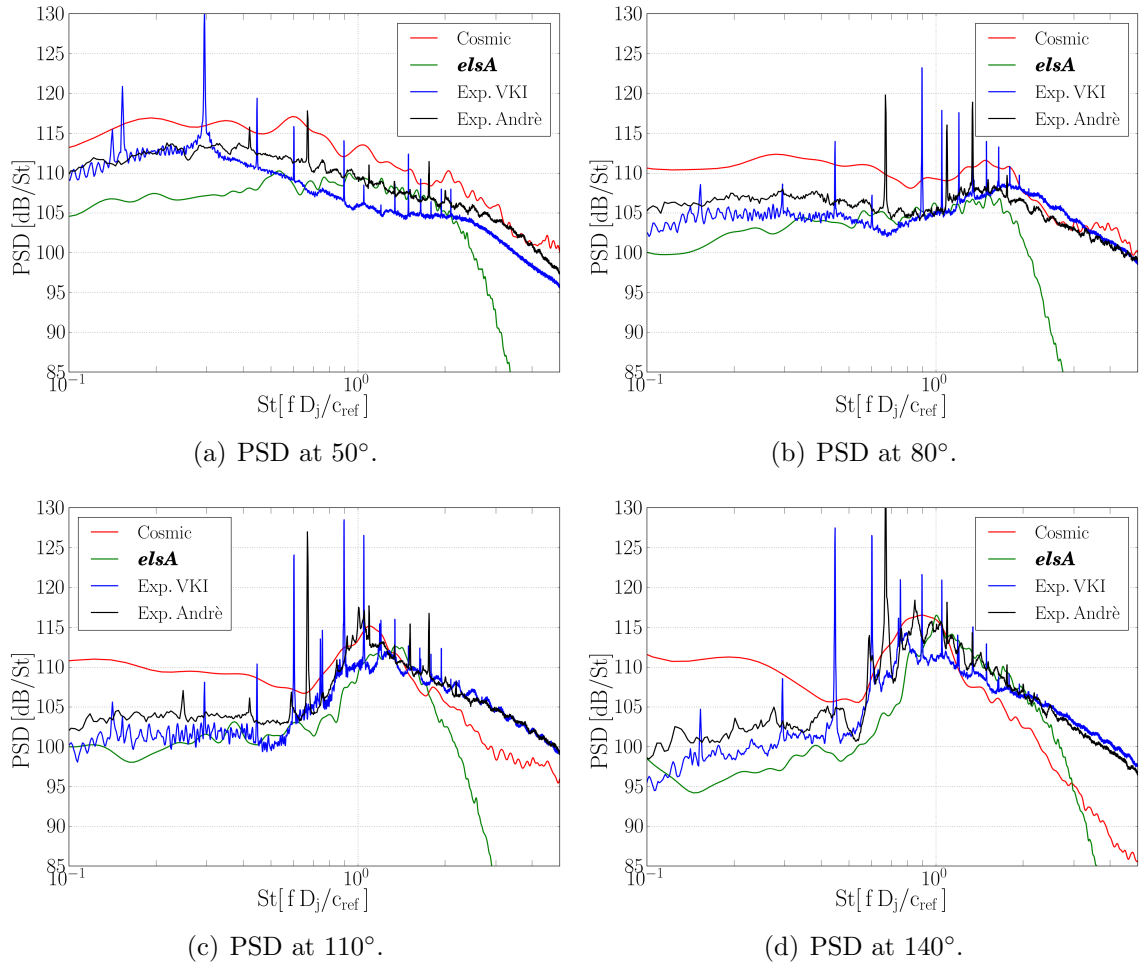


Figure 4.10: Acoustic spectra in the acoustic far-field at $R = 50D_e$ for a $M_j = 1.15$ under-expanded jet. The angle θ is measured with respect to the jet axis. Comparison with numerical data from Pérez [100] and experimental results from André [4] and from Guariglia [105].

Figures 4.11(a) and 4.11(b) show the Overall Sound Pressure Level (OSPL) com-

4. SUPERSONIC UNDER-EXPANDED SINGLE JET

puted over the whole frequency domain and over the narrower frequency range $St = 0.4$ to $St = 2.0$ respectively. As observed in Fig. 4.10, the overestimation of the low frequency components in Cosmic causes an overestimation of the OSPL at low θ angles up to $\theta = 90^\circ$ as observed in Fig. 4.11(a). The mean error in the prediction of the OSPL over the whole range of frequencies is equal to 1.31dB re $20\mu\text{Pa}$ with respect to the experimental data of André [4], taken as reference values, with a maximum error of 2.44dB re $20\mu\text{Pa}$ at $\theta = 140^\circ$. The predicted OSPL from *elsA* suffers from the underestimation of the high Strouhal number contributions to the OSPL caused by the mesh design, as previously discussed, and shows a global underestimation at all angles. By reducing the Strouhal number integration range to $St = 0.4 - 2$, thus isolating the frequency components related to BBSAN, the predictions from *elsA* show a very good agreement with experimental data as displayed in Fig. 4.11(b). Cosmic, on the other hand, presents a similar behaviour to Fig. 4.11(a), with higher OSPL values for angles lower than $\theta = 90^\circ$ and slightly higher errors compared to the whole frequency domain integration, with a mean error of 1.62dB re $20\mu\text{Pa}$ and a maximum error of 2.81dB re $20\mu\text{Pa}$ at $\theta = 90^\circ$ with respect to the experimental data of André [4]. A sudden increase in OSPL is observed in the experimental data of André [4] at $\theta = 130^\circ$ and higher than expected values are also obtained at $\theta = 140^\circ$ and $\theta = 150^\circ$. This behaviour is most probably caused by a strong increase in the screech noise peaks observed at these angles in the experiment of André [4] as shown in Figure 4.3 in André [4]. At $\theta = 130^\circ$, the main screech peak becomes wider and grows in amplitude from around 126dB to more than 132dB. This increase is accompanied by a similar behaviour observed for all of the secondary screech noise peaks.

The validation test case provided important insights on the behaviour of the Cos-

4. SUPERSONIC UNDER-EXPANDED SINGLE JET

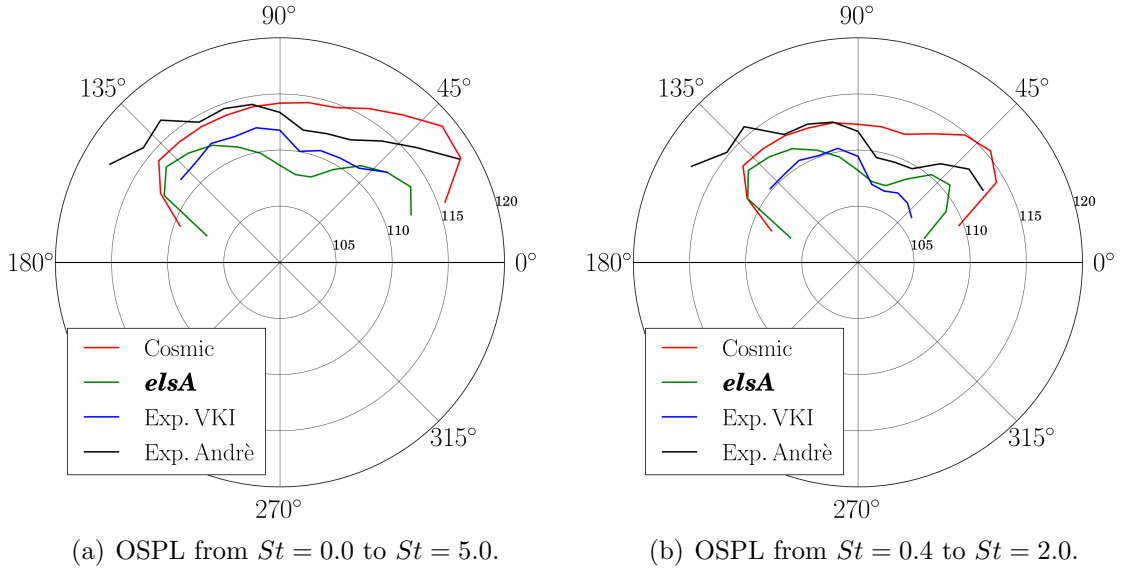


Figure 4.11: OSPL in the far-field computed at $R = 50D_e$ for a $M_j = 1.15$ under-expanded jet. Comparison with numerical data from Pérez [100] and experimental results from André [4] and Guariglia [105].

mic numerical method applied to the CAA analysis of supersonic under-expanded jets. The mesh design proved of major importance under several aspects. The axial discretisation must provide an appropriate spatial resolution to capture the shock-cell pattern without excessive dissipation in order to properly predict the amplitude and location of the shock cells as shown in Fig. 4.3. The radial discretisation can have a strong impact on the ability of the simulation to capture high Strouhal number noise components, as observed for the results obtained using *elsA* in Fig. 4.10. In the single jet simulation with Cosmic, there seem to be no issues with respect to the radial discretisation, giving confidence that the same mesh design approach can be adopted for the dual-stream jet simulation of Chapter 5. With respect to the azimuthal discretisation, on the other hand, the mesh used with Cosmic suffered from low spatial refinement, with just 64 cells covering the 360° of the azimuthal direction. Because of this insufficient azimuthal refinement, a proper breakdown of

4. SUPERSONIC UNDER-EXPANDED SINGLE JET

turbulence structures travelling in the shear layer could not be modelled, leading to excessively large coherent structures travelling in the downstream direction, as shown by Fig. 4.8 and Fig. 4.9. Regarding the boundary conditions for the simulation, the single jet simulation shows that it is necessary to implement a filter function to effectively damp perturbations travelling in the sponge region to avoid the reflection and onset of spurious long period oscillations in the flow field that can generate very high low Strouhal number numerical noise components as observed in Fig. 4.7 and 4.10. Finally, the tripping function applied inside the nozzle appears to successfully act on the flow to force the turbulence transition within a short axial distance from the nozzle exit plane as shown in Fig. 4.6. Fine tuning of the tripping parameters, coupled with proper mesh design, is necessary to model a representative turbulence level in the shear layer for this high Reynolds number jet.

The outcome of the validation test case is satisfactory, with a general good agreement of the Cosmic predictions both with numerical and experimental data from third parties. The results highlighted areas of possible improvement for the coaxial flow simulation and there is confidence that engineering accurate results of such a complex flow can be obtained with Cosmic. From the analyses carried out in this chapter, it is possible to conclude that Cosmic is a viable tool for aeroacoustic studies of supersonic jets, provided it is used judiciously with an appropriate awareness of its limits.

Chapter 5

Supersonic under-expanded dual-stream jet

The dual-stream jet test case presented in this chapter has been defined in collaboration with Airbus France, who provided the design and run conditions of the nozzle. This test case is a simplification of the coaxial nozzles that are used in civil aircraft engines and it is expected to provide Airbus with an interesting insight into the physics of coaxial jets. The test conditions here presented have been tested experimentally at the von Karman Institute for Fluid Dynamics (VKI). Comparative numerical results have also been obtained at CERFACS [100] with the *elsA* solver described in Chapter 4.

5.1 Test case conditions

A coaxial nozzle geometry is used in which the primary stream is subsonic with an exit Mach number of $M_p = 0.89$ and the core nozzle pressure ratio $CNPR = 1.675$.

5. SUPERSONIC UNDER-EXPANDED DUAL-STREAM JET

The secondary stream is supersonic and under-expanded, with a design exit Mach number of $M_s = 1.20$ and a nozzle pressure ratio $FNPR = 2.45$. The jets issue from two concentric convergent nozzles with primary and secondary diameters of $D_p = 23.4$ mm and $D_s = 55.0$ mm respectively. The thickness of the two nozzle lips at exit is $t = 0.3$ mm. The jets are cold and their stagnation temperature matches the ambient temperature $T = 283.0$ K. The jets are discharged in initially quiescent air with pressure $p_\infty = 101.325$ kPa. The Reynolds numbers based on the jet exit diameters and perfectly expanded conditions are $Re_p = 0.67 \times 10^6$ and $Re_s = 2.64 \times 10^6$.

5.2 Mesh and numerical set-up

The mesh for the dual jet has similar features to the single jet mesh presented in Chapter 4 and a sketch of the numerical computational domain is shown in Fig. 5.1. The mesh contains 226×10^6 cells. It consists of a butterfly type mesh in order to avoid defining any zero area unit cell at the nozzle axis. The walls of the internal sections of the nozzles, as well as the external section of the primary nozzle, attain a resolution at the wall of $y^+ \approx 1$ with 25 points in the boundary layers. The maximum expansion ratio between adjacent cells achieved in the mesh is not greater than 4%. The radial domain size grows from the nozzle exit plane in the positive axial direction in order to take into account the expansion of the jet (from $r/D_p = 6$ at the exit of the primary nozzle to $r/D_p = 12$ at $x/D_p = 50$). The overall computational domain for the simulation extends to $80D_p$ downstream of the nozzle exit plane and to $-14D_p$ upstream of it. The domain, as for the single jet, is composed of the physical domain and of a sponge layer. For the physical domain, a

5. SUPERSONIC UNDER-EXPANDED DUAL-STREAM JET

contoured boundary is used in the radial direction with a minimum radial extent of $6D_p$ at the nozzle exit plane and a maximum radial extent of $12.0D_p$ at the physical domain outflow placed at $50D_p$ from the nozzle exit plane. In the upstream axial direction, the physical domain extends to $-4D_p$. The compliant layer, or sponge layer, extends over the range $50D_p \leq x \leq 80D_p$ in the downstream axial direction, over the range $-14D_p \leq x \leq -4D_p$ in the upstream axial direction, and up to $20D_p$ in the radial direction. As for the single jet test case, topological surfaces are defined inside the physical domain for the collection of data used to perform the Ffowcs Williams and Hawkings analogy as well as arrays of probes to extract quantities at locations of interest. Three surfaces are defined starting respectively from a radial distance of $3D_p$, $4D_p$, and $5D_p$ over the primary nozzle exit plane and running parallel to the contoured radial boundary. The arrays of probes are placed on the axis, on the primary and secondary nozzle lip lines, and at radial distances of $1D_p$, $2D_p$, and $3D_p$. The probes are placed every $\Delta x = 0.1D_p$ and there are 18 arrays in the azimuthal direction for each radial position. The lip line arrays follow the development of the shear layer, while the arrays at $1D_p$, $2D_p$, and at $3D_p$ are placed at a positive expansion angle $\vartheta = 8^\circ$ to the nozzle outflow direction. Both topological surfaces and probes are sampled at a frequency of 200 kHz. Axial planes spaced by $\Delta x = 1D_p$ are extracted at a frequency of 100 kHz, together with the $y = 0$ and $z = 0$ planes.

5.3 Experimental set-up

The experimental data presented in this chapter have been obtained at the von Karman Institute for Fluid Dynamics (VKI), as part of the AeroTraNet2 project.

5. SUPERSONIC UNDER-EXPANDED DUAL-STREAM JET

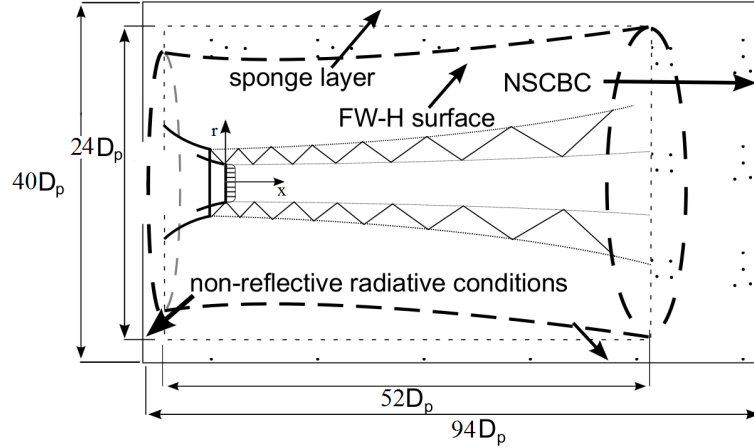


Figure 5.1: Sketch of the computational domain adopted for the dual jet simulation. The radial dimension is shown stretched compared to the axial dimension, for clarity.

The Free jet AeroacouSTic (FAST) facility was specifically designed and built to perform experiments on coaxial jets [111, 112], with the possibility of running single jet tests. The nominal test conditions for the primary and secondary nozzles are respectively $1.35 < CNPR < 1.72$ and $2.00 < FNPR < 2.50$. Due to delays in the manufacturing process of the nozzle at VKI, the CFD simulations at CERFACS were performed before the beginning of the experimental campaign at VKI. For this reason, geometrical differences are present between the numerical and the experimental geometries. For comparison purposes, the numerical simulation by Cosmic kept the same geometry as the one used by *elsA*. The main differences with respect to the experiments are here reported.

Figure 5.2 shows the Computer Aided Design (CAD) of the coaxial nozzle installed in the FAST facility. The effect of the screws used to attach the nozzle to the final part of the duct was assumed to be negligible and thus they are not modelled in the numerical simulations. More importantly, a coaxial nozzle of $D_p = 23.4$ mm and $D_s = 55$ mm could not be tested due to an excessive pressure loss in the air feed

5. SUPERSONIC UNDER-EXPANDED DUAL-STREAM JET

pipeline of the facility. Due to this loss in pressure, the apparatus was not able to meet the desired nominal pressure ratios and a reduction of 20% in the nozzle dimensions was applied to reduce the airflow demand during testing. For this reason, the primary nozzle diameter was reduced from $D_p = 23.4$ mm to $D_p = 19.2$ mm and the secondary nozzle diameter was reduced from $D_s = 55.0$ mm to $D_s = 44.0$ mm. The change in dimensions affects the Reynolds number Re_j , with an impact on the acoustics of the jet. Moreover, at the end of the testing campaign, a vertical displacement of the secondary nozzle of about 2 mm in the jet direction was observed from pictures taken during the operation of the facility. The reason for this displacement was identified at VKI in the vertical strain of the external duct caused by the pressurisation of the ducts. The effects of this displacement will be discussed later on in this chapter.

Two sets of experimental data are available for comparison: a far-field polar array of pressure probes and the time-averaged flow field obtained by Particle Image Velocimetry (PIV). The polar array, with a sampling frequency of 250 kHz, was placed at $70 D_p$ from the jet axis and the signal was acquired for around 67 seconds, giving about 2^{24} samples. The PIV velocity vector maps were obtained by means of two cameras set parallel to one another with a small overlapping region. The captured images had a resolution of $2,360 \times 1,766$ pixels² and were sampled at a frequency of 15 Hz. Two sets of experiments were performed with the same conditions with a different placement of the cameras in order to generate an extended view of the flow in the downstream direction. The experiments were run in five runs of 40 seconds, generating 600 images per run. A sample image of the composite vector map obtained by nesting two frame pairs is shown in Fig. 5.3. In Fig. 5.3, the left and right pairs are asynchronous and the composite of the two pairs was

5. SUPERSONIC UNDER-EXPANDED DUAL-STREAM JET

obtained by scanning the image dataset for reasonably congruent structures.

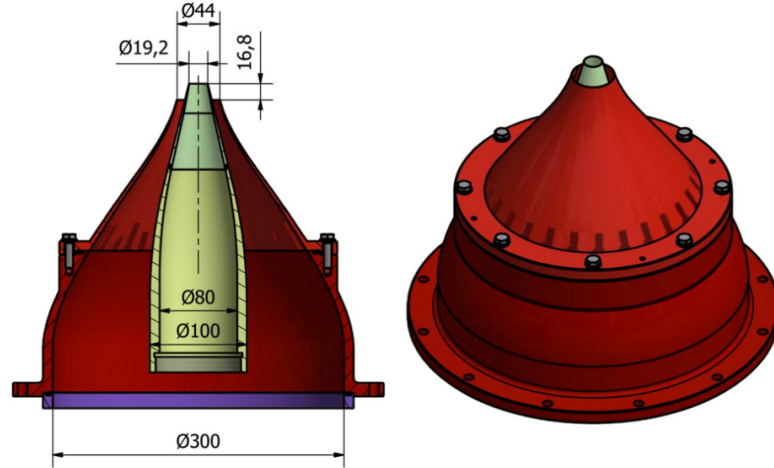


Figure 5.2: CAD drawings of the coaxial nozzle manufactured at VKI [105].

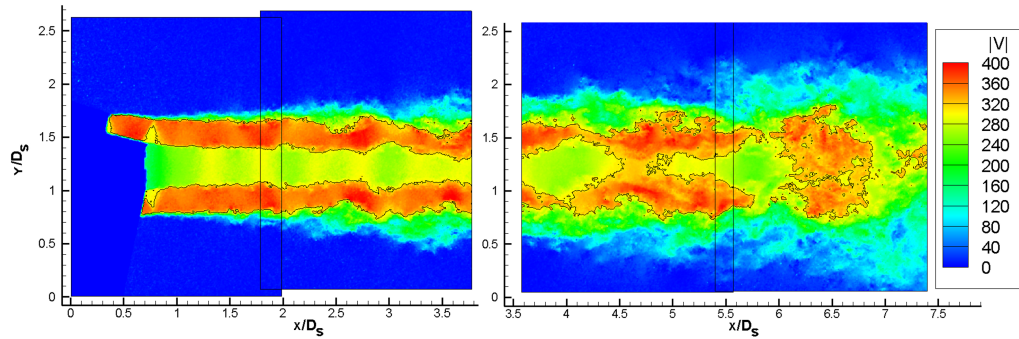


Figure 5.3: Instantaneous PIV in-plane velocity flow field with Mach number $M = 1$ isolines. CNPR=1.675 and FNPR=2.500, from Guariglia [105].

5.4 Results

The results obtained with Cosmic for the coaxial jet test case are compared with data obtained from *elsA* software and from the experiment at VKI. Time-averaged

5. SUPERSONIC UNDER-EXPANDED DUAL-STREAM JET

results are analysed first, followed by the analysis of the unsteady flow predictions and of the noise generation.

5.4.1 Time-averaged flow

The time averaging in Cosmic is performed over a period of 140 convective times (\hat{t}). In Fig. 5.4, time-averaged Mach contours are shown from Cosmic and *elsA*. The length of the potential core of the primary and secondary jet is different in the two sets of data, with the prediction from *elsA* presenting longer cores. This is expected, since Cosmic is based on a lower-order scheme and its intrinsic numerical dissipation is higher with respect to *elsA*, resulting in a faster reduction of the flow speed with axial distance from the nozzle exit. Moreover, both potential cores present a spatial phase shift in the axial sequence of the shock cells, with Cosmic predicting the onset of shock-cell structures closer to the nozzle with respect to *elsA*, with a consequent shift of the primary jet flow structures.

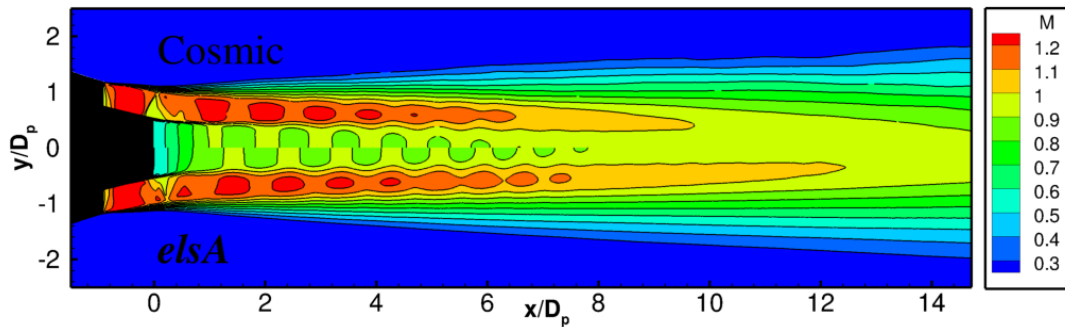


Figure 5.4: Time-averaged Mach number contours. Comparison between Cosmic and *elsA* [100] solvers.

The axial phase shift is caused by a different flow topology in the region above the primary nozzle wall where the expansion that develops at the nozzle lip of the secondary nozzle is reflected by the wall itself towards the outer shear layer, where

5. SUPERSONIC UNDER-EXPANDED DUAL-STREAM JET

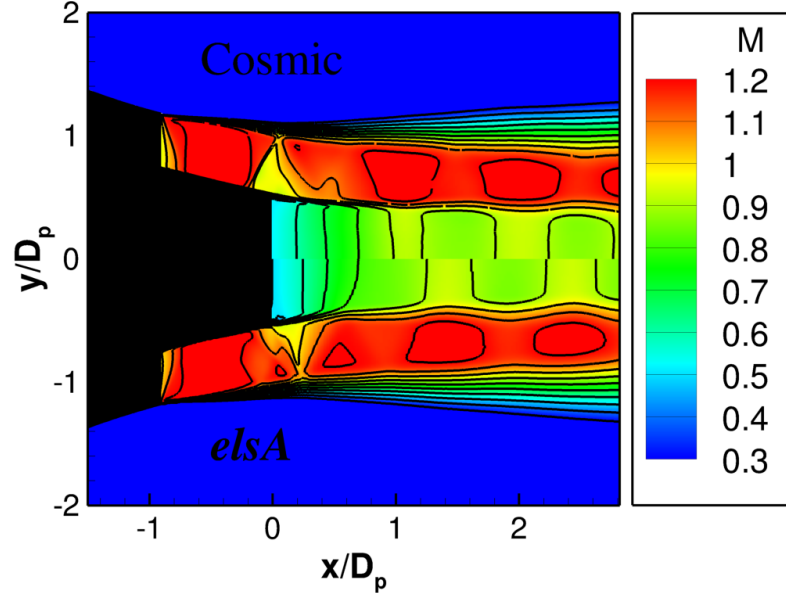


Figure 5.5: Time-averaged Mach number contours. Comparison between Cosmic and *elsA* [100] solvers.

it reflects back towards the nozzle axis as a shock. In the enlargement of Fig. 5.4 shown in Fig. 5.5, it is possible to clearly observe that the initial region of expansion and acceleration of the secondary stream, the red region, is longer in the *elsA* prediction than in the Cosmic prediction. For this reason, the first shock cell, yellow region, is predicted more upstream by Cosmic, with the shock standing on top of the primary nozzle exit plane. In the *elsA* prediction, on the other hand, the shock is anchored to the primary nozzle lip, developing downstream of it. Differences are visible also in the shape of the first shock and in the flow topology downstream of it. The first shock predicted by Cosmic appears to be larger and more regular in shape and it features a small tail that is not observed in *elsA*. Due to the shape and size of the shock cells, it appears that the two structures reach approximately the same axial position. The reason for the axial shift of the remainder of the shock-train is then to be found in the flow topology following the first shock. At

5. SUPERSONIC UNDER-EXPANDED DUAL-STREAM JET

the back of the first shock, there is the formation of a small region of accelerating flow caused by an expansion. This triangular region, well visible in the prediction by *elsA*, is less intense in the prediction from Cosmic, in which the flow is slower as shown by the almost absence of the fast flow region shown by the prediction from *elsA*. The discrepancy in the flow topology of the secondary jet downstream of the secondary nozzle exit plane is most probably caused by the presence of the RANS boundary layer in the DES Cosmic simulation. In the Cosmic prediction, the interaction of the expansion fan developing from the secondary nozzle lip and the boundary layer over the primary nozzle wall is affected by the transition from the RANS approach to the LES approach, causing the first shock cell to translate upstream and to develop a different shape than what is predicted by the pure LES approach in *elsA*. The different shock cell location affects its development and the interaction with the flow exiting from the primary nozzle, affecting in return the flow immediately downstream of the shock cell and thus causing an overall axial shift of the potential core structures of the secondary jet. The secondary stream flow topology affects the primary stream that appears also to be axially shifted.

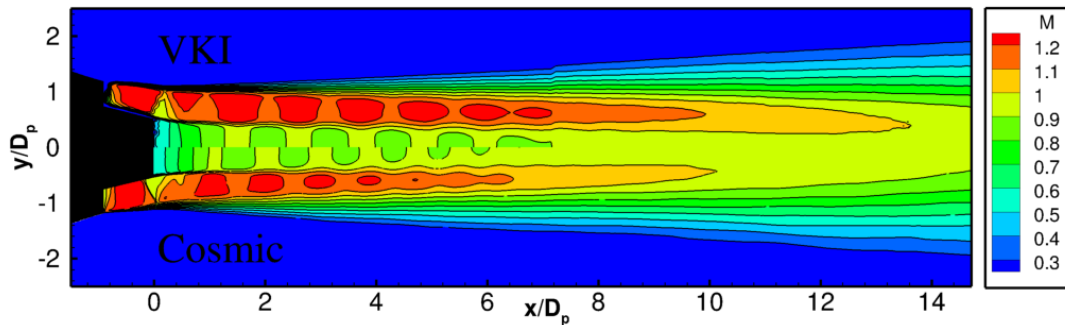


Figure 5.6: Time-averaged Mach number contours. Comparison between Cosmic and experimental results from VKI [105].

Comparing the time-averaged Mach number distribution predicted by Cosmic

5. SUPERSONIC UNDER-EXPANDED DUAL-STREAM JET

with the experimental results from VKI, it is possible to draw the same conclusions. The flow topology predicted by *elsA* is more in line with the one that is observed in the VKI experiment. The experiment presents larger shock-cell structures and higher velocities, but the flow topology observed above the primary nozzle exit plane confirms the limitations of the DES prediction and it is in good agreement with the pure LES prediction.

Figure 5.7 shows the time-averaged Mach number distribution of the secondary jet along a line defined as the average between the primary and the secondary shear layer radial positions as identified by the inflection point of their velocity profiles from Cosmic, *elsA*, and experiment. This extraction line is referred to as the middle of the secondary jet. As qualitatively observed in Fig. 5.4 and Fig. 5.6, a clear axial shift of the shock-cell structures is present starting from $x = 1.0D_p$. The first expansion predicted by the two numerical solvers is in good agreement for position and intensity. The experiment presents a slightly shifted raise due to the 2 mm nozzle lip axial shift reported in Section 5.3 and due to the higher velocities. As described before, Cosmic predicts the first shock more upstream so that the minimum velocity is reached at $x \approx 0.0D_p$, while *elsA* and the experiment place the first shock downstream of the primary nozzle exit plane. Following the first shock, Cosmic predicts a less intense and more upstream expansion followed by a more modest recompression of the flow. The same features are predicted by *elsA* and are shown in the experiment, but these are larger and more intense. The differences observed between $-0.1D_p < x < 0.8D_p$ generate the spatial phase shift that is maintained in the axial Mach number distribution throughout the secondary jet potential core. The number, spacing, and intensity of the shock cells developing from $x = 1D_p$ predicted by the two solvers are in good agreement, as shown in Tables 5.1 and 5.2,

5. SUPERSONIC UNDER-EXPANDED DUAL-STREAM JET

confirming a good spatial discretisation of the domain in the axial direction. The numbering of the shock cells in the tables ignores the non-periodic structures up to $x = 1D_p$. The experiment presents larger shock-cell structures, being 25% larger on average for the first 5 shock cells, and higher Mach numbers than the numerical results. The potential core decay is in good agreement between the two simulations, while it occurs further downstream by around $2D_p$ in the experiment.

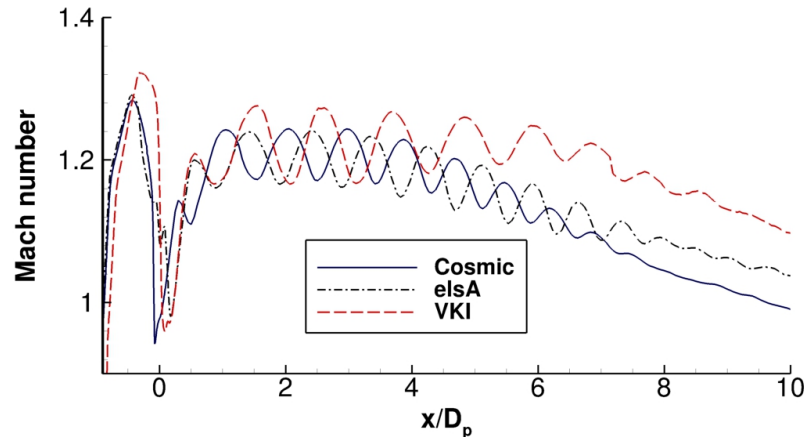


Figure 5.7: Time-averaged Mach number distribution through the middle of the secondary jet. Comparison between Cosmic, *elsA* [100], and experimental results from VKI [105].

The secondary jet shock-cell structure axial shift in the Cosmic predictions affects the primary jet Mach number distribution. The primary jet, which is subsonic, exhibits a pattern of compressions and expansions that alternate in the axial direction that mirrors the shock cell pattern on the secondary jet that surrounds it. This modulates the primary jet cross-section in the axial direction. In Fig. 5.8 it is possible to observe spatial oscillations in the Mach number axial distribution of the primary jet which are in phase with the secondary jet shock cells. An expansion of the supersonic secondary flow causes a local increase in the supersonic secondary flow cross-section. This is accommodated by both an outwards displacement of the

5. SUPERSONIC UNDER-EXPANDED DUAL-STREAM JET

	Cosmic	<i>elsA</i>	% error ₁	Exp. VKI	% error ₂
L_1/D_p	1.013	0.998	1.5%	1.035	-2.2%
L_2/D_p	0.924	0.938	-1.5%	1.116	-20.8%
L_3/D_p	0.880	0.894	-1.6%	1.153	-31.0%
L_4/D_p	0.821	0.857	-4.4%	1.079	-31.4%
L_5/D_p	0.784	0.805	-2.7%	0.939	-19.7%
L_{avg}/D_p	0.884	0.898	-1.6%	1.064	-25.1%

Table 5.1: Shock-cell axial length. Error₁ refers to discrepancy between Cosmic and *elsA* [100], error₂ refers to discrepancy between Cosmic and the VKI experiment [105].

	Cosmic	<i>elsA</i>	% error ₁	Exp. VKI	% error ₂
M_1	1.242	1.239	0.2%	1.276	-2.7%
M_2	1.243	1.241	0.2%	1.272	-2.3%
M_3	1.244	1.233	0.9%	1.267	-1.8%
M_4	1.230	1.219	0.9%	1.260	-2.4%
M_5	1.204	1.192	1.0%	1.248	-3.6%
M_{avg}	1.232	1.225	0.6%	1.265	-2.7%

Table 5.2: Shock-cell amplitude. Error₁ refers to discrepancy between Cosmic and *elsA* [100], error₂ refers to discrepancy between Cosmic and the VKI experiment [105].

secondary nozzle outer shear layer as well as by the narrowing of the primary jet cross-section. Being the primary flow subsonic, a reduction of the jet cross-section causes an expansion of the flow which accelerates. Figure 5.8 shows that, in the predictions of Cosmic, the alternating axial pattern of local accelerations and decelerations, shown by a wavy trend in the Mach number distribution, is phase-shifted upstream compared to the predictions from *elsA* and to the experiment by VKI, similarly to the results reported in Fig. 5.7. As for the axial Mach number distribution of the secondary jet, the amplitude of the accelerations and decelerations is

5. SUPERSONIC UNDER-EXPANDED DUAL-STREAM JET

broadly consistent between the numerical predictions. The amplitude of the Mach number spatial fluctuations is larger in experiment, as in Fig. 5.7. There is a fair agreement in the wavelength and in the number of waves between experiment and computation.

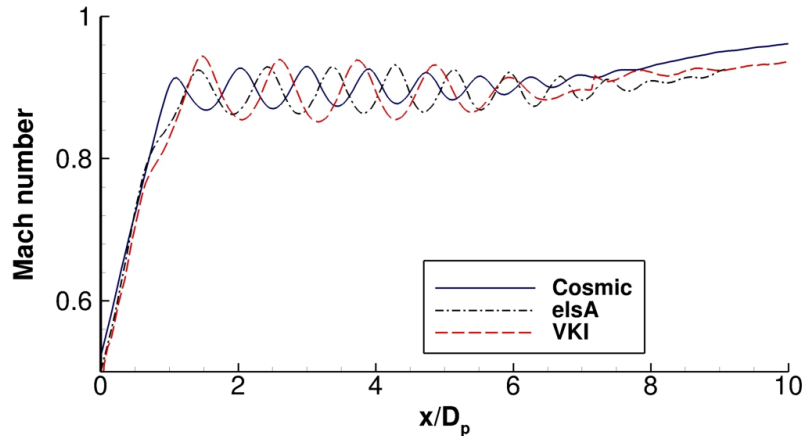


Figure 5.8: Time-averaged Mach number distribution along the centreline of the primary jet. Comparison between Cosmic, *elsA* [100], and experimental results from VKI [105].

To investigate the causes of the shock-cell structure axial shift and to investigate whether this numerical artefact might come from the RANS approach used by the DES in the boundary layer over the primary nozzle wall, the time-averaged Mach number distribution from Cosmic of Fig. 5.7 is compared to that from a pure RANS simulation performed with *elsA*. In Fig. 5.9 it is possible to observe that a much closer match is obtained in the predicted location of the first shock on top of the primary nozzle exit plane. Figure 5.9 suggests that the flow topology of the DES simulation is closer to that from a RANS simulation in the supersonic region over the primary nozzle external wall. This result seems to confirm that the RANS boundary layer modelled in Cosmic strongly affects the flow topology over the first one and a half diameters downstream of the secondary nozzle exit plane. The comparison

5. SUPERSONIC UNDER-EXPANDED DUAL-STREAM JET

of the primary jet axial Mach number distributions from the time-averaged Cosmic simulation and from the *elsA* RANS simulation is presented in Fig. 5.10. It shows an improved agreement in the spatial phase of the first acceleration downstream of the nozzle exit plane compared to Fig. 5.8. This confirms the interpretation that the alternating axial pattern of accelerations and decelerations in the primary jet are mainly driven by the changes in the radial confinement of this jet by the secondary jet shock cells.

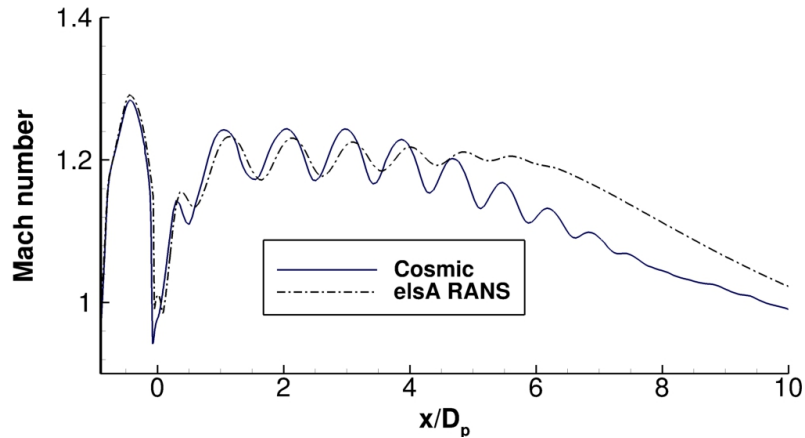


Figure 5.9: Time-averaged Mach number distribution through the middle of the secondary jet. Comparison between time-averaged Cosmic predictions and RANS predictions from *elsA* [100].

Despite the clear shift and difference in flow topology in the first D_p , the axial Mach number distribution of Fig. 5.7, as well as Tables 5.1 and 5.2, show that the spacing and intensity of the shocks are well predicted by Cosmic. To confirm these observations, the radial distribution of the time-averaged Mach number is extracted for the first 6 shock cells and it is shown in Fig. 5.11. The extraction is performed at different axial locations for the three sets of data to take into account the different position of the shocks among the numerical predictions and the experiment. The upper part of the figure shows the radial Mach number distribution for the position

5. SUPERSONIC UNDER-EXPANDED DUAL-STREAM JET

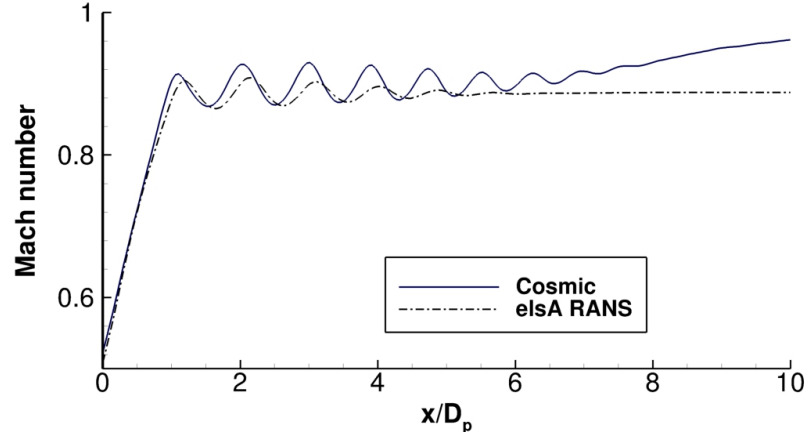


Figure 5.10: Time-averaged Mach number distribution along the centreline of the primary jet. Comparison between time-averaged Cosmic predictions and RANS predictions from *elsA* [100].

of lowest pressure in the shock cells, *i.e.* of local Mach number maximum, while the lower part displays the Mach number radial distribution at the location of maximum pressure of the same shock cells, *i.e.* of local Mach number minimum. The same layout is later adopted for the figures displaying the radial distributions of time-averaged radial velocity u_r , of axial velocity variance u' , and of radial velocity variance u'_r . Figure 5.11 displays a good agreement in the Mach number radial distributions from Cosmic and *elsA* over the first 6 shock cells. The experimental data show higher Mach number local maxima after the third shock cell and cells that are radially larger, with a thinner shear layer with respect to the numerical simulations. Both Cosmic and *elsA* predict larger shear layer visual thicknesses than in experiment, with the Cosmic prediction being closer to the experimental results. The shear layer predicted by Cosmic and *elsA* is on average 25% and 40% larger than in experiments respectively. The different radial shape and a larger shear layer can account for the shorter shock-cell lengths predicted by the numerical simulations. In the radial direction, Cosmic and *elsA* predict cells that are 16% smaller than in the

5. SUPERSONIC UNDER-EXPANDED DUAL-STREAM JET

experiments. With less space in the radial direction, the expansion and compression waves travel over shorter distances in the axial direction, which results in smaller shock-cell lengths. Moreover, with a reduced Mach number gradient across the shear layer, waves interacting with the shear layer are damped and lose intensity.

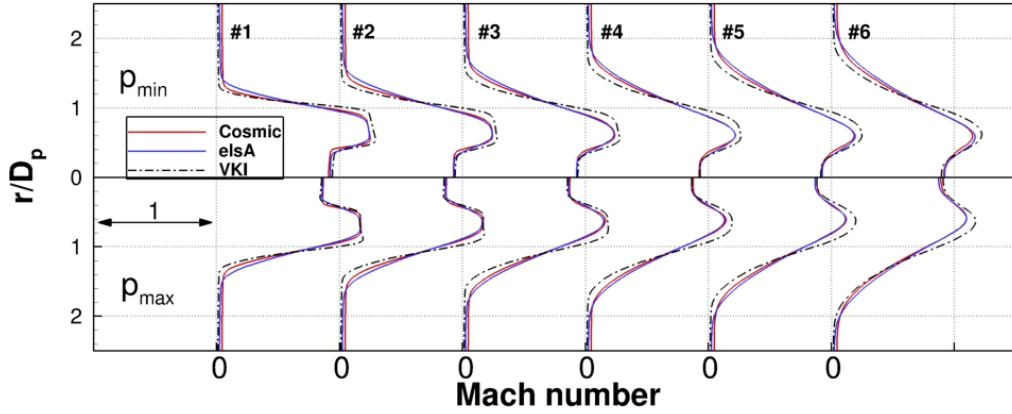


Figure 5.11: Time-averaged Mach number radial distributions. Comparison between Cosmic, *elsA* [100], and experimental results from VKI [105].

An interesting insight into the flow field is given by the contour plot of the radial velocity fields shown in Fig. 5.12. In Fig. 5.12, a negative u_r indicates that the flow is directed towards the jet axis, while a positive u_r implies an opening of the jet in the opposite direction. The radial velocity shows the typical behaviour of not-perfectly expanded jets along the outer nozzle lip line, with regions of expanding flow going outwards, denoted by a positive u_r , alternating with re-compressions of the flow that turns towards the jet axis. The axial portion of the secondary jet that develops over the primary jet nozzle wall has a strong negative component that is directed towards the jet axis, despite the strong expansion fan generated at the nozzle lip, due to the geometry of the nozzle. After the primary and secondary jets meet at the primary nozzle exit plane, the radial velocity component goes to zero as the

5. SUPERSONIC UNDER-EXPANDED DUAL-STREAM JET

secondary stream jet is turned in the axial direction by the expansion fan that follows the first shock stemming from the primary nozzle lip. This is followed by triangle-shaped regions of high radial velocity in the secondary jet shear layer. These regions are located where the shock waves reach the outer nozzle shear layer and reflect as expansion fans. At these locations, the flow turns outwards with respect to the jet axis and the potential core expands in the radial direction. Where an expansion fan is reflected as compression waves by the inner shear layer, it goes back interacting with the outer shear layer, tilting the flow back towards the coaxial nozzle axis. The flow field comparisons in Fig. 5.12 show a good agreement between the numerical predictions in terms of the types of the flow patterns that are modelled and of the radial velocity ranges that are predicted. Higher values of u_r are observed in the corresponding experiment by Guariglia [105] in each expansion zone and markedly higher values of u_r occur in the experiment in the shear layer downstream of the axial position $x = 7D_p$ due to the expansion of the jet.

Observing the radial distributions of the time-averaged radial velocity of the first, third, and fifth shock cell in Fig. 5.13, a more detailed analysis is possible. The radial velocity is normalised with respect to $u_{r\ max} = 7\ \text{m/s}$. Both Cosmic and *elsA* predict larger radial velocity minima just outside the shear layer shed by the outer nozzle lip line. This peak represents the flow entrainment from the surroundings towards the jet and it is overestimated in both numerical simulations. In the experiment, lower flow entrainment suggested by the radial velocity distribution is probably due to recirculation effects linked to the FAST test facility, or to the geometry of the part of the nozzle that is not simulated, which may be a source of blockage. The difference in the radial velocity minima is 50% in the first shock cell and this difference reduces in the third and fifth shock cells. Cosmic predicts the radial velocity minimum closer

5. SUPERSONIC UNDER-EXPANDED DUAL-STREAM JET

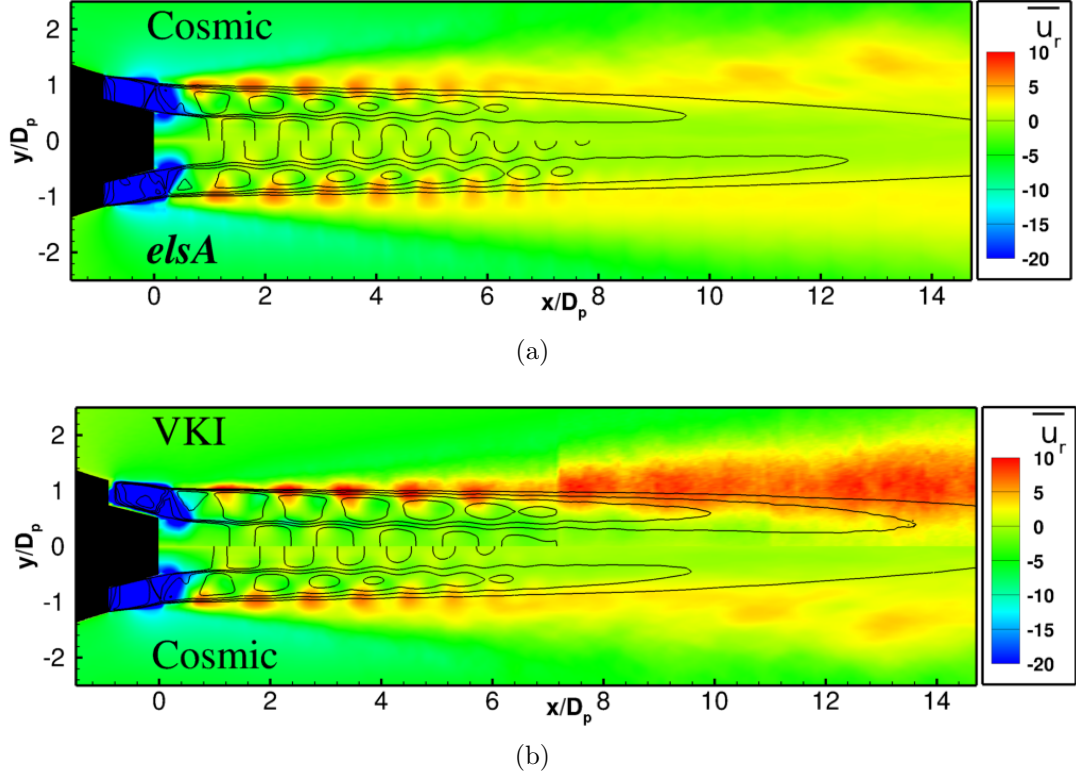


Figure 5.12: Time-averaged radial velocity contours. Comparison between a) Cosmic and *elsA* [100] and b) Cosmic and experimental results from VKI [105]. Velocity is stated in m/s.

to the jet axis, confirming a thinner shear layer than in *elsA*. Radial velocity maxima occur at around $r = 1D_p$. These maxima are determined, as already described, by the expansion fan of the shock cells. The radial velocity maxima predicted by Cosmic and *elsA* are in good agreement both in position and intensity for all cells. The experimental data, on the other hand, show higher radial velocity maxima, even if their radial position is matched in the numerical simulations. For radial distances below $r = 1D_p$, the agreement in the radial distribution of radial velocity among experiment and predictions is coarser, in particular in the first and third shock cells. The agreement among the numerical simulations improves in the fifth shock cell.

5. SUPERSONIC UNDER-EXPANDED DUAL-STREAM JET

The negative values of radial velocity observed closer to the jet axis are associated to the primary nozzle shear layer which converges towards the jet axis due to the radial expansion of the secondary jet indicated by the radial velocity maximum along the outer shear layer discussed in the context of Fig. 5.12. Both numerical methods are shown in Fig. 5.13 to predict the radial velocity component as zero at the axis of the jet, while the experimental data show a non-zero value at the jet axis, which was not expected. The slightly negative component might be explained by a misalignment of the laser sheet or of the nozzle axis during measurement, or to a less extent by the uncertainty linked to the number of averaging samples, which was limited to 3,000 samples. The limitation in averaging is also likely to be responsible for less smooth velocity profiles with respect to the predictions, as it can be observed in the radial distributions of radial velocity at the end of the fifth shock cell in Fig. 5.13. The contour plots and the distribution lines predicted by Cosmic and *elsA* are obtained by ensemble averaging the time averaged data over sixteen different azimuthal planes.

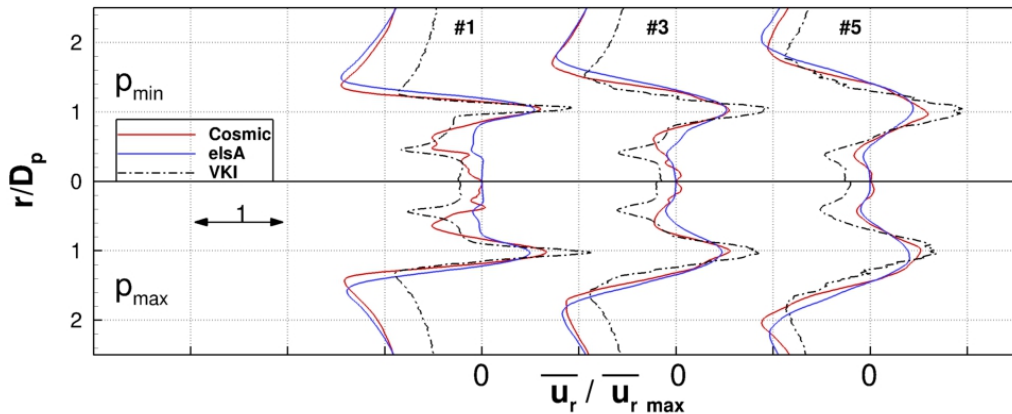


Figure 5.13: Radial distribution of the time-averaged radial velocity of the first, third, and fifth shock cells. Comparison between Cosmic, *elsA* [100], and experimental results from VKI [105].

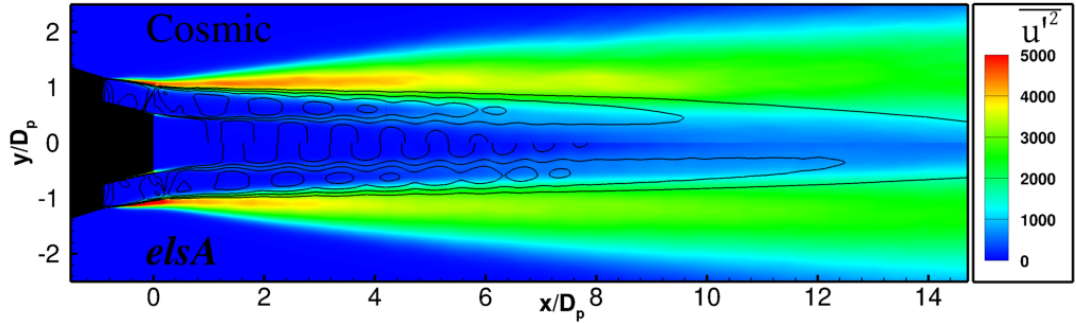
5. SUPERSONIC UNDER-EXPANDED DUAL-STREAM JET

In Fig. 5.14, contours of the variance of u' , the axial velocity fluctuation, are shown from Cosmic, **elsA**, and the experimental data. The Cosmic prediction shows higher values of resolved axial velocity fluctuation magnitude in the secondary shear layer at $x > 0.5D_p$ compared to **elsA** and $\overline{u'^2}$ is higher than in experiments up to $x = 7D_p$. Further downstream, the experimental data then show higher values of $\overline{u'^2}$ than both numerical simulations. These observations are confirmed by the distributions in Fig. 5.15 where the radial distribution of $\overline{u'^2}$ is shown. In these plots, $\overline{u'^2}$ is shown normalised by its maximum value in experiment. The maxima in $\overline{u'^2}$ predicted by Cosmic are higher than their experimental counterpart up to the sixth shock cell for the shock-centre distributions. The axial velocity variance observed in the experiments is as low as 50% with respect to both numerical predictions in the first shock cells. This might be explained by the poor resolution of the PIV technique in the thinnest regions of the shear layer [113, 114].

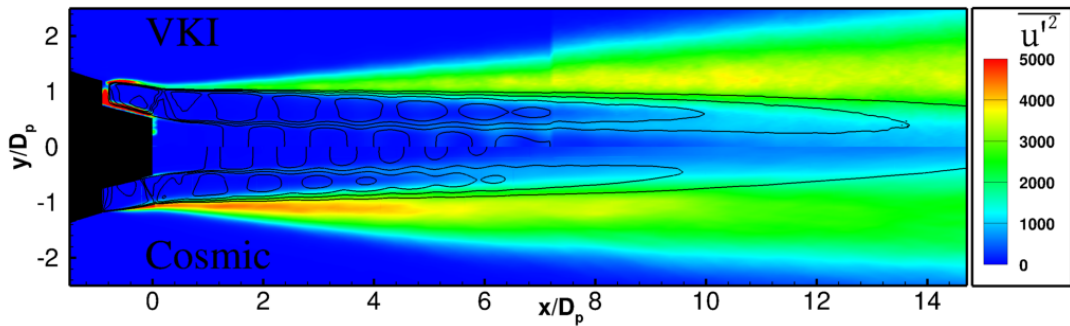
Similar observations can be made comparing experimental and numerical data for the radial velocity variance contours in Fig. 5.16 and for its radial distributions of Fig. 5.17. In Fig. 5.17, $\overline{u_r'^2}$ is normalised by its maximum value in experiment. The experimental levels of $\overline{u_r'^2}$ are about 2.5 times lower than in the numerical predictions for the first shock cell, with this discrepancy reducing in the downstream direction. The contour plot and the distribution lines predicted by Cosmic are obtained by ensemble averaging the time averaged data over four different azimuthal planes.

To conclude the presentation of the time-averaged results, the axial profiles of *rms* axial and radial velocity are shown along the lip lines of the primary and secondary nozzles, respectively in Figures 5.18 and 5.19. There is a fair qualitative agreement between the numerical predictions by **elsA** and by Cosmic in all four plots of Figs. 5.18 and 5.19. Cosmic is shown to estimate higher values of both

5. SUPERSONIC UNDER-EXPANDED DUAL-STREAM JET



(a)



(b)

Figure 5.14: Variance of the axial velocity u' in m^2/s^2 . Comparison between a) Cosmic and *elsA* [100] and b) Cosmic and the experimental results from VKI [105].

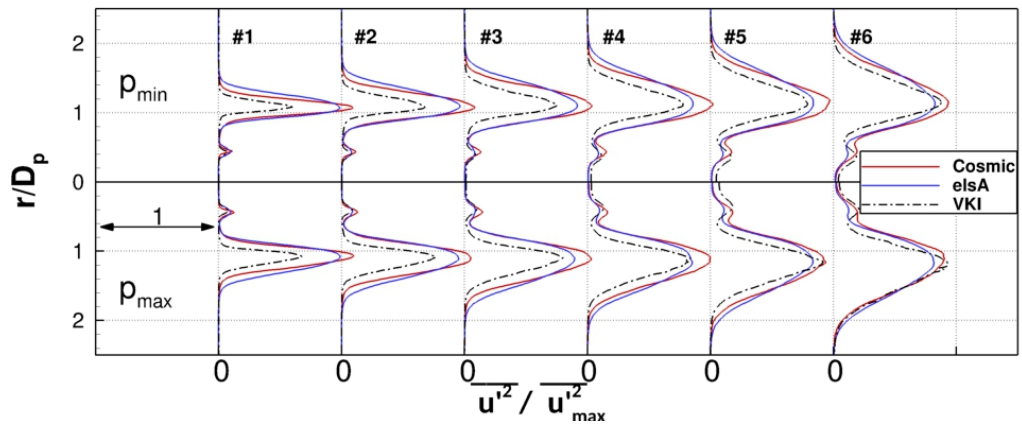
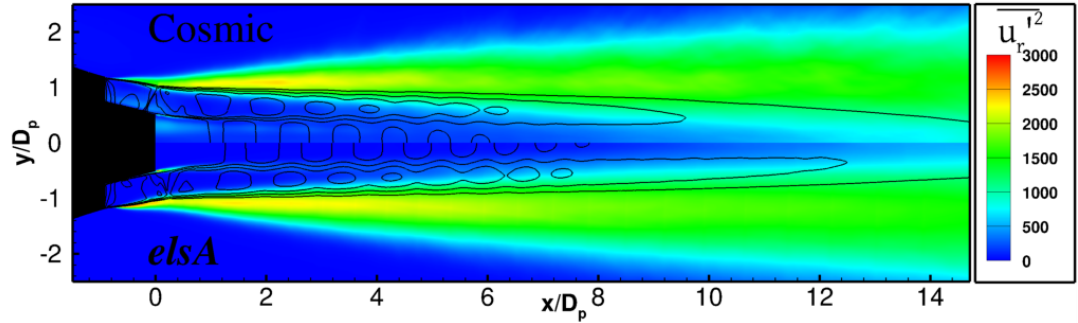
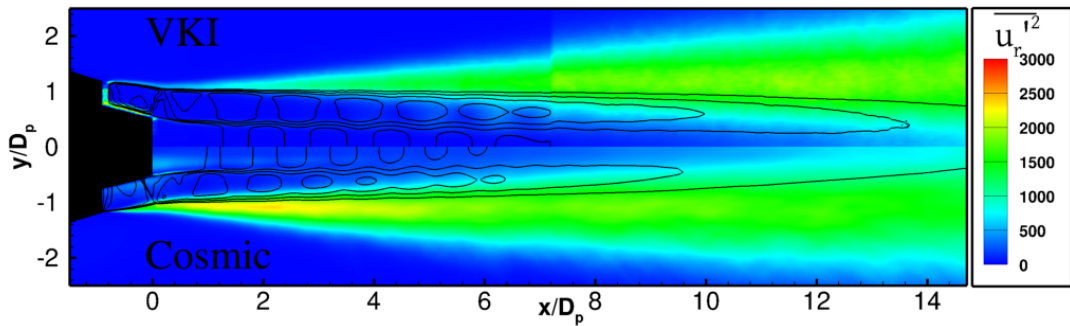


Figure 5.15: Variance of the axial velocity u' radial distribution at corresponding shock cell locations. Comparison between Cosmic, *elsA* [100], and experimental results from VKI [105].

5. SUPERSONIC UNDER-EXPANDED DUAL-STREAM JET



(a)



(b)

Figure 5.16: Variance of the radial velocity u_r in m^2/s^2 . Comparison between a) Cosmic and *elsA* [100] and b) Cosmic and the experimental results from VKI [105].

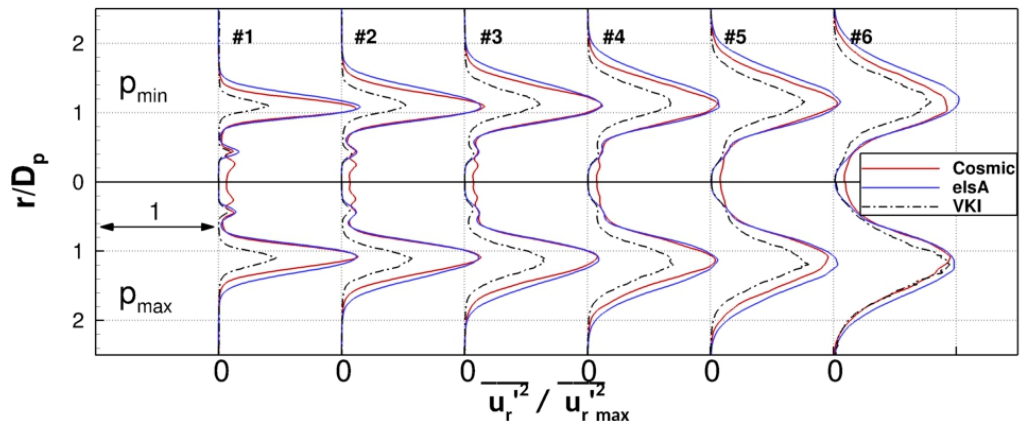


Figure 5.17: Variance of the radial velocity v'^2 radial distribution at corresponding shock cell locations. Comparison between Cosmic, *elsA* [100], and experimental results from VKI [105].

5. SUPERSONIC UNDER-EXPANDED DUAL-STREAM JET

axial and radial *rms* velocity fluctuations at $x > 6D_p$ along the primary nozzle lip line, compared to *elsA*. Whereas this confers to the Cosmic predictions an improved agreement with experiment in Fig. 5.18(a) compared to *elsA*, a coarser agreement is shown in Fig. 5.18(b) at $x > 6D_p$. Along the secondary nozzle lip line, on the other hand, differences between experiment and computation are noticeable for $x < 5D_p$ and $x < 7D_p$ for the axial and radial *rms* velocity distributions respectively. The experiments show an initial decrease of *rms* velocity over the range $-0.9D_p < x < 0D_p$, followed by a first sudden rise and then a steady increase up to a plateau where experimental and numerical *rms* velocity magnitudes are broadly similar. Both numerical predictions show a different trend, characterised by a sharp rise in *rms* velocity up to about $0D_p$ and then a monotonic decline in *rms* velocity with increasing axial distance. A similar monotonic decay of the *rms* axial velocity component is displayed in PIV measurements of the *rms* axial velocity by Krotapalli *et al.* [115] from a fully expanded Mach 1.44 single jet at $Re = 2.3 \times 10^5$. The authors highlighted the challenge of dealing with particle lag as well as of finding an appropriate inter-frame PIV setting in regions of large velocity change. This may explain the inconsistency in trend between the predictions and the experiment from VKI.

The analysis of the averaged quantities presented in this section showed broadly a good agreement with numerical and experimental data. The limitations observed in the single jet simulation were successfully solved and this builds up confidence that time-dependent predictions extracted from probes and planes inside the domain can provide aerodynamic data that is appropriate for studying broad-band shock-associated noise generation in the dual-stream jet. The impact on the jet of the secondary nozzle axial shift experienced in the VKI experiment is addressed in

5. SUPERSONIC UNDER-EXPANDED DUAL-STREAM JET

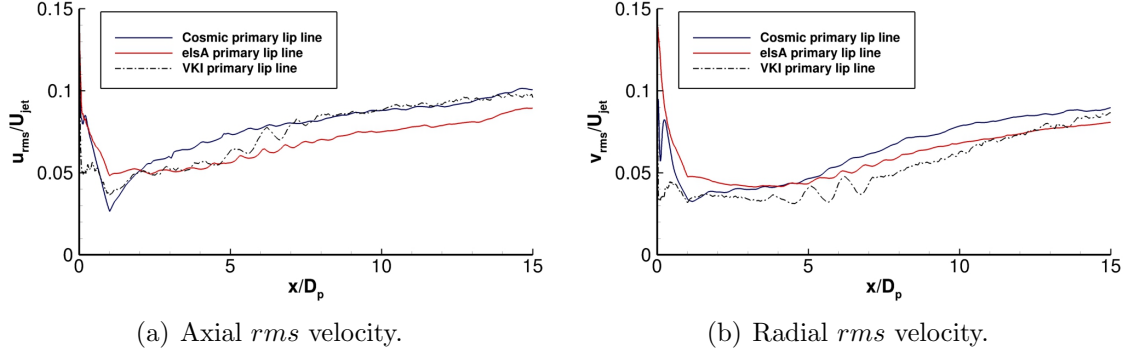


Figure 5.18: *Rms* velocity profiles on the primary nozzle lip line for an under-expanded coaxial jet. Comparison between Cosmic, *elsA* [100], and experimental results from VKI [105].

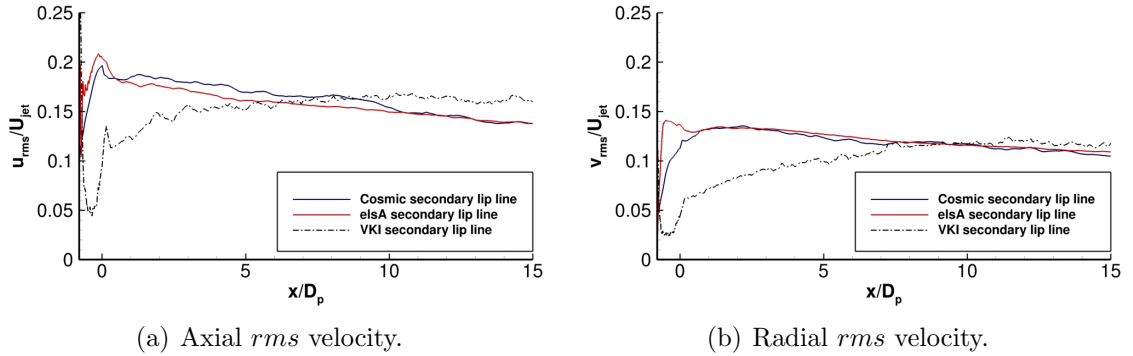


Figure 5.19: *Rms* velocity profiles on the secondary nozzle lip line for an under-expanded coaxial jet. Comparison between Cosmic, *elsA* [100], and experimental results from VKI [105].

Section 5.4.2.

5.4.2 Effects of secondary nozzle shift in VKI experiments

As previously stated, the secondary nozzle of the experimental apparatus experienced an axial shift of about 2 mm during the blow-down tests due to the pressurisation of the air delivery duct. In his Ph.D. thesis, Pérez-Arroyo [100] performed a comparative analysis of the designed and shifted nozzles through RANS simulations.

5. SUPERSONIC UNDER-EXPANDED DUAL-STREAM JET

A brief summary of his results is here given.

The experimental facility experienced a shift of the secondary nozzle exit plane of 1.9 mm in the downstream direction. Considering the reduced dimensions of the experimental nozzle with respect to the one adopted in the numerical simulations, an axial shift of the secondary nozzle of $0.117 D_p$ was modelled in the RANS simulation. Due to the shape of the coaxial nozzles, the shift of the secondary nozzle translates into an increase of the effective area for the secondary flow of 5%, from $A/D_p^2 = 2.63$ to $A/D_p^2 = 2.76$. This causes an increase in the mass flow rate of 5% through the secondary nozzle, assuming a negligible change in the jet outflow specific momentum ρu .

The time-averaged Mach number contours extracted from the RANS simulations shown in Fig. 5.20 show that the $0.117D_p$ change in the secondary nozzle axial position determines some differences in the flow topology between the two configurations. The secondary nozzle as designed, shown in Fig. 5.20(a), produces a stronger expansion over the primary nozzle wall and the first shock position is upstream with respect to the secondary nozzle shifted as in the experiment, which also has a more regular shock cell structure and more localised compressions and expansions in the first shock cell. The first shock cell is then followed by a marginally stronger expansion in the case of the secondary nozzle shifted as in the experiment shown in Fig. 5.20(b).

Figure 5.21 shows the Mach number distributions through the middle of the secondary nozzle as designed and the secondary nozzle as shifted as in the experiment. Figure 5.21 shows how the axial shift in the secondary nozzle plane directly translates into a shift of the shock-cell train in the positive axial direction. The axial shift of the shock cell around $x = 1D_p$, as determined by the axial location of the Mach

5. SUPERSONIC UNDER-EXPANDED DUAL-STREAM JET

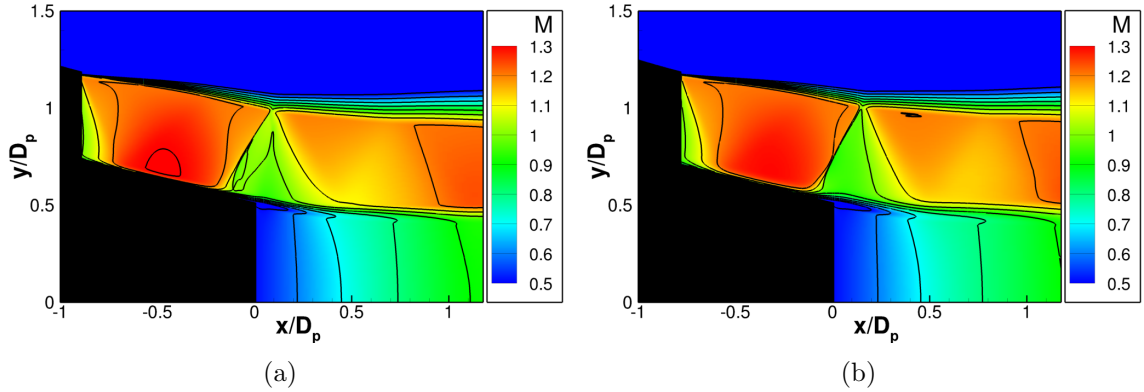


Figure 5.20: Time-averaged Mach number contours. Comparison between a) the secondary nozzle as designed and b) the secondary nozzle shifted axially by $0.117D_p$ as in experiment. RANS simulations obtained with the *elsA* [100] solver.

number local maximum in Fig. 5.21, is $\Delta x = 0.148D_p$. The difference in the shock cell axial location between the two flows then increases with increasing axial distance for the following shock cells due to an increase in the shock-cell length as reported in Table 5.3. Another noticeable effect is the increase in the shock cell intensity, with a Mach number drop across the shocks that increases on average by 15.4% for the first 3 shock cells downstream of the primary nozzle exit plane, as shown in Table 5.4. The same effect is observed for the first shock above the primary nozzle wall, with a drop in Mach number that goes from $\Delta M = 0.301$ to $\Delta M = 0.356$ with an increase of 18.3%. The primary jet Mach number axial distribution shown in Fig. 5.22 is likewise affected by the displacement of the secondary nozzle shock cell train in the positive axial direction, shown in Fig. 5.21. The Mach number oscillations translate axially in space by approximately the same Δx as the secondary shock cells and their amplitude increases by approximately 28%.

The changes in flow topology and velocity modulation here described are likely to have an impact on the noise produced by the dual-stream jet. However, the

5. SUPERSONIC UNDER-EXPANDED DUAL-STREAM JET

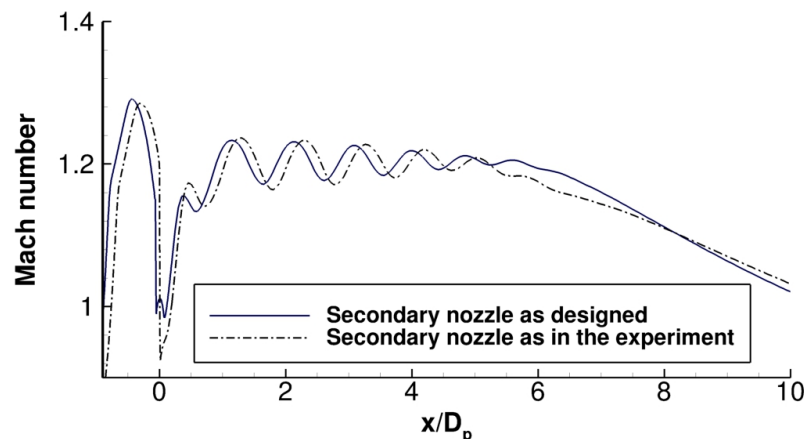


Figure 5.21: Time-averaged Mach number distribution through the middle of the secondary jet. Comparison between the secondary nozzle as designed and the secondary nozzle as in the experiment by VKI. RANS simulations obtained with the *elsA* [100] solver.

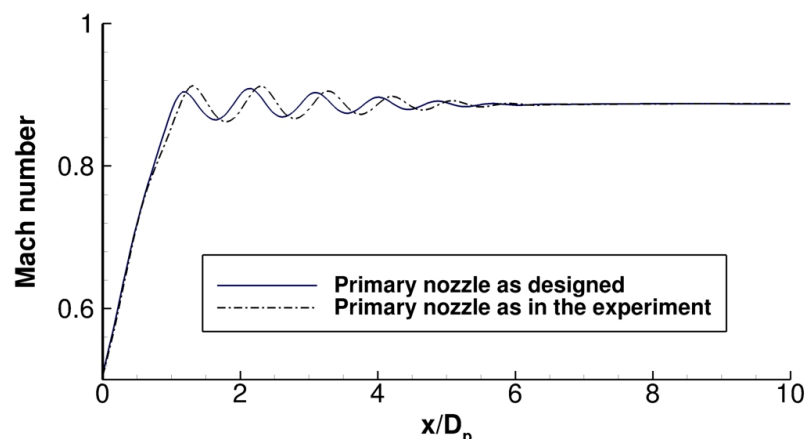


Figure 5.22: Time-averaged Mach number distribution along the centreline the primary jet. Comparison between the secondary nozzle as designed and the secondary nozzle as in the experiment by VKI. RANS simulations obtained with the *elsA* [100] solver.

nature and magnitude of such impact remain unclear and they should be the focus of dedicated studies in the future.

5. SUPERSONIC UNDER-EXPANDED DUAL-STREAM JET

Secondary nozzle	as designed	as tested in experi- ment	% increase
L_1/D_e	0.995	1.014	1.9%
L_2/D_e	0.959	0.977	1.9%
L_3/D_e	0.903	0.931	3.1%
L_{avg}/D_e	0.952	0.974	2.3%

Table 5.3: Shock cell axial length. Comparison between RANS simulations from *elsA* with the secondary nozzle as designed and as tested in experiment [105].

Secondary nozzle	as designed	as tested in experi- ment	% increase
ΔM_1	0.061	0.072	18.0%
ΔM_2	0.054	0.062	14.8%
ΔM_3	0.042	0.046	9.5%
ΔM_{avg}	0.052	0.060	15.4%

Table 5.4: Mach number drop across the first three shocks of the secondary jet shock-cell train. Comparison between RANS simulations from *elsA* with the secondary nozzle as designed and as tested in experiment [105].

5.4.3 Unsteady flow and noise production

This section presents unsteady flow results and discusses the noise production for the dual jet test case. Figure 5.23 shows a snapshot taken from the Cosmic DES simulation. The instantaneous Mach number distribution is shown by iso-colour levels and the pressure field fluctuations are shown by different levels of gray. The pressure field fluctuation is shown as the percentage of the ambient pressure. The key features of a typical dual-stream jet with a secondary stream supersonic and under-expanded can be clearly identified, with triangle-shaped shock cells strongly interacting with

5. SUPERSONIC UNDER-EXPANDED DUAL-STREAM JET

turbulent structures being convected downstream in the dual-stream mixing layers. Pressure waves are visible and appear to be travelling in both the upstream and downstream directions, indicating that shock-cell noise (SCN) is generated by the jet.

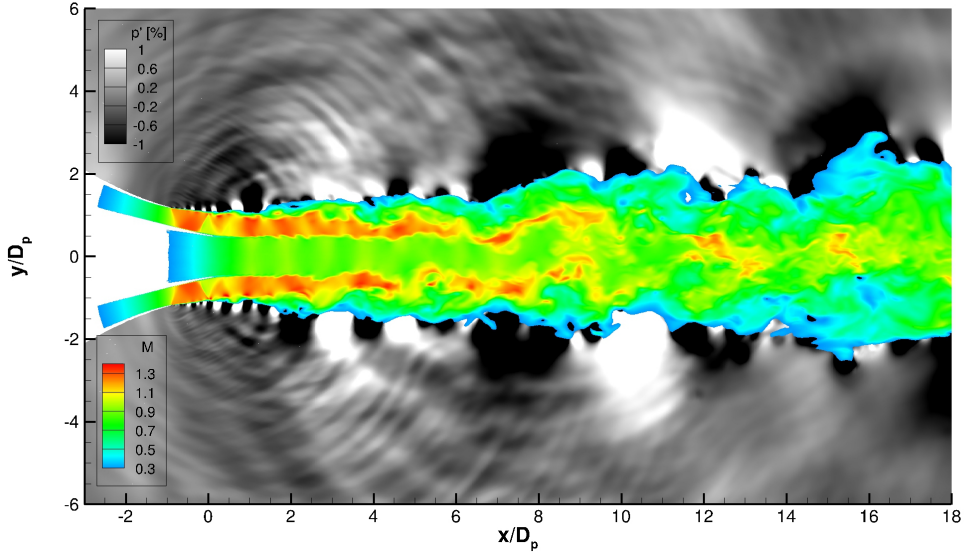


Figure 5.23: Instantaneous iso-colour levels of streamwise Mach number and grayscale levels of pressure fluctuation of the under-expanded coaxial jet.

In Fig. 5.24, the Power Spectral Density (PSD) in the near field of the jet is shown. Figures 5.24(a,d), 5.24(b,e), and 5.24(c,f) show respectively the PSD from the predicted pressure fluctuations at radial locations $r = 2D_p$, $3D_p$, and $4D_p$ on the meridional plane ($\theta = 0$) from Cosmic and *elsA*. The PSD is expressed as dB/St and it is plotted as function of the normalised axial location x/D_p and of the Strouhal number $St = f D_p / c_{ref}$. The first row of results has been obtained with the numerical scheme Cosmic, while the second one is the output from *elsA*. The spatial resolution of the abscissa in Fig. 5.24 is $\Delta x = 0.1D_p$. From Fig. 5.24 it is possible to observe a good qualitative match of results between the numerical schemes. The low

5. SUPERSONIC UNDER-EXPANDED DUAL-STREAM JET

Strouhal number components that were over-estimated in Cosmic in the single jet simulation appear now to be more comparable in magnitude to the predictions from *elsA*, with a decay in the radial direction that now matches that from the *elsA* prediction. The jet modelled by *elsA* appears to exhibit slightly larger amplitude pressure fluctuations than the prediction from Cosmic for all locations and Strouhal numbers, in particular for $St > 1.0$. Analysing Fig. 5.24 with respect to results presented by Savarese [107] for an under-expanded single jet test case, it is possible to observe the ‘banana’ shaped component of noise over the range $0.4 < St < 1.1$, which is typical of broad-band shock associated noise (BBSAN). In the Cosmic prediction, this component extends from $St = 0.4$ to $St = 1.1$ and from $x = 0D_p$ to $x = 7D_p$. In *elsA* the BBSAN ‘banana’ has a larger extent, covering the same Strouhal number range, but spanning from $x = 0D_p$ to $x = 9D_p$. The axial extent of the ‘banana’ is proportional to that of the shock train structure, being shorter for the Cosmic prediction than for *elsA* prediction, showing the clear dependence of these frequency components upon the shock cells. The agreement in shape and intensity of the PSD plots from the two numerical methods is good and it suggests that the DES simulation is able to correctly capture the fundamental mechanisms of shock-cell noise generation. To quantitatively compare the PSD plots, an integration of the PSD over the same area of the ‘banana’ region is performed for Cosmic and *elsA*. The integration area extends from $x = 0$, between $St = 0.4$ and $St = 0.7$, to $x = 10D_p$, between $St = 0.7$ and $St = 1.16$, following the ‘banana’ shape. The integration is performed for all three r positions shown in Fig. 5.24 and shows a good agreement between Cosmic and *elsA* with a maximum difference of 2.4dB. For the ‘banana’ region Cosmic predicts an integrated PSD of 145.9dB, 143.8dB, and 142.1dB from Fig. 5.24(a-c) respectively, while *elsA* gives an integrated PSD

5. SUPERSONIC UNDER-EXPANDED DUAL-STREAM JET

of 147.7dB, 146.0dB, and 144.5dB from Fig. 5.24(d-f).

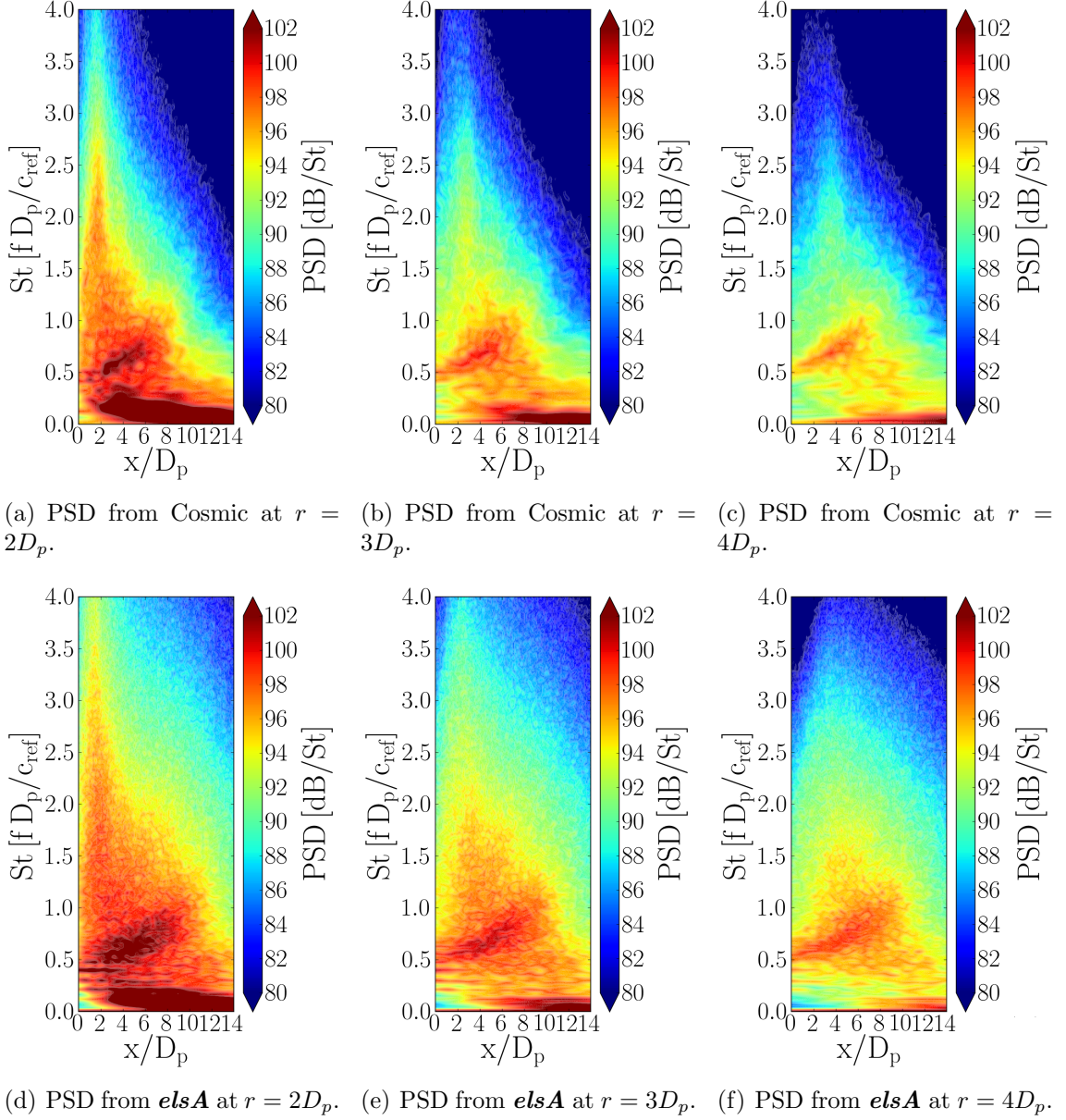


Figure 5.24: Power Spectral Density at different radial locations for an under-expanded coaxial jet obtained with the numerical schemes Cosmic and *elsA*.

The correlation length scales of the axial and radial velocity components are shown in Fig. 5.25(a) and 5.25(b) respectively. These correlation length scales are

5. SUPERSONIC UNDER-EXPANDED DUAL-STREAM JET

obtained by following the same integration procedure used in Chapter 4. The predicted length scale for the axial velocity shows a broad qualitative agreement between the two solvers in the correlation length scale evaluated along the secondary nozzle lip line, with a similar growth rate and comparable levels. Along the primary nozzle lip line, on the other hand, Cosmic predicts a greater axial velocity correlation length of greater growth rate close to the nozzle exit. The axial velocity correlation length predicted by Cosmic along the primary nozzle lip line then exhibits a reduced growth rate downstream of $x = 5D_p$ that is similar to the one from the *elsA* predictions. Due to its earlier growth rate close to the nozzle exit plane, the correlation length scale predicted by Cosmic remains about 25% longer than that from *elsA* at $x > 5D_p$. The radial velocity length scale of Fig. 5.25(b) is smaller than the axial one. Again, Cosmic and *elsA* present a better agreement along the secondary nozzle lip line compared to the radial velocity length scale evaluated along the lip line of the primary nozzle. For all plots, Cosmic shows higher values of correlation length indicating more coherent turbulent structures being convected in the primary and secondary shear layers. This difference, which is shown by Fig. 5.25 to be lower than the corresponding results for a single jet test case of Fig. 4.9, can be ascribed to a higher azimuthal refinement in the *elsA* LES mesh than in the Cosmic DES mesh, as the number of cells in the azimuthal direction used in the *elsA* LES is 256 compared to 128 in the Cosmic DES. However, this difference does not seem to affect the near-field acoustic data as much as noted in Chapter 4, as it is possible to observe comparing the low Strouhal number components of near-field PSD plots between Fig. 4.7 and Fig. 5.24.

Figure 5.26 presents the PSD predicted at a far field array placed at $R = 70D_p$ from the jet axis. These results have been obtained by means of the Ffowcs Williams

5. SUPERSONIC UNDER-EXPANDED DUAL-STREAM JET

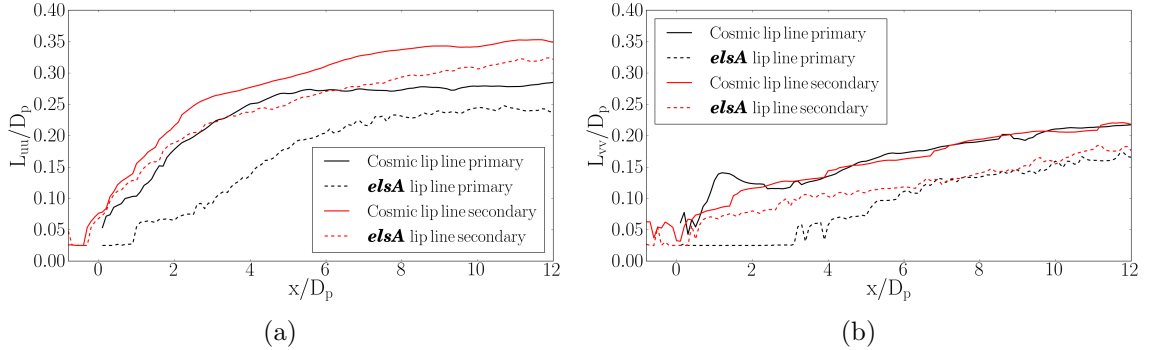


Figure 5.25: Axial variation of the correlation lengths of the resolved (a) axial and (b) radial velocities along the lip lines of the primary and of the secondary nozzles. Coaxial jet modelled by Cosmic DES and by *elsA* LES [100].

and Hawkings acoustic analogy applied on bespoke surfaces as shown in Figure 5.1. These predictions are compared with the corresponding results from *elsA* and from microphone measurements performed at VKI [105]. These results are of difficult interpretation due to major differences at different angles and at different frequencies among the numerical and experimental dataset. At 30° , Fig. 5.26(a), there is good agreement for very low Strouhal numbers between *elsA* and the experiment, while Cosmic predicts PSD levels 6dB higher, showing that at low angles its accuracy for low frequency components is possibly still affected by the limited extent of the computational domain and by the acoustically non-reflecting performance of the boundary conditions. Between $St = 0.3$ and $St = 3$, the numerical predictions show a much improved agreement, while they are above the experimental measurements by about 6dB. At higher Strouhal numbers, all three sets of data converge towards more similar PSD values. At higher angles, Fig. 5.26(b)-5.26(f), the results exhibits a good agreement between numerical data at low Strouhal numbers, up to $St = 0.5$. The agreement between the numerical predictions and the experiment is still coarse, with a difference of about 7dB over the range $0.1 < St < 0.3$ at $\theta = 130^\circ$, as shown in

5. SUPERSONIC UNDER-EXPANDED DUAL-STREAM JET

Fig. 5.26(f). As observed for the single jet test case, Cosmic predicts an exponential decay in the PSD with frequency, which increases with increasing angles. The *elsA* LES predicts a greater PSD roll-off rate with frequency for $St > 3$ at polar angles higher than 30° with respect to the Cosmic DES. The BBSAN spectral peaks from the numerical predictions, perhaps shown most clearly in Fig. 5.26(f), broadly agree in shape and position among the three sets of data, but for the absence of screech tones in the predictions. Experimental BBSAN peaks are of lower PSD but agree in shape, even if a slight shift in frequency is observed. This frequency shift is probably due to the different size of the shock cells between experiment and computation, as highlighted in Table 5.1. Due to the axially longer shock cells observed in the experiments, the BBSAN frequency associated to them is lower with respect to that of the BBSAN extracted numerically by acoustic analogy from the computational fluid dynamics near-field simulations, in which the shock cells are shorter. The shock cell axial length is inversely related to the BBSAN frequency according to the simple phased-array model for BBSAN of Harper-Bourne and Fisher [116].

5. SUPERSONIC UNDER-EXPANDED DUAL-STREAM JET

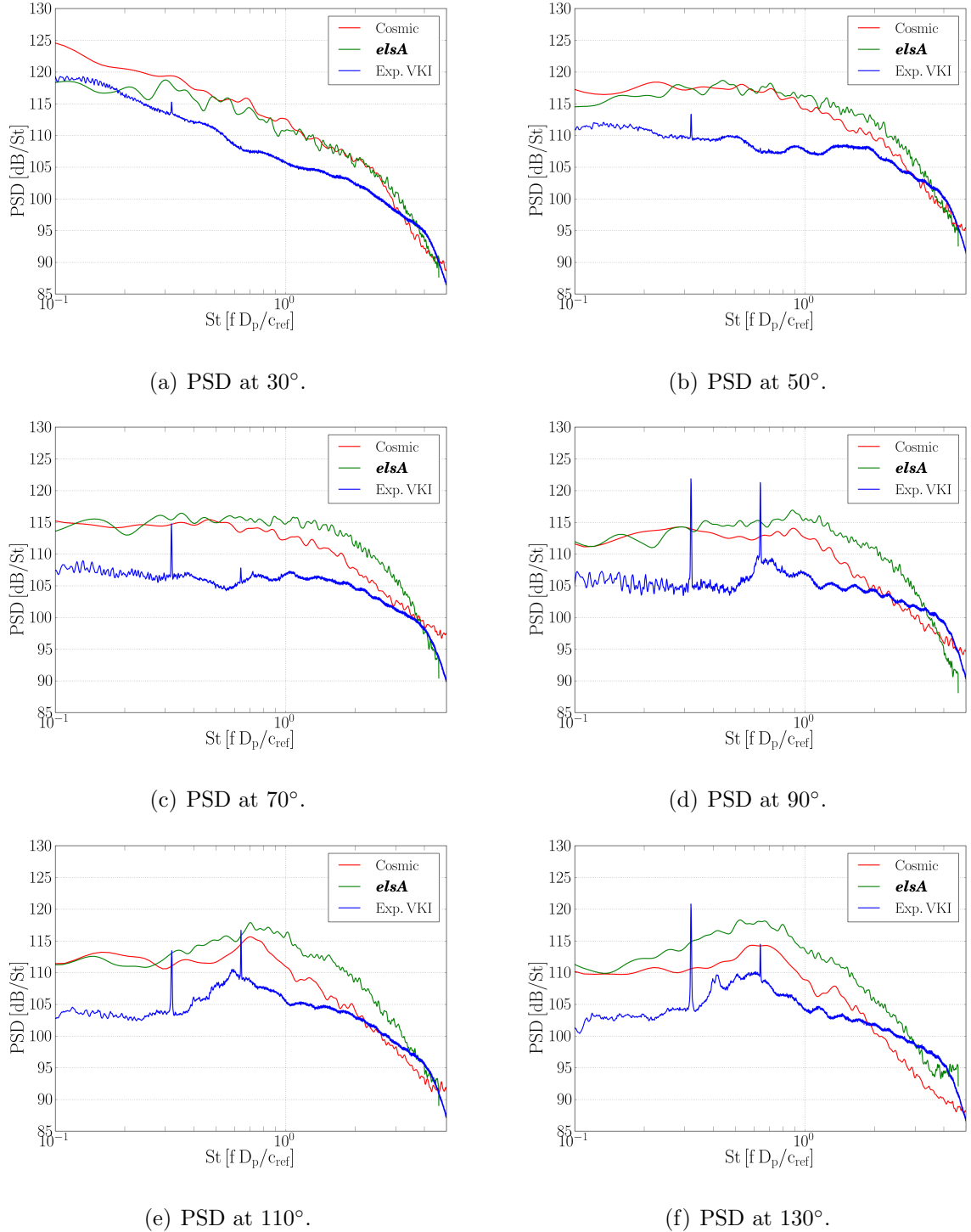


Figure 5.26: Far-field PSD at $R = 70D_p$. Polar angle θ measured with respect to the jet axis. Numerical results from Cosmic and *elsA* [100], experimental results from VKI [105].

5. SUPERSONIC UNDER-EXPANDED DUAL-STREAM JET

By uniformly scaling the numerical predictions by -7dB it is possible to observe how the agreement between the measurements and the predictions from Cosmic at $\theta = 40^\circ$, Fig. 5.27(a), is extremely good up to $St \approx 1$. It is also possible to observe a good match in the exponential decay of the PSD with frequency up to $St = 1.5$. The scaled PSD results at the polar angle $\theta = 130^\circ$ in Fig. 5.27(b) show that both Cosmic and *elsA* predict a steeper PSD roll-off above $St = 1.0$ than the measurements. Over the range $0.2 < St < 1.0$, the three sets of data still display a spread of about 3dB after scaling. The differences in the aerodynamic near-field reported in the previous sections could in part explain this spread. Higher *rms* velocity values predicted by both numerical simulations and the presence of screech in the experiment might also contribute. However, such factors were also present in the single jet test case discussed in Chapter 4, and the differences in far-field noise levels were not as large as the ones reported in this section. The relatively good agreement shown by the two sets of numerical data obtained with completely different and independent solvers suggests that it would be prudent to review the experimental data and its acquisition procedure, with the aim of establishing the experimental uncertainty in these measurements and re-interpret the results in the light of this uncertainty.

The directivity of the dual-stream jet is investigated by computing the Overall Sound Pressure Level (OSPL) at the far-field array set at $R = 70D_p$. The numerical values of OSPL are obtained by integration of the PSD over the Strouhal number range $0 \leq St \leq 5$, from similar data to the one shown in Fig. 5.26. The predictions from the application of the Ffowcs Williams and Hawkings acoustic analogy to the near-field aerodynamic data from Cosmic and *elsA* are compared to the measured sound directivity in Fig. 5.28. It is noticeable that in experiment a lower OSPL was

5. SUPERSONIC UNDER-EXPANDED DUAL-STREAM JET

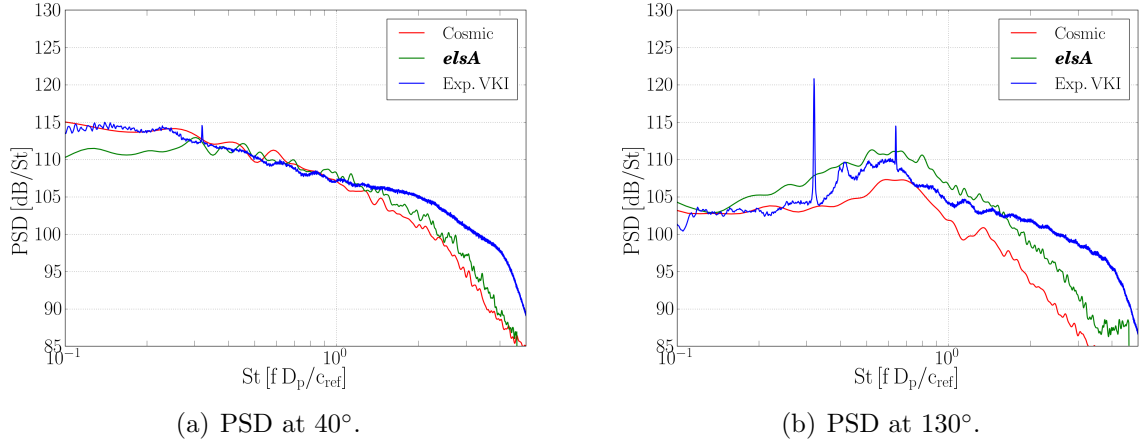


Figure 5.27: Far-field PSD at $R = 70D_p$. Polar angle θ measured with respect to the jet axis. Numerical results from Cosmic and *elsA* [100], experimental results from VKI [105]. The numerical predictions are shown scaled uniformly by -7dB.

measured at all angles with respect to Cosmic and *elsA*. Figure 5.28(b) shows the OSPL computed by integrating over the BBSAN noise range $0.4 \leq St \leq 2.0$. The discrepancy in the magnitude of the OSPL between experiment and the numerical simulations slightly increases, however the measured and modelled directivities have a certain agreement in shape. It is possible to better appreciate this aspect in Fig. 5.29 where the OSPL is evaluated for the numerical data shifted by -7dB as previously shown in Fig. 5.27. As seen in Fig. 5.29(b), there is a very good agreement between *elsA* and the experimental data, with Cosmic predicting monotonically lower OSPL levels at increasing polar angles.

5. SUPERSONIC UNDER-EXPANDED DUAL-STREAM JET

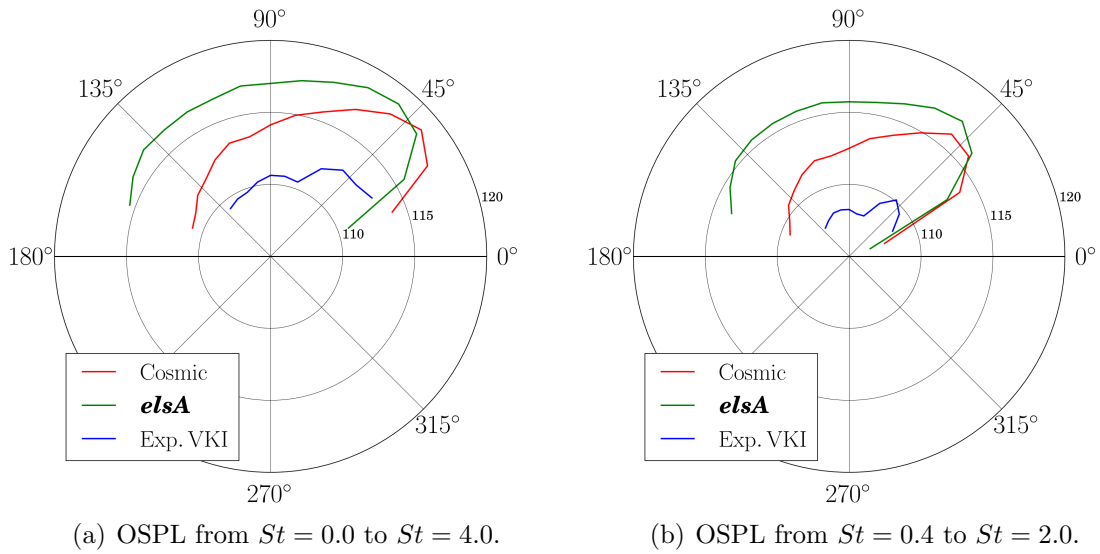


Figure 5.28: OSPL in the far-field computed at $R = 70D_p$ for an under-expanded coaxial jet. Comparison with numerical data from Pérez [100] and experimental results from Guariglia [105].

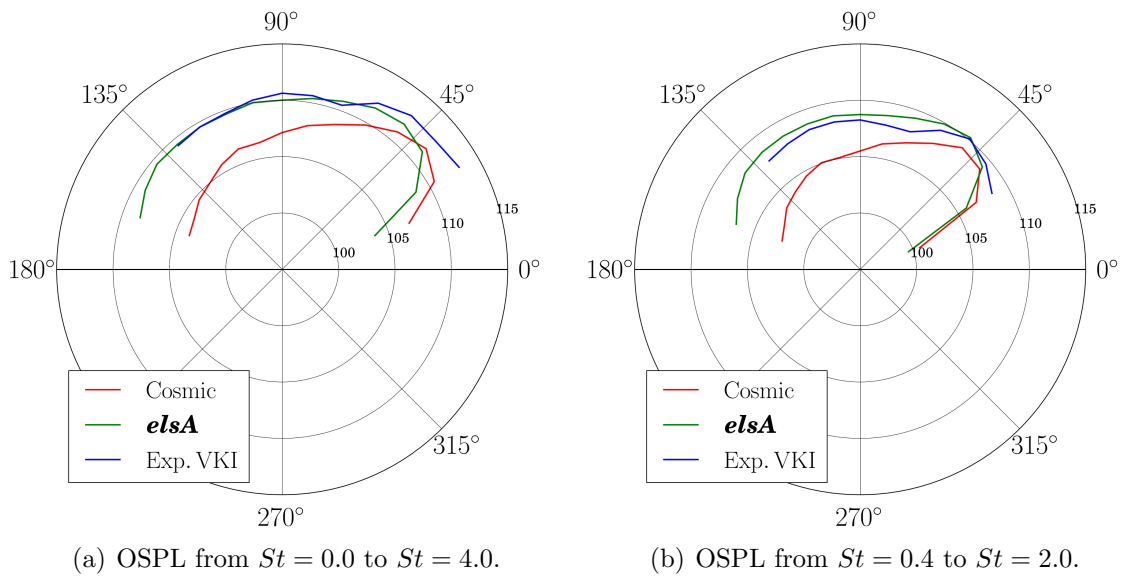


Figure 5.29: OSPL in the far-field computed at $R = 70D_p$ for an under-expanded coaxial jet. Comparison with numerical data from Pérez [100] and experimental results from Guariglia [105]. The numerical predictions are shown scaled uniformly by -7dB.

Chapter 6

Conclusions

The impact of noise in civil aviation is crucial as proven by the continuous effort of the scientific community in trying to reduce it. The jet noise component, despite being a major contributor and having been studied for decades, still proves to be elusive to a comprehensive and deep understanding of its underpinning mechanisms, and, more importantly, to accurate and efficient models able to predict it under real-case scenarios. This work explored whether lower-order hybrid DES schemes can be used for aeroacoustic investigations of supersonic under-expanded jets. The combined approach with lower-order schemes and RANS-LES methods translates into reduced computational costs compared to wall-resolved LES, cutting the simulation time and thus allowing to deliver predictions that are more in line with the current optimisation design cycle timescales of the aerospace industry.

6. CONCLUSIONS

6.1 Single jet test case

The single jet test case presented in Chapter 4 was used as the test ground to assess the strengths and limitations of the numerical scheme implemented in Cosmic. The test case proved of great value in pointing out the mesh requirements and boundary treatment requirements linked to the lower-order scheme when dealing with aeroacoustic problems. The axial discretisation showed to be lacking, causing strong numerical dissipation due to the presence of shocks and the subsequent switching to the first-order scheme due to the numerical flux limiter. The radial discretisation, on the other hand, proved to be well defined, allowing for the capturing of high Strouhal number components radiating in the near-field of the jet. Finally, the azimuthal discretisation showed to be significant for modelling the axial development of the resolved turbulence structures. An insufficient azimuthal discretisation refinement translated into excessively large and coherent structures developing in the jet shear layer. Such structures affected the noise generation mechanisms, by propagating strong hydrodynamic components in the jet near-field. The importance of an appropriate boundary layer treatment was highlighted, specifically on the transition between the RANS and LES regions in DES that required the use of a tripping function to appropriately initiate the time-dependent fluctuations of the velocity field. Similarly, the treatment of the computational boundaries was important to mitigate the onset of spurious numerical waves originating at the edges of the domain. Despite the strong limitations encountered, the obtained results, compared with experimental results and numerical results provided by third parties, proved to be of satisfactory quality, with an overall acceptable agreement both for time-averaged and time-dependent data sets. In particular, the acoustic signatures and

6. CONCLUSIONS

levels both in the near-field and in the far-field of the jet appeared to be in line with these reference numerical and experimental data, giving strong confidence that the methodology applied can be successful. The observations made for this test case allowed for the definition of appropriate measures to improve the numerical simulation for the more complex test case of the under-expanded coaxial jet.

6.2 Dual-stream jet test case

The dual-stream jet test case proved, as expected, more complicated of the previous one and new limitations were observed. Some issues arose in the experimental campaign at VKI that ran in parallel with these numerical simulations. The dimensions of the experimental apparatus were changed with respect to the original drawings and a vertical displacement of the secondary nozzle of about 2 mm in the jet direction was observed once the testing campaign was completed. These factors made the comparison between numerical and experimental results more complicated, leaving some open questions that only further experiments and numerical simulations will be able to answer. Despite these difficulties, the analysis of results gave a satisfactory outcome under many points of view. Time-averaged distributions of several quantities were compared, and good agreement was found among the data sets, especially between the numerical predictions of Cosmic and *elsA*. The limitations in mesh definition observed for the single jet test case appeared to have been successfully overcome, with the axial discretisation being sufficiently refined to correctly capture the amplitude and the decay of the axial Mach number distribution up to the end of the potential core. Good results were also obtained by increasing the azimuthal refinement, attaining turbulence structure dimensions close to the ones predicted by

6. CONCLUSIONS

elsA. Finally, thanks to the implementation of a sponge region and of fine-tuning the damping coefficient within it, the problem of low Strouhal number spurious waves travelling in the domain was successfully reduced. The main concern arising from the dual jet test case analysis was a shift of the shock-train structures in the axial direction clearly observable in the time-averaged Mach number distribution. Upon analysis of the results, and through a comparison with an available RANS prediction obtained by *elsA*, this shortcoming in the model was diagnosed and related to the RANS treatment of the outer region of the primary nozzle boundary layer, proper of the DES approach. The interaction between the strong expansion fan propagating from the secondary nozzle lip and the stationary boundary layer did not seem to provide the correct reflection angle of the waves, causing the initial shock cell structure to be shorter than that predicted using *elsA* and measured in the VKI experiment. Despite this difference in the flow topology, the key noise producing mechanisms were found to be captured by the Cosmic model and good agreement was obtained in the time-dependent results between Cosmic and *elsA*. The acoustic near-field of the jet predictions showed comparable noise levels and similar distributions, with the ‘banana’ shaped region linked to BroadBand Shock-Associated Noise (BBSAN) well visible in both data sets, and strong low Strouhal number components developing in the downstream region of the jet. The integration of the ‘banana’ region showed a maximum difference of 2.4dB between the numerical predictions at a distance of $5D_p$ from the primary jet axis. The far-field acoustic results were more challenging and characterised by the reference experimental results having lower noise levels than the prediction from either Cosmic or *elsA*. While the two numerical predictions at low Strouhal number components ranged between 110dB and 120dB, depending on the polar angle θ considered, the experimental levels over the same frequency

6. CONCLUSIONS

range were as low as 102dB. By applying a scaling factor of -7dB to the numerical results, it was possible to make the distributions match, but the reason for the 7dB difference was not identified. In the far-field noise spectra, it was possible to observe good agreement in shape among the three sets of data, with Cosmic and *elsA* being in agreement over the full modelled Strouhal number range. The experimental data showed a delayed, less steep roll-off over the range $1.5 < St < 4.0$, and the BBSAN peak was slightly shifted in frequency, which correlates well with the longer shock cells observed in the time-averaged flow data from the experiment. It was noted that Cosmic predicts lower noise levels at high polar angles θ . The cause for this behaviour was not identified.

The overall performance of Cosmic in modelling the aeroacoustics of under-expanded supersonic jets was good, with results showing broad agreement with data obtained from experiments and with numerical data from a higher-order scheme. The advantages of using a lower order DES scheme to predict noise generation in incorrectly expanded jets are mainly two: the possibility to safely deal with shocks of strong intensity without the onset of numerical instabilities and a less demanding computational cost. The DES mesh requires a significantly lower number of points in the boundary layer compared to a fully resolved LES simulation due to the RANS treatment in this region. At the same time, a lower order scheme requires a lower number of floating point operations on each iteration, translating in faster computations for the same number of cells in the domain. The full coaxial jet simulation, initialised from a fully quiescent flow, took a total of 12 days of run on 1824 processors to deliver the full set of data described in Chapter 5 for a 226M cell mesh. This kind of time scale, compared to month-long LES simulations, can allow, for example, multiple investigations of the same test case at different nozzle operating

6. CONCLUSIONS

conditions.

6.3 Further work

Due to limited computational resources and time constraints, it was not possible to extend the analyses of the test cases to different flow conditions, nor to test a shifted nozzle geometry to verify the effects of such shift on the noise generation in the coaxial jet. Further tests are necessary to assess the behaviour of the DES approach in the region of interaction of the strong expansion fan deriving from the secondary nozzle lip and the RANS boundary layer of the primary jet outer wall in order for the DES approach to be safely and confidently used as a design tool in the design and engine integration phases of wide-body civil aircraft.

Bibliography

- [1] P. Arguelles, M. Bischoff, P. Busquin, B. A. C. Droste, R. Evans, W. Kroll, J. L. Lagardere, A. Lina, J. Lumsden, D. Ranque, et al. *European Aeronautics: A vision for 2020*, volume 12. OFFICE FOR OFFICIAL PUBLICATIONS OF THE EUROPEAN COMMUNITIES, 2001.
- [2] European Commission et al. *Flightpath 2050. Europe's Vision for Aviation*. OFFICE FOR OFFICIAL PUBLICATIONS OF THE EUROPEAN COMMUNITIES, 2012.
- [3] A. Rona, D. Di Stefano, A. Mancini, and E. Hall. Time-dependent prediction of the unsteady pressure near-field from an under-expanded jet. In *20th AIAA/CEAS Aeroacoustics Conference, AIAA Aviation and Aeronautics Forum and Exposition 2014, Atlanta, Georgia, USA, 16-20 June 2014*, volume 2340, 2014.
- [4] B. André. *Etude expérimentale de l'effet du vol sur le bruit de choc de jets supersoniques sous-détendus*. PhD thesis, L'École Centrale de Lyon, 2012.
- [5] C. K. W. Tam. Computational aeroacoustics-issues and methods. *AIAA Journal*, 33(10):1788–1796, 1995.

-
- [6] M. J. Lighthill. On sound generated aerodynamically. ii. turbulence as a source of sound. *Philosophical Transactions of the Royal Society of London*, 222(1148):1–32, 1954.
- [7] S. C. Crow and F. H. Champagne. Orderly structure in jet turbulence. *Journal of Fluid Mechanics*, 48(3):547–591, 08 1971.
- [8] C. K. W. Tam, M. Golebiowski, and J. M. Seiner. On the two components of turbulent mixing noise from supersonic jets. In *2nd AIAA/CEAS Aeroacoustics Conference, May 6-8, 1996/State College, PA*. American Institute of Aeronautics and Astronautics, 1996.
- [9] M. Harper-Bourne and M. J. Fisher. The noise from shock waves in supersonic jets. In *Advisory Group for Aerospace Research and Development*, 1973. AGARD Conference on Noise Mechanisms.
- [10] C. K. W. Tam and H. K. Tanna. Shock associated noise of supersonic jets from convergent-divergent nozzles. *Journal of Sound and Vibration*, 81(3):337–358, 1982.
- [11] C. K. W. Tam. Stochastic model theory of broadband shock associated noise from supersonic jets. *Journal of Sound and Vibration*, 116(2):265–302, 1987.
- [12] C. K. W. Tam. Broadband shock-associated noise of moderately imperfectly expanded supersonic jets. *Journal of Sound and Vibration*, 140(1):55–71, 1990.
- [13] C. K. W. Tam and K. C. Chen. A statistical model of turbulence in two-dimensional mixing layers. *Journal of Fluid Mechanics*, 92(2):303–326, 05 1979.

- [14] C. K. W. Tam, J. A. Jackson, and J. M. Seiner. A multiple-scales model of the shock-cell structure of imperfectly expanded supersonic jets. *Journal of Fluid Mechanics*, 153:123–149, 1985.
- [15] C. K. W. Tam, J. M. Seiner, and J. C. Yu. Proposed relationship between broadband shock associated noise and screech tones. *Journal of Sound and Vibration*, 110(2):309–321, 1986.
- [16] A. Powell. On the mechanism of choked jet noise. *Proceedings of the Physical Society*, 66(12):1039, 1953.
- [17] L. Prandtl. Stationary waves in a gaseous jet. *Physikalische Zeitschrift*, 5:599–601, 1904.
- [18] D. C. Pack. A note on prandtl’s formula for the wave-length of a supersonic gas jet. *The Quarterly Journal of Mechanics and Applied Mathematics*, 3(2):173–181, 1950.
- [19] G. Raman. Supersonic jet screech: Half-century from powell to the present. *Journal of Sound and Vibration*, 225(3):543–571, 1999.
- [20] J. Panda. An experimental investigation of screech noise generation. *Journal of Fluid Mechanics*, 378:71–96, 1999.
- [21] J. Panda, G. Raman, and K. B. M. Q. Zaman. Underexpanded screeching jets from circular, rectangular and elliptic nozzles. *AIAA Paper*, 97-1623, 1997.
- [22] J. Lepicovsky and K. Ahuja. Experimental results on edge-tone oscillations in high-speed subsonic jets. *AIAA Journal*, 23(10):1463–1468, October 1985.

- [23] C. K. W. Tam. Supersonic jet noise. *Annual Review of Fluid Mechanics*, 27(1):17–43, 1995.
- [24] G. Raman and E. J. Rice. Instability modes excited by natural screech tones in a supersonic rectangular jet. *Physics of Fluids*, 6(12):3999–4008, 1994.
- [25] C. K. W. Tam. The shock-cell structures and screech tone frequencies of rectangular and non-axisymmetric supersonic jets. *Journal of Sound and Vibration*, 121(1):135–147, 1988.
- [26] P. J. Morris, T. R. S. Bhat, and G. Chen. A linear shock cell model for jets of arbitrary exit geometry. *Journal of Sound and Vibration*, 132(2):199 – 211, 1989.
- [27] T. D. Norum. Screech suppression in supersonic jets. *AIAA Journal*, 21(2):235–240, 1983.
- [28] Y. Y. Chan. A simple model of shock cell noise generation and its reduction. *The Journal of the Acoustical Society of America*, 54(2):556–557, 1973.
- [29] T. D. Norum and J. M. Seiner. Measurements of mean static pressure and far field acoustics of shock containing supersonic jets. *NASA Technical Memorandum*, 1982.
- [30] R. Westley and J. H. Woolley. An investigation of the near noise fields of a choked axisymmetric air jet. *National Research Council of Canada, Aeronautical Report LR-506*, June 1968.

- [31] R. Westley and J. H. Woolley. The near field sound pressures of a choked jet when oscillating in the spinning mode. *AIAA 2nd Aeroacoustics Conference*, March 1975.
- [32] A. Krothapalli, Y. Hsia, D. Baganoff, and K. Karamcheti. The role of screech tones in mixing of an underexpanded rectangular jet. *Journal of Sound and Vibration*, 106(1):119 – 143, 1986.
- [33] H. Suda, T. A. Manning, and S. Kaji. Transition of oscillation modes of rectangular supersonic jet in screech. In *AIAA, Aeroacoustics Conference, 15th, Long Beach, CA*, 1993.
- [34] J. Panda. Shock oscillation in underexpanded screeching jets. *Journal of Fluid Mechanics*, 363:173–198, 1998.
- [35] T. Suzuki and S. K. Lele. Shock leakage through an unsteady vortex-laden mixing layer: application to jet screech. *Journal of Fluid Mechanics*, 490:139–167, 2003.
- [36] C. Lui and S. K. Lele. Sound generation mechanism of shock-associated noise. In *9th AIAA/CEAS Aeroacoustics Conference and Exhibit, 12-14 May 2003, Hilton Head, South Carolina*, volume 3315, page 2003, 2003.
- [37] A. Krothapalli, P. T. Soderman, C. S. Allen, J. A. Hayes, and S. M. Jaeger. Flight effects on the far-field noise of a heated supersonic jet. *AIAA Journal*, 35(6):952–957, 1997.
- [38] G. Raman. Advances in understanding supersonic jet screech: Review and perspective. *Progress in Aerospace Sciences*, 34(1-2):45–106, June 1998.

- [39] M. D. Dahl, D. Papamoschou, and R. Hixon. Supersonic coaxial jets: Noise predictions and measurements. Technical report, NASA Technical Memorandum, 1998. Also published in AIAA-98-2294, 4th AIAA/CEAS Aeroacoustics Conferences.
- [40] E. Murakami and D. Papamoschou. Mean flow development in dual-stream compressible jets. *AIAA Journal*, 40(6):1131–1138, 2002.
- [41] E. Murakami and D. Papamoschou. Mixing layer characteristics of coaxial supersonic jets. *AIAA Journal*, 2060:1–16, 2000.
- [42] K. Viswanathan. Parametric study of noise from dual-stream nozzles. *Journal of Fluid Mechanics*, 521:35–68, 2004.
- [43] Y. Abdelhamid and U. Ganz. Prediction of shock-cell structure and noise in dual flow nozzles. *13th AIAA/CEAS Aeroacoustics Conference (28th AIAA Aeroacoustics Conference)*, 2007.
- [44] C. K. W. Tam, N. N. Pastouchenko, and K. Viswanathan. Broadband shock-cell noise from dual stream jets. *Journal of Sound and Vibration*, 324(3):861–891, 2009.
- [45] T. R. S. Bhat, U. W. Ganz, and A. Guthrie. Acoustic and flow field characteristics of shock-cell noise from dual flow nozzles. In *11th AIAA/CEAS Aeroacoustics Conference, 23-25 May, Monterey, California*, volume 2929, 2005.
- [46] K. Viswanathan, M. J. Czech, and I. C. Lee. Towards prediction of dual-stream jet noise: Database generation. *AIAA Journal*, 49(12):2695–2712, 2011.

- [47] K. Viswanathan. True farfield for dual-stream jet noise measurements. *AIAA Journal*, 49(2):443–447, 2011.
- [48] M. L. Shur, P. R. Spalart, M. K. Strelets, and A. V. Garbaruk. Further steps in les-based noise prediction for complex jets. *AIAA paper*, 485, 2006.
- [49] S. J. Eastwood and P. G. Tucker. Hybrid les—rans of complex geometry jets. *International Journal of Aeroacoustics*, 10(5-6):659–684, 2011.
- [50] M. L. Shur, P. R. Spalart, and M. K. Strelets. Noise prediction for underexpanded jets in static and flight conditions. *AIAA journal*, 49(9):2000–2017, 2011.
- [51] F. Vuillot, N. Lupoglazoff, and M. Huet. Effect of chevrons on double stream jet noise from hybrid caa computations. *AIAA Paper*, 1154, 2011.
- [52] K. Viswanathan, P. R. Spalart, M. J. Czech, A. Garbaruk, and M. Shur. Tailored nozzles for jet plume control and noise reduction. *AIAA journal*, 50(10):2115–2134, 2012.
- [53] M. Sanjosé, A. Fosso-Pouangué, S. Moreau, G. Wang, and T. Padois. Unstructured les of the baseline exejet dual-stream jet. *AIAA paper*, 3037, 2014.
- [54] D. G. Crighton. Basic principles of aerodynamic noise generation. *Progress in Aerospace Sciences*, 16(1):31–96, 1975.
- [55] T. Colonius and S. K. Lele. Computational aeroacoustics: progress on nonlinear problems of sound generation. *Progress in Aerospace Sciences*, 40(6):345–416, 2004.

- [56] B. E. Mitchell, S. K. Lele, and P. Moin. Direct computation of the sound from a compressible co-rotating vortex pair. *Journal of Fluid Mechanics*, 285(1):181–202, 1995.
- [57] J. B. Freund, S. K. Lele, and P. Moin. Numerical simulation of a mach 1.92 turbulent jet and its sound field. *AIAA Journal*, 38(11):2023–2031, 2000.
- [58] M. F. Barone and S. K. Lele. A numerical technique for trailing edge acoustic scattering problems. In *AIAA Aerospace Sciences Meeting & Exhibit, 40 th, Reno, NV*, 2002.
- [59] C. Bogey, C. Bailly, and D. Juvé. Noise investigation of a high subsonic, moderate reynolds number jet using a compressible large eddy simulation. *Theoretical and Computational Fluid Dynamics*, 16(4):273–297, 2003.
- [60] D. J. Bodony and S. K. Lele. Jet noise prediction of cold and hot subsonic jets using large-eddy simulation. In *10th AIAA/CEAS Aeroacoustics Conference 10–12 May 2004, Manchester, U.K.*, volume 3022, page 2004, 2004.
- [61] C. Bogey and C. Bailly. Effects of inflow conditions and forcing on subsonic jet flows and noise. *AIAA Journal*, 43(5):1000–1007, 2005.
- [62] C. Bogey and C. Bailly. Computation of a high reynolds number jet and its radiated noise using large eddy simulation based on explicit filtering. *Computers & Fluids*, 35(10):1344–1358, 2006.
- [63] C. Bogey and C. Bailly. Large eddy simulations of round free jets using explicit filtering with/without dynamic smagorinsky model. *International Journal of Heat and Fluid Flow*, 27(4):603–610, 2006.

- [64] C. Bogey and C. Bailly. Large eddy simulations of transitional round jets: Influence of the reynolds number on flow development and energy dissipation. *Physics of Fluids*, 18:1–14, 2006.
- [65] C. Bogey and C. Bailly. Investigation of downstream and sideline subsonic jet noise using large eddy simulation. *Theoretical and Computational Fluid Dynamics*, 20(1):23–40, 2006.
- [66] J. Schulze and J. Sesterhenn. Numerical simulation of supersonic jet-noise. *Proceedings in Applied Mathematics and Mechanics*, 8(1):10703–10704, 2008.
- [67] J. Berland, C. Bogey, and C. Bailly. Large eddy simulation of screech tone generation in a planar underexpanded jet. In *12th AIAA/CEAS Aeroacoustics Conference 27th AIAA Aeroacoustics Conference 8–10 May 2006, Cambridge, Massachusetts*, pages 8–10, 2006.
- [68] C. Bailly, P. Lafon, and S. Candel. Subsonic and supersonic jet noise predictions from statistical source models. *AIAA Journal*, 35(11):1688–1696, 1997.
- [69] T. Colonius, S. K. Lele, and P. Moin. Sound generation in a mixing layer. *Journal of Fluid Mechanics*, 330:375–409, 1997.
- [70] A. Leonard. Computing three-dimensional incompressible flows with vortex elements. *Annual Review of Fluid Mechanics*, 17(1):523–559, 1985.
- [71] G.-H. Cottet and P. D Koumoutsakos. *Vortex methods: theory and practice*. Cambridge university press, 2000.
- [72] C. Bogey, C. Bailly, and D. Juvé. Computation of flow noise using source terms in linearized euler’s equations. *AIAA journal*, 40(2):235–243, 2002.

- [73] R. Ewert, M. Meinke, and W. Schroeder. Comparison of source term formulations for a hybrid cfd/caa method. *AIAA paper*, 2200(7), 2001.
- [74] A. Yoshizawa. Statistical theory for compressible shear flows with the application of subgrid modelling. *Physics of Fluids*, 29:2152–63, 1986.
- [75] Y. Liu, P. G. Tucker, and R. M. Kerr. Linear and nonlinear model large-eddy simulations of a plane jet. *Computers & Fluids*, 37(4):439–449, May 2008.
- [76] A. A. Townsend. *The Structure of Turbulent Shear Flow*, volume 1. Cambridge University Press, 1976.
- [77] D. C. Wilcox. *Turbulence modeling for CFD*. Griffin Printing, Glendale, California, USA, 2002.
- [78] F. R. Menter. Improved two-equation $k-\omega$ turbulence models for aerodynamic flows. Technical Memorandum 103975, NASA Technical Memorandum, 1992.
- [79] U. Piomelli. Large eddy simulations in 2030 and beyond. *Philosophical transactions Series A, mathematical, physical, and engineering sciences*, 32, 2014.
- [80] E. F. Toro. *Riemann Solvers and Numerical Methods for Fluid Dynamics*. Springer-Verlag Berlin Heidelberg, 2009.
- [81] P. Roe. Approximate Riemann solvers, parameter vectors and difference schemes. *Journal of Computational Physics*, 43(2):357–372, October 1981.
- [82] C. Hirsch. *Numerical Computation of Internal and External Flows*. Butterworth-Heinemann, Oxford, second edition edition, 2007.

- [83] B. van Leer, J. Thomas, P. Roe, and R. Newsome. A comparison of numerical flux formulas for euler and navier-stokes equation. *AIAA 8th Computational Fluid Dynamics Conference*, 87-1104:36–41, 1987.
- [84] M. Manna. *A three dimensional high resolution compressible flow solver*. PhD thesis, Université Catholique de Louvain, Belgium, October 1992.
- [85] P. K. Sweby. High resolution schemes using flux limiters for hyperbolic conservation laws. *SIAM Journal on Numerical Analysis*, 21(5):995–1011, 1984.
- [86] B. van Leer. Towards the Ultimate Conservation Difference Scheme. II. Monotonicity and Conservation Combined in a Second-Order Scheme. *Journal of Computational Physics*, 14:361–370, March 1974.
- [87] J. Blazek. *Computational Fluid Dynamics: Principles and Applications (Second Edition)*. Elsevier Science, Oxford, second edition edition, 2005.
- [88] F. Q. Hu. Absorbing boundary conditions. *International Journal of Computational Fluid Dynamics*, 18(6):513–522, 2004.
- [89] M. B. Giles. Nonreflecting boundary conditions for euler equation calculations. *AIAA Journal*, 28(12):2050–2058, 1990.
- [90] D. Givoli. Non-reflective boundary conditions. *Journal of Computational Physics*, 94:1–29, 1991.
- [91] A. Fosso-Pouangué. *Schémas Volumes Finis précis: application à l'aéroacoustique de jets subsoniques- TH/CFD/11/21*. PhD thesis, Université Pierre et Marie Curie, Paris, 2011. phd.

- [92] M. F. F. El-Dosoki. *Analytical and CFD Methods Investigating Shroud Blade Tip Leakage*. PhD thesis, University of Leicester, Leicester, UK, 2009.
- [93] A. Ytterström. A tool for partitioning structured multiblock meshes for parallel computational mechanics. *International Journal of High Performance Computing Applications*, 11(4):336–343, 1997.
- [94] M. Grottadaurea. *Aerodynamics and near-field acoustics of a subsonic cylindrical cavity flow by parallel CFD*. PhD thesis, University of Leicester, UK, December 2009.
- [95] M. Monti. *Large Eddy Simulation of a cavity with a synthetic stochastic thick turbulent inflow*. PhD thesis, University of Leicester, UK, 2012.
- [96] M. Grottadaurea and A. Rona. Detached eddy simulation of subsonic cylindrical cavity flow. *Science and supercomputing in Europe*, pages 364–369, 2008.
- [97] A. Rona. Self-excited supersonic cavity flow instabilities as aerodynamic noise sources. *International Journal of Aeroacoustics*, 5(4):335–360, 2006.
- [98] M. Grottadaurea and A. Rona. Noise sources from a cylindrical cavity. *13th AIAA/CEAS Aeroacoustics Conference (28th AIAA Aeroacoustics Conference)*, 2008.
- [99] M. Grottadaurea and A. Rona. The radiating pressure field of a turbulent cylindrical cavity flow. *14th AIAA/CEAS Aeroacoustics Conference (29th AIAA Aeroacoustics Conference)*, 2007.

- [100] C. Pérez-Arroyo. *Large eddy simulations of a dual stream jet with shock-cells and noise emission analysis*. PhD thesis, Université de Toulouse, Toulouse, France, November 2016.
- [101] S. K. Lele. Compact finite difference schemes with spectral-like resolution. *Journal of Computational Physics*, 103:16–42, 1992.
- [102] A. Fosso-Pouangué, H. Deniau, F. Sicot, and P. Sagaut. Curvilinear finite volume schemes using high order compact interpolation. *Journal of Computational Physics*, 229(13):5090–5122, 2010. jx.
- [103] M. R. Visbal and D. V. Gaitonde. On the use of higher-order finite-difference schemes on curvilinear and deforming meshes. *Journal of Computational Physics*, 181:155–185, 2002.
- [104] C. Bogey and C. Bailly. A family of low dispersive and low dissipative explicit schemes for flow and noise computations. *Journal of Computational Physics*, 194(1):194–214, 2004.
- [105] D. Guariglia. *Shock-cell noise investigation on a subsonic/supersonic coaxial jet*. PhD thesis, Università degli Studi di Roma “La Sapienza”, published by the Von Karman Institute for Fluid Dynamics, Sint-Genesius-Rode, Belgium, February 2017.
- [106] C. Bogey, O. Marsden, and C. Bailly. Large-eddy simulation of the flow and acoustic fields of a reynolds number 105 subsonic jet with tripped exit boundary layers. *Physics of Fluids*, 23(3):035–104, 2011.

- [107] A. Savarese, P. Jordan, S. Girard, A. Royer, C. Fourment, E. Collin, Y. Gervais, and M. Porta. Experimental study of shock-cell noise in underexpanded supersonic jets. *AIAA Journal*, 2013.
- [108] D. Di Stefano, A. Rona, E. Hall, C. L. Morfey, and G. Puigt. Validating the fflowcs williams and hawkins acoustic analogy implementation in antares. *22nd AIAA/CEAS Aeroacoustics Conference*, 2016.
- [109] J. Schulze, J. Sesterhenn, P. Schmid, C. Bogey, N. De Cacqueray, J. Berland, and C. Bailly. Numerical simulation of supersonic jet noise. In *Numerical Simulation of Turbulent Flows and Noise Generation*, pages 29–46. Springer, 2009.
- [110] A. Singh and A. Chatterjee. Numerical prediction of supersonic jet screech frequency. *Shock Waves*, 17(4):263–272, 2007.
- [111] D. Guariglia, C. Schram, and F. Stella. Design of a facility for shock-cell noise investigation on a subsonic/supersonic coaxial jet. *PhD VKI Symposium*, 2015.
- [112] D. Guariglia, A. R. Carpio, and C. Schram. Design of a facility for shock-cells noise experimental investigation on a subsonic/supersonic coaxial jet. In *22nd AIAA/CEAS Aeroacoustics Conference, May 30 – June 1, Lyon, France*. AIAA Paper, 2016.
- [113] J. Westerweel. On velocity gradients in piv interrogation. *Experiments in Fluids*, 44(5):831–842, 2008.
- [114] F. Scarano. Iterative image deformation methods in piv. *Measurement Science and Technology*, 13(1):R1, 2001.

- [115] A. Krothapalli, L. Venkatakrishnan, L. Lourenco, and R. Elavarasan. Supersonic jet noise suppression by water injection. *6th Aeroacoustics Conference and Exhibit*, 2000.
- [116] M. Harper-Bourne and M. Fisher. The noise from shock waves in supersonic jets. In *Noise Mechanisms*, AGARD Conference Proceedings 131, pages 11–11–13, Brussels, Belgium, September 1973. Advisory Group for Aeronautical Research and Development.